University of Oxford

D. Phil. Thesis

Modelling elements of microstructure in olivine

Thomas P. Breithaupt

Supervisors: Prof. Richard F. Katz, Prof. Lars N. Hansen, and Dr. Kathryn M. Kumamoto

A thesis submitted for the degree of Doctor of Philosophy

Department of Earth Sciences

University College

Declaration of authorship

I declare that the contents of this thesis are my own, except where explicitly stated. The contents of Chapter 2 have already been published in Breithaupt et al. (2021) and the contents of Chapter 3 have been submitted for publication. I was the lead author of both studies, and my contribution to these works is indicated in the statements of authorship at the end of each of these chapters.

The COVID-19 pandemic resulted in the closure of the Rock Rheology and the Scanning Electron Microscope Laboratories in the Department of Earth Sciences, and thus greatly impacted the experimental portion of Chapter 4. Instead, these experiments were completed remotely. At my direction, Amanda M. Dillman (University of Minnesota) performed the annealing experiments, and Lars N. Hansen (University of Minnesota) polished the samples and collected backscattered electron images. I performed all subsequent analysis of this dataset.

Thomas P. Breithaupt

Michaelmas Term, 2021

Acknowledgements

Firstly, I am immensely grateful to my supervisors Richard Katz, Lars Hansen and Katie Kumamoto. I thank Rich for his guidance, mentorship, and support, as well as his boundless enthusiasm for research. I thank Lars, who has always been there at critical moments, no matter the hour or time zone. I thank Katie for taking me on as a student mid-way through my DPhil, and for her generosity with her time, knowledge, and experience.

I also thank Srikanth Toppaladoddi for introducing me to the world of stochastic differential equations, and for discussions over afternoon tea at All Souls College. I am indebted to Amanda Dillman for performing my annealing experiments, after the pandemic made it impossible for them to be completed in Oxford.

My thanks go to the members of 'Team Beam' for making it possible for me to join them on a trip to Argonne National Laboratory. In particular, I would like to thank Chris Thom for joining me on the graveyard shift, which gave me invaluable and memorable experimental experience.

I have been lucky enough to be part of two research groups during my DPhil: FOALAB and the Rock Rheology Group. The regular feedback and discussion that they have provided has been very helpful for my own research.

I thank my friends in Oxford. In particular, I thank Dan Spencer, who has been a constant source of support, insightful scientific discussion, and gossip in equal

measure. I also thank Diana Avadanii, whose support and energy has sustained me through my many years at Oxford. I thank Rellie Goddard for sharing her experience, wisdom, and friendship. I also thank Gwen Antell for her unyielding positivity and thoughtful discussions about statistics in the office.

I thank my parents and my sister, Emily, whose support has made this possible, and who have never failed to be interested in my research. Finally, I thank Grace, whose enduring love and support has sustained me throughout.

Contents

Abstract

To solve problems in the Earth and planetary sciences ranging from mantle convection and plate tectonics, magma dynamics, glacial-isostatic adjustment, post-seismic creep, seismic attenuation, and tidal dissipation, we require a deep understanding of the rheological, seismic, and chemical properties of silicate materials. Elements of microstructure, such as grain size and dislocation density, exert a strong control on these properties. In this thesis, I apply novel approaches to modelling the time evolution of these quantities.

I begin by examining grain-size evolution in the regime of normal grain growth, which is driven by surface energy reduction. I extend the canonical model of normal grain growth by limiting the interactions of a grain to its neighbourhood. In this extended model, heterogeneity in the local environments of grains is accounted for using a stochastic process. The model predicts the existence of a normal grain growth regime that evolves according to accepted grain-growth kinetics. Moreover, this regime is characterised by a grain-size distribution that agrees with observed distributions, in direct contrast to the distribution predicted by the canonical model.

I then examine dislocation-density evolution. I construct a new theory of the physical processes affecting dislocations: storage and recovery. The evolution of dislocation density is fundamentally connected to intracrystalline plastic deformation, and thus also makes predictions about viscosity. We calibrate our theoretical framework for

olivine using data from steady-state deformation experiments. This model explains the empirical relationships among strain rate, applied stress, and dislocation density in disparate laboratory regimes. Indeed, it predicts the previously unexplained dependence of dislocation density on applied stress in olivine. The predictions of our model for geological conditions differ from direct extrapolations from experimental data. For example, the calibrated model predicts rapid, transient deformation in the upper mantle, consistent with recent measurements of post-glacial rebound.

The calibrated model of dislocation-density evolution sets out the hypothesis that dislocation recovery in olivine is controlled by pipe diffusion. This assumption is in direct contrast with previous work, which has assumed that dislocation recovery in olivine is controlled by lattice diffusion instead. The recovery process can be inferred from annealing experiments that track the decrease in dislocation density with time. Through statistical analysis of data from new annealing experiments, combined with previously published data from the literature, I determine that the dominant dislocation recovery process in olivine is likely controlled by pipe diffusion.

Chapter 1

Introduction

Investigation of the dynamics of rocky planetary bodies requires detailed knowledge of the properties of silicate minerals. Indeed, our approach to addressing problems in these areas relies on models of rheological, seismic, and chemical properties, and how these properties change in time. Our understanding of these properties is developed through a combination of experimental investigation and theoretical analysis. However, application of empirically-derived trends in these properties requires extrapolation outside of laboratory conditions, creating epistemic uncertainties. Moreover, the construction of quantitative models can be hindered by their dependence of these properties on the complicated microstructures of these materials. As a result, the approach to modelling these quantities often remains phenomenological in nature. Consequently, there is a need for novel approaches to modelling microstructures and their relationship to material properties.

In this thesis, I focus on two aspects of microstructure in crystalline materials, grain size and dislocation density, which quantify the amount of planar and linear lattice defects present in the material. These aspects of microstructure exert a strong control on rheological properties, but the processes that control their evolution remain understudied, and thus are an ideal target for investigation.

In this introductory chapter, I first introduce some geodynamic contexts in which microstructure and its influence on material properties plays a fundamental role. Then, I review the properties of grains and dislocations and current approaches to modelling these aspects of microstructure. Finally, I outline the structure of this thesis.

1.1 Geodynamic context

One of the most central dynamic process within the Earth and planetary sciences is mantle convection, which exerts a first-order control on the thermal and chemical structure of many planetary bodies. Thermal convection involves the advection of buoyant fluid, which is resisted by the fluid's viscosity. Thus, both the presence and vigour of convection in planetary bodies is controlled by viscosity. Both grain size and dislocation density play fundamental roles in determining viscosity, and therefore influence mantle convection. Furthermore, these quantities are expected to dynamically evolve and thus may influence the thermal histories of convecting bodies. For example, Hall and Parmentier (2003) demonstrated that the transient evolution of grain-size may delay the onset of convection. However, the potential role of dislocation density evolution in mantle convection remains unknown.

On Earth, mantle convection manifests as plate tectonics, a distinct mode of convection in which thermal transport is accommodated by the conductive cooling of the plates and their subsequent foundering into the mantle (Bercovici, 2003). The plates themselves are strong internally, with deformation localised into narrow plate boundaries. The mechanism by which plate boundaries form remains an open question (Bercovici, 2003; Mulyukova and Bercovici, 2019*a*). However, the correlation of relatively fine-grained rocks with plate boundaries (Warren and Hirth, 2006; Skemer et al., 2010) strongly suggests that grain-size evolution plays an important role in the

generation of plate boundaries (Mulyukova and Bercovici, 2019*a*).

Microstructural evolution, through its influence on transient viscosities, is also highly relevant to a broad range of settings involving time-dependent loading, including glacial-isostatic adjustment (Rümpker and Wolff, 1996), post-seismic creep (Pollitz et al., 2006; Freed et al., 2012), and tidal dissipation on other planetary bodies such as the Moon (Nimmo et al., 2012) and Jupiter's moon Io (Bierson and Nimmo, 2016). Microstructure also exerts a strong control on the attenuation of seismic waves. Indeed, dislocations and grain boundaries play a fundamental role in some mechanisms of seismic attenuation (Granato and Lücke, 1956; Gribb and Cooper, 1998).

A further property of interest is permeability, a quantity that describes the ease with which fluids can flow through porous media (e.g., McKenzie, 1984). On Earth, permeability is the relevant quantity for describing the flow of magma and fluids in mid-ocean ridges and subduction zones. Permeability is strongly dependent on the grain size (McKenzie, 1984). Therefore, grain size and its evolution can exert a strong control on the dynamics of these settings. Indeed, numerical simulations have demonstrated that grain-size evolution and its subsequent effects on permeability can control melt focusing in these settings (Cerpa et al., 2017; Turner et al., 2015). Similar considerations apply to magma dynamics in other planetary bodies. For example, grain size, through its control on permeability, may control whether or not rocky planetessimals develop magma oceans (Lichtenberg et al., 2019).

1.2 Grains and grain boundaries

Grains are volumes of the crystal lattice with a coherent crystallographic orientation that are separated from each other by interfaces termed grain boundaries. The grain boundaries themselves are two dimensional lattice defects. Grains are quantitatively

described by their size, which is a measure of the linear dimension of the grain. Grain size is an key microstructural length scale that is relevant for many processes, for example, setting the effective diffusion length scale in diffusion creep (pp. 131, Karato, 2008).

There are various approaches to defining grain size, such as the mean width or the radius of the volume-equivalent sphere, and the choice of definition will depend on the context. The grain microstructure can then be described using the probability density function of grain size, or grain-size distribution, which describes the fraction of grains with a specified size. For the purpose of modelling of material properties, such as viscosity (e.g. Hansen et al., 2011), or within geodynamic simulations (e.g. Turner et al., 2015), the grain-size distribution is often summarised using only the mean grain size.

1.2.1 Evolution of grain microstructure

Grain microstructure evolves through migration of grain boundaries and the creation of new grains. Grain boundary migration occurs by exchanges of mass between neighbouring grains, which are driven by differences in the free energy density of the neighbouring grains (pp. 223, Karato, 2008). The dominant sources of free energy within the microstructure are the surface energy associated with the grain boundaries, and the stored energy of deformation (e.g., Holtzman et al., 2018; Mulyukova and Bercovici, 2019*b*). In addition, the stored energy of deformation can also drive the creation of new grains, releasing this stored energy, in the process of dynamic recrystallisation (e.g., Karato et al., 1980). In this thesis, I focus on changes in the grain microstructure driven by surface energy.

As grain boundaries are two-dimensional defects, they possess an excess free energy per unit area, γ. The surface energy density of a grain of size R is proportional to γ/R. This free energy density can be decreased by increasing the grain size,

and thus grain-boundary migration driven by surface energy results in overall grain growth. In detail, for grain growth driven by surface energy, each local patch of grain boundary migrates towards its local centre of curvature at a rate proportional to the mean curvature of the boundary at that point (Mullins, 1956). By considering the integral of mean curvature across the entire grain surface, Von Neumann (1952) and Mullins (1956) (in 2D systems), and MacPherson and Srolovitz (2007) (in 3D systems) obtained expressions for the rate of change of grain area in terms of topological properties of grains. These expressions may be combined with grain size-topology relationships to obtain kinetic models that express the rate of change of grain size as a function of grain size (e.g., Pande and McFadden, 2010). The canonical kinetic model is due to Hillert (1965):

$$\frac{dR_i}{dt} \propto \left(\frac{1}{R_m} - \frac{1}{R_i} \right), \tag{1.1}$$

where R_i is the radius of the i^{th} grain and R_m is the mean-field radius, which encapsulates the effect of the average curvature of neighbouring grains. To investigate grain growth driven by surface energy, Equation (1.1) or similar kinetic models are integrated forward in time for populations of grains (e.g. Hillert, 1965; Hunderi and Ryum, 1980; Ryum and Hunderi, 1989; Streitenberger and Zöllner, 2006; Zöllner and Streitenberger, 2006).

After sufficient time has elapsed, the grain microstructure and grain growth kinetics tend toward a regime termed normal grain growth. In the normal grain growth regime, the grain-size distribution becomes narrow in extent, giving the microstructure a uniform appearance, and its shape, when normalised by the mean grain size, is independent of time (e.g., Atkinson, 1988). A key test of these models is the grain-size distribution they predict in the normal grain growth regime, which may be compared to observed distributions from experiments and full-field numerical simula-

tions. Hillert's model predicts a grain-size distribution that does not match observed distributions (Rios et al., 2006; Rios and Glicksman, 2006*a*; Rios and Zöllner, 2018). Recently, new kinetic equations have been constructed that predict grain-size distributions in agreement with observations (Rios et al., 2006; Zöllner and Streitenberger, 2006; Pande and Moser, 2020). However, these approaches contain fitting parameters, whose physical interpretation is unclear, and which limit the applicability of these models outside the normal grain growth regime.

Within the geodynamic models, grain-size evolution models that track the change in mean grain size are used (Hall and Parmentier, 2003; Austin and Evans, 2007). These models are synchronous, assuming that the total rate of change of mean grain size can be additively decomposed into contributions from normal grain growth and dynamic recrystallisation. However, as discussed above, the kinetics of normal grain growth are related to the grain topologies developed in normal grain growth, and do not necessarily apply outside of this regime. Therefore, to apply these models confidently, there is a need for new models of normal grain growth that can match observations without these fitting parameters.

1.3 Dislocations

Dislocations are line defects in the crystal lattice. The density of dislocations is determined by the total length of dislocations per unit volume. Along the dislocation line, or core, the crystal lattice is disrupted. In addition, the dislocation elastically strains the surrounding lattice, resulting in a corresponding stress field, and as a result, dislocations store strain-energy in the crystal lattice. Dislocation motion plays a fundamental role in plastic deformation. Indeed, dislocations are the carriers of deformation in a range of deformation mechanisms: dislocation creep, low-temperature plasticity, and and dislocation-accommodated grain boundary sliding. To understand

the behaviour of these deformation mechanisms, we need to understand the processes that control dislocation density.

In this thesis, I explore dislocation density evolution in the mineral olivine. Olivine is a useful case-study for my approach because there are many published experiments exploring the relationships between dislocation density and other variables in olivine (Durham et al., 1977; Bai and Kohlstedt, 1992; Kohlstedt and Goetze, 1974; Farla et al., 2011; Jung and Karato, 2001; Ohuchi et al., 2011; Hirth and Kohlstedt, 2015). Moreover, as olivine is the most abundant mineral in the upper mantle, understanding the behaviour of plastic deformation realised by the motion of dislocations in olivine grants us an insight into the dynamics of the upper mantle.

1.3.1 Dislocations and deformation

Despite the role of dislocations as carriers of intracrystalline deformation, the dislocation density does not explicitly appear in empirical flow laws for dislocation-mediated deformation mechanism. Instead, the effect of dislocation density is implicitly included in flow laws as part of stress dependence of strain rate. Alternatively, the strain rate can be modelled with the Orowan equation (Orowan, 1934), which explicitly accounts for dislocation density:

$$\dot{\varepsilon} = \rho b v, \tag{1.2}$$

where b is the magnitude of the Burgers vector, ρ is the dislocation density, and v is the dislocation velocity. To predict the dependence of strain rate on the applied stress driving deformation, σ, relationships between ρ, v and σ are required. By assuming that the dislocation stress fields approximately balance the applied stress in magnitude in steady-state deformation, the dislocation density is predicted to be proportional to the square of the applied stress, $\rho \propto \sigma^2$ (e.g., Kohlstedt and Weath-

ers, 1980). Guided by models of diffusion-limited dislocation motion, the dislocation velocity in the dislocation-creep deformation mechanism is predicted to be proportional to the applied stress $v \propto \sigma$ (pp. 108–109, Poirier, 1985). The combination of Equation (1.2) and these scaling relationships predict a stress exponent of 3, i.e., $\dot{\varepsilon} \propto \sigma^3$.

However, in practise, these scaling relationships do not hold for deformation by dislocation creep in olivine. The dislocation density is observed to scale as $\rho \propto \sigma^{1.4}$ (Bai and Kohlstedt, 1992). Adjusting for the smaller exponent on this relationship leads to a smaller predicted stress exponent of 2.4 (Hirth and Kohlstedt, 2015). Moreover, the observed stress exponent in dislocation creep is approximately 3.5, a greater value than predicted by these simple models (Hirth and Kohlstedt, 2015). Hirth and Kohlstedt (2015) hypothesised that this discrepancy can be explained if vacancy diffusion is controlled by pipe diffusion, and therefore $v \propto \rho\sigma$. This dislocation-density scaling predicts a stress exponent of 3.8, which is broadly consistent with observations. However, this analysis assumes an empirical dislocation-density stress relationship, which still remains unexplained.

1.3.2 Dislocation-density evolution

Dislocation density rapidly increases with plastic deformation (pp. 155, Messerschmidt, 2010), and with sufficient plastic strain attains a steady-state value that is related to the applied stress (e.g., Takeuchi and Argon, 1976). Increases in dislocation density are connected geometrically to dislocation motion, and therefore plastic strain (Kocks, 1966). In contrast, decreases in dislocation density can occur by time-dependent diffusion-limited processes, and thus continue to operate after deformation (pp. 168, Messerschmidt, 2010).

In the geoscience literature, two models of dislocation density evolution have been recently presented by Holtzman et al. (2018) and Mulyukova and Bercovici (2019*b*).

Both of these models do not explicitly link their dislocation density kinetics to physical processes. Furthermore, these models assume a steady-state relationship between dislocation density and applied stress *a priori*, and thus cannot be used to investigate the origin of this relationship. Consequently, there is a need for a new model of dislocation-density evolution to tackle this question.

1.4 Key questions

1. What physical processes are not currently captured by models of normal grain growth?

2. What physical processes control the steady-state scaling of dislocation density in olivine?

3. Can a model of dislocation-density evolution explain the fundamental scalings of dislocation-controlled deformation mechanisms with variables such as stress?

4. To what extent does pipe-diffusion control dislocation-density evolution in olivine?

1.5 Thesis structure

In this chapter, I have highlighted the necessity of models describing microstructural evolution to answering some of the outstanding problems in the Earth and planetary sciences. In this thesis, I will use novel modelling approaches to address the evolution of grain size and dislocation density, and how these parameters affect viscosity. I also conduct new experiments to test hypotheses arising from these models.

In Chapter 2, I construct a new stochastic model of normal grain growth that incorporates random noise. I will examine the role of a grain's neighbourhood in determining the kinetics of its growth, and the impact on the grain-size distribution. This chapter

will conclude with an examination of the source of random noise in grain growth, and the connection between this noise and the topological properties of grains. This chapter has already been published as:

> Breithaupt, T., Hansen, L.N., Toppaladoddi, S. and Katz, R.F., 2021. The role of grain-environment heterogeneity in normal grain growth: A stochastic approach. *Acta Materialia, 209*, p.116699.

In Chapter 3, I will construct a model of dislocation density evolution by considering the fundamental processes that control dislocation density: dislocation storage and dislocation recovery. I will calibrate the model against data gathered from deformation experiments on olivine. I consider the underlying principles that lead to the empirical scaling relationships between the strain rate, dislocation density, and applied stress. Finally, I will consider the models predictions regarding both steady-state and transient deformation in the upper mantle. This chapter has been submitted to the journal *Science Advances*:

> Breithaupt, T., Katz, R. F., Hansen, L. N., and Kumamoto, K.M. (submitted). Dislocation theory of steady and transient creep of crystalline solids: predictions for olivine

In Chapter 4, I examine dislocation recovery experiments performed on olivine. In previous studies, the dominant recovery process and its associated kinetics have been assumed *a priori*. In contrast, I explore the potential recovery processes that could have been observed in these experiments, and the consistency of the kinetic predictions of each processes with experimental data. I perform new recovery experiments that aim to determine the dominant recovery process in olivine.

Chapter 2

Grain-environment heterogeneity in normal grain growth

This work has already been published in Breithaupt et al. (2021). I have made minor adjustments to the formatting and content of this work to put it within the context of this thesis.

2.1 Introduction

Many properties of engineered and natural materials are controlled by the size distribution of their constituent grains. Accurately modelling the evolution of the distribution of grain size is critical to understanding these properties, and is a prerequisite to modelling processes such as strain localisation due to grain-size reduction (Rozel et al., 2011). The fundamental process acting on grain size is normal grain growth; to confidently predict the evolution of a population of grains undergoing deformation, we must first predict the grain-size distributions that result from normal grain growth. Normal grain growth is driven by the tendency to minimise the total surface energy of the grains. In observations of normal grain growth from laboratory experiments and numerical simulations, the mean grain size grows as the square root of time, and the distribution of grain size normalized by the mean is constant (Rios and Zöllner,

2018). The latter property is termed statistical self-similarity. The classical, mean-field theory of grain growth due to Hillert (1965) assumes that grains are spherical and grow at a rate that depends on each grain's self-curvature and a global, mean-field curvature. Hillert's model achieves the observed square-root of time kinetics but predicts a self-similar distribution that is inconsistent with observations (Rios et al., 2006; Rios and Glicksman, 2006*a*; Rios and Zöllner, 2018). Despite this inconsistency, analysis of the thermodynamics (Fischer et al., 2003; Kertsch and Helm, 2016) and grain topology (Rios and Glicksman, 2006*b*) have provided support for Hillert kinetics, and the Hillert model forms the basis for many models of normal grain growth (e.g., Brown, 1989; Pande and Dantsker, 1990; Marthinsen et al., 1996; Zöllner and Streitenberger, 2006). We take the kinetics of the Hillert model as our starting point.

We modify the Hillert model by replacing the mean-field curvature with a local curvature, defined as the mean curvature over the local environment of each grain. The local environment of a grain is the set of its nearest-neighbour grains, i.e., the grains that it exchanges mass with. The local environment of a grain interacts with a much larger set of grains, many of which are screened from the grain by its neighbours. From the perspective of individual grains, the local curvature will undergo a random walk, providing a source of noise to the grain-size kinetics. To capture this effect, we introduce a stochastic term into our model with an amplitude determined by the global statistics of local environments. Our approach differs from other stochastic models because the amplitude of our noise is determined through the hypothesis of a specific physical source (Pande and Dantsker, 1990; Pande and McFadden, 2010; Pande and Moser, 2020).

The local curvature is defined as an average grain curvature over the local environment, which is itself a small sample of the global population of grains. Hence, the distribution of local curvatures will approximate a normal distribution. We therefore model local curvatures using an Ornstein-Uhlenbeck process, because realisations of

this process are normally distributed (Uhlenbeck and Ornstein, 1930; Wang and Uhlenbeck, 1945). We solve the coupled stochastic differential equations for grain radius and local environment for a large ($N \approx 10^6$) set of grains over a sufficiently long period of time for the set to reach statistical self-similarity. We obtain grain-size distributions that are in agreement with observations, indicating that heterogeneity in the local environments of grains plays a key role in normal grain growth.

2.1.1 Classical models of grain growth

In his canonical model, Hillert (1965) assumed the simplest possible expression for the grain-growth rate that gives the required behaviour: that small grains shrink and large grains grow. As a result, Hillert's theory does not explicitly incorporate key physical principles such as the geometric requirement of equilibrium dihedral angles and the topological requirement of filling space. Nevertheless, Hillert's theory forms the basis of many models of normal grain growth (e.g. Brown, 1989; Pande and Dantsker, 1990; Marthinsen et al., 1996; Zöllner and Streitenberger, 2006). More recently, Hillert's model has gained support from topological and thermodynamic perspectives. Rios and Glicksman (2006*a*) develop a special set of polyhedra that possess equilibrium dihedral angles and are space filling. By assuming that every grain can be approximated by a member of this set, they develop equations for the rate of change of grain size and the number of grain faces. Ultimately they demonstrate that, given certain assumptions about grain topology, their model is equivalent to Hillert's, validating Hillert's approach. Similarly, distinct thermodynamic approaches derive a variation of the Hillert model (Fischer et al., 2003; Kertsch and Helm, 2016) that reduces to the classical Hillert model under the assumption that the mobilities of all grain boundaries are given by a single constant. However, broadly recognised discrepancies between observations and Hillert's distribution indicate that the theory does not provide an adequate approximation to the grain-growth rate (Rios et al.,

2006; Rios and Glicksman, 2006*a*; Rios and Zöllner, 2018).

Modifications to Hillert's model centre on the introduction of adjustable parameters or stochastic terms. Brown (1989) suggested relaxing a stability argument that Hillert had applied, and thereby introduced an adjustable parameter into the model. Rios (1999) applied this approach to derive a one-parameter family of distributions, some of which are in agreement with observed distributions (Rios et al., 2006). However, the stability of these distributions and the physical justification for Brown's approach are a matter of debate (Rios, 1999), and the selection of the best-fit Rios distribution is essentially a "phenomenological procedure" (Rios and Lücke, 2001). In contrast, Marthinsen et al. (1996) used numerical simulations to guide modification of Hillert's theory. In their simulations, an inverse correlation develops between a grain's size and its local environment. This correlation develops because large grains grow by taking mass away from their neighbours, shrinking them. Marthinsen et al. regress this correlation and adapt Hillert's model into a correlation-field theory of normal grain growth. However, their predicted distribution is too negatively skewed to match observations. Streitenberger (1998) furthered this approach by deriving a constraint on the linear fit between the local environment and grain size. Using only this constraint and the intercept of the relationship in Marthinsen et al. (1996), Streitenberger predicts a grain-size distribution that is in agreement with the distribution observed by Marthinsen et al. However, the gradient Streitenberger infers is much higher than the gradient of the correlation observed by Marthinsen et al., which Streitenberger attributes to topological constraints not accounted for in the model.

Alternatively, Hillert's model can be augmented with stochastic terms. By considering the statistical divergence between two solutions for the grain-size distribution, Pande and Rajagopal (2001) argued that under deterministic grain-size kinetics, arbitrary initial distributions cannot converge to a unique self-similar distribution. Consequently, grain-size kinetics must incorporate a stochastic term to reproduce this key

feature of normal grain growth. Typically, an additive white-noise term is appended to the Hillert kinetics (Pande and Dantsker, 1990; Pande et al., 2008). The strength of the noise introduced by this term is left as an adjustable parameter, and so its presence is not directly attributed to any one process. However, it has been suggested that the effect of heterogeneity in the local environments of grains provides a source of noise (Pande and Dantsker, 1991; Pande and Moser, 2020). In this case, the self-similar grain-size distribution can be found by solving the Fokker-Planck equation associated with the proposed grain-size kinetics. Pande and Moser (2020) seek an approximate analytical solution and find that it is equivalent to a previously derived distribution from a modified mean-field theory (Streitenberger and Zöllner, 2006) and that is in agreement with observed distributions.

The application of white noise to normal grain growth is not without controversy, however. Implicit in the assumption of white noise is that the process causing fluctuations in grain size occurs on a much shorter timescale than the process driving deterministic evolution of grain size (Mullins, 1998). Since neighbouring grains should change their size on the timescale of grain-size evolution itself, Mullins argued that fluctuations in grain-growth rate within these models cannot arise from the neighbouring grains (Mullins, 1998). In contrast, (Pande and Moser, 2020) have argued that any fluctuation-causing process that affects a single grain will ultimately affect the growth rate of every grain in the system. As the number of grains becomes large, the timescale of fluctuations becomes arbitrarily small. White noise can therefore be applied to model normal grain growth under the assumption that the spatial influence of each fluctuation is arbitrarily large.

2.2 Our model

We propose a modification to Hillert's theory that is associated with the mean-field curvature. We adjust the mean-field curvature by a local term that is specific to each grain. This local term accounts for the difference between the mean-field environment and the local environment of each grain. Our approach differs from previous modifications because the local environment of each grain is allowed to evolve independently. We hypothesise that the differential of the size of the i^{th} grain $\mathrm{d}R_i$ is given by

$$\mathrm{d}R_i(t) = \alpha \left(\frac{1}{R_m(t) + S_i(t)} - \frac{1}{R_i(t)} \right) \mathrm{d}t, \tag{2.1}$$

where α, which has the units of diffusivity, is the product of the surface energy per unit area, the grain-boundary mobility, and a geometric factor of order unity. We assume that the surface energies and the mobilities of all grain boundaries are identical, an assumption that has been previously called the uniform-boundary model (Rios, 2004). Consequently, α is a constant for all grains. $R_m(t)$ is the mean-field radius, S_i is the deviation of the local environment from the mean field, and t is time. Variables labelled with a subscript i are local quantities, specific to the i^{th} individual grain. We develop a model for the evolution of S_i below. Hillert's theory can be recovered from Equation (2.1) by setting $S_i(t)$ equal to zero. We suggest that Equation (2.1) better reflects the physics of grain growth at the grain scale, for which the size of a grain relative to its neighbours plays a role in determining grain-growth rates.

The mean-field radius is calculated by requiring the total mass of the set of grains to be conserved. Since density is constant for a single phase, this is equivalent to conservation of total grain volume. Assuming that each grain is spherical, the differential

of grain volume $\mathrm{d}V_i$ is given by

$$\mathrm{d}V_i(t) = 4\pi\alpha \left(\frac{{R_i}^2}{R_m(t) + S_i(t)} - R_i \right) \mathrm{d}t. \tag{2.2}$$

Total volume conservation is enforced by requiring that the sum of all volume increments given by Equation (2.2) vanishes, or equivalently, that the expectation value of $\mathrm{d}V_i$ vanishes. For the expectation of $\mathrm{d}V_i$ to vanish, it must be true that

$$\mathrm{E}\left[\frac{R_i(t)^2}{R_m(t) + S_i(t)} \right] - \mathrm{E}[R_i(t)] = 0, \tag{2.3}$$

where $E[\cdot]$ is the expectation defined over the complete set of grains. Equation (2.3) implicitly determines the mean-field radius R_m. In Hillert's theory, S_i is zero and the mean-field radius is $\mathrm{E}[{R_i}^2]/\mathrm{E}[R_i]$.

The local environment radius $R_m + S_i$ represents the interactions of a grain with its neighbours. We assume that these interactions are exactly governed by the Hillert model and are volume conserving. However, since a grain's interactions are confined to its neighbourhood only, the average over all grains used to compute the mean-field radius in the Hillert model ($\mathrm{E}[R_i^2]/\mathrm{E}[R_i]$) is, in our model, restricted to the neighbourhood of the grain only. Consequently, the local environment radius is here given by $\mathrm{E}_i[{R_i}^2]/\mathrm{E}_i[R_i]$, where $\mathrm{E}_i[\cdot]$ is the local mean—the expectation defined over the set of a grain and its neighbours—and is local to an individual grain. The distribution of local environment radii is a sampling distribution of this statistic from the global distribution of grain size. We make the simplifying assumption that this sampling distribution is normally distributed and has a variance given by the small-sample distribution of the mean of R_i, under the central limit theorem. Therefore, the

deviation S_i from the mean-field radius is normally distributed as

$$S_i \sim \mathcal{N}\left(0, \frac{1}{n}\mathrm{Var}[R_i]\right), \tag{2.4}$$

with a variance $\mathrm{Var}[R_i]/n$, where n is the number of grains in the small-sample set of a grain and its neighbours. The number of grains surrounding a given grain will depend on the size of that grain compared to the size of those surrounding it; grains that are small should have comparatively few neighbours. Introducing this dependence would couple the evolution of a grain's local environment S_i to its size R_i in a manner that goes beyond the sensitivity to the whole set of grains implied by Equation (2.4). To avoid this complication, we make the simplifying assumption that n is a constant for all grains.

The grains comprising the local environment of an individual grain interact more broadly than does the individual grain itself. In particular, they exchange mass with a much larger set of grains. Heterogeneity in the size of grains within this larger set will drive heterogeneity in exchanges of mass. Consequently, local environments that are initially similar may evolve along very different (and random) trajectories. We make the simplifying assumption that these random walks can be modelled as being Brownian. Consequently, the evolution of S_i is modelled by a stochastic differential equation with a random term $\Omega\,\mathrm{d}W(t)$, for which $\Omega^2/2$ is a diffusion coefficient and $W(t)$ is the standard Wiener process. Ω quantifies the heterogeneity in the evolution of local environments, which is a consequence of heterogeneity in the broader set of grains that exchange mass with the local environment.

Furthermore, as the grains that comprise the local environment evolve, some may shrink to zero size. Once this occurs, they may be replaced by grains from beyond the local environment. The introduction of replacement grains from the global set of grains will tend to pull the local environment radius $R_m + S_i$ towards the mean-field

radius R_m. A detailed description of this process would involve modelling the episodic loss of grains from the local environment and the grains that replace them. Instead, we make the simplifying assumption that the replacement of grains can be approximated by the continuous decay of the deviation S_i between the local-environment radius and the mean-field radius on the timescale of removal, which is the timescale of normal grain growth τ. Mathematically, this can be represented by $-(S_i/\tau)\mathrm{d}t$, where

$$\tau(t) = 2\frac{\mathrm{E}[R_i]^2}{\alpha}. \tag{2.5}$$

As the timescale τ increases, the decay of S_i will be retarded. Physically, this reduced decay rate corresponds to a reduction in the rate of introduction of replacement grains into any given local environment that occurs as grain growth and the associated removal of grains slows.

Combining both of these components, we obtain an Ornstein-Uhlenbeck process

$$\mathrm{d}S_i(t) = -\frac{S_i(t)}{\tau(t)}\mathrm{d}t + \Omega(t)\mathrm{d}W(t). \tag{2.6}$$

The ensemble statistics of S_i generated by Equation (2.6) are normal and, provided that the initial mean of S_i is zero, consistent with the statistics given by Equation (2.4). Ω can be determined by requiring that S_i has the variance given by Equation (2.4). Consequently, Ω will depend on the variance of the grain-size distribution, which is a measure of heterogeneity in grain size. Since the variance of the grain-size distribution is a function of time, we let Ω vary with time.

Normal grain growth is a spontaneous irreversible process (Rios, 2004). For the proposed model to be thermodynamically admissible, by the second law of thermodynamics, the rate of entropy production must be positive. In our notation, this is equivalent to the statement that $\mathrm{E}[R_i\dot{R}_i]$ is negative (Fischer et al., 2003). This condition is satisfied by the Hillert model because the mean-field radius R_m exceeds

the mean radius $\mathrm{E}[R_i]$. We have assumed that local interactions within a grain neighbourhood are governed by the Hillert model and therefore in our model, the entropy production rate is positive within every grain neighbourhood. Moreover, we have approximated the distribution of local environment radii as a normal distribution (Equation 2.4). Under this approximation, positivity of entropy production holds provided that the standard deviation of S_i is sufficiently small relative to R_m. This condition is satisfied for all of the results we have obtained.

To remove material-specific properties from the model, we non-dimensionalise variables using the initial mean grain size $\mathrm{E}[R_i(0)]$ as the scale for grain size and $2\mathrm{E}[R_i(0)]^2/\alpha$ as the scale for time. This timescale is chosen such that under the Hillert model, once the self-similar state is achieved, the square of the mean-field radius is a linear function of time with unit gradient. Equations (2.1), (2.3), and (2.6) take the non-dimensional form

$$\mathrm{d}R_i' = 2\left(\frac{1}{R_m'(t') + S_i'} - \frac{1}{R_i'}\right)\mathrm{d}t', \tag{2.7}$$

$$\mathrm{d}S_i' = -\frac{S_i'}{\mathrm{E}[R_i']^2}\mathrm{d}t' + \Omega'(t')\mathrm{d}W(t'), \tag{2.8}$$

$$0 = \mathrm{E}\Big[\frac{R_i'^2}{R_m'(t') + S_i'}\Big] - \mathrm{E}[R_i'], \tag{2.9}$$

where a prime denotes a non-dimensional variable. From this point, we drop primes and maintain pre-scaled notation for the rest of the paper. Equations (2.7) and (2.8) allow calculation of the time evolution of R_i and S_i provided that $R_m(t)$, $\mathrm{E}[R_i(t)]$, and $\Omega(t)$ are known.

To find the self-similar distribution of grain size that develops, we take a Monte Carlo approach of simulating a large set of (R_i, S_i) pairs as a function of time. For each pair, we integrate Equations (2.7) and (2.8) forward in time with the Euler-Maruyama scheme, using code developed in the framework of the Portable, Extensible Toolkit for Scientific Computation (PETSc) (Balay et al., 1997, 2018). Normally

distributed random numbers for Equation (2.8) are generated by applying a Box-Muller transform to uniformally distributed random numbers from the 64-bit linear congruential generator implemented in SPRNG-1.0 (Mascagni and Srinivasan, 2000). $\mathrm{E}[R_i(t)]$ is trivially calculated as the mean grain size at the current timestep. We solve Equation (2.9) implicitly for $R_m(t)$ by Newton's method, using the value of $R_m(t)$ at the previous timestep as an initial guess. Finally, we calculate $\Omega(t)$ by requiring the small-sample statistics of $\Omega(t)$, given in Equation (2.4), to hold at the end of an Euler-Maruyama timestep (see Appendix 2.A). Consequently, $\Omega(t)$ is given by

$$\Omega(t)^2 = \frac{1}{\Delta t}\left[\frac{1}{n}\mathrm{Var}[R_i(t)] - \left(1 - \frac{\Delta t}{\mathrm{E}[R_i]^2}\right)^2 \mathrm{Var}[S_i(t)]\right]. \tag{2.10}$$

Grain growth necessarily involves the elimination of many grains as their volume is redistributed to the remaining grains. Simulation of an (R_i, S_i) pair ceases if R_i becomes less than or equal to zero. To maintain sufficient active grain realizations to construct a reliable histogram at the end of the simulation, the size distribution of active grains is re-sampled with replacement if the fraction of active grains drops below some specified fraction of the initial number of realizations. Since each realization is sensitive only to itself and the statistics of the global population of grains, re-sampling does not affect the overall results.

The starting grain sizes are drawn from a normal distribution with unit mean. Across a suite of simulations, we alter the initial variance of grain size between $\sim 10^{-4}$ and $\sim 10^{-1}$ to investigate the evolution toward the self-similar state. We use a time step $\Delta t = 10^{-5}$, which was determined by testing for converged statistics of the global set of grains (see Appendix 2.B). Assuming that a grain may only interact with its neighbours, the number of grains within each local environment n should be approximately the average number of faces of a grain plus one, to account for the grain itself. For space filling tetrakaidecahedra n is 15 (Thomson, 1887) and for random

Voronoi polyhedra n is 16.5 (Wakai et al., 2000). We take $n = 16$ as a reference case.

2.3 Results

The only adjustable parameter in our model is the number of grains within each local environment n. First, we explore the kinetics and grain-size distributions that result if n is set to the reference value of 16. Then we explore the effect of n on the predicted grain-size distributions, using a suite of simulations with values of n between 4 and 64, which all begin with the same normal distribution of grain size with unit mean and variance 0.03.

A key test of our model is whether it evolves to a self-similar state. If the simulation achieves self-similarity, then normalised statistics such as the coefficient of variation should be constant and histograms of grain size normalised by the mean should be independent of time. The coefficient of variation, plotted in Figure 2.1, converges to $c_v = 0.40$ by $t = 5$ for all initial conditions used, indicating that self-similarity is achieved and is stable—at least over the range of model times considered. This value is slightly higher than that obtained by Hillert ($c_v = 0.35$) (Hillert, 1965). The time taken in the transient towards self-similarity changes with the initial variance of the grain-size distribution. Tighter initial distributions require a longer transient to reach self-similarity. Other normalised statistics also converge to a constant value. For example, the ratio of the mean-field radius to the mean grain size converges to $R_m/\mathrm{E}[R_i] = 1.2$, which is higher than the value of 1.125 obtained in a pure Hillert model.

Histograms of grain size normalised by the mean also converge to a self-similar state. This convergence occurs following an initial transient in all of our simulations during which the normalised distribution broadens. Figure 2.2 compares the distribution obtained under our model (with $n = 16$) with the histogram from a pure Hillert

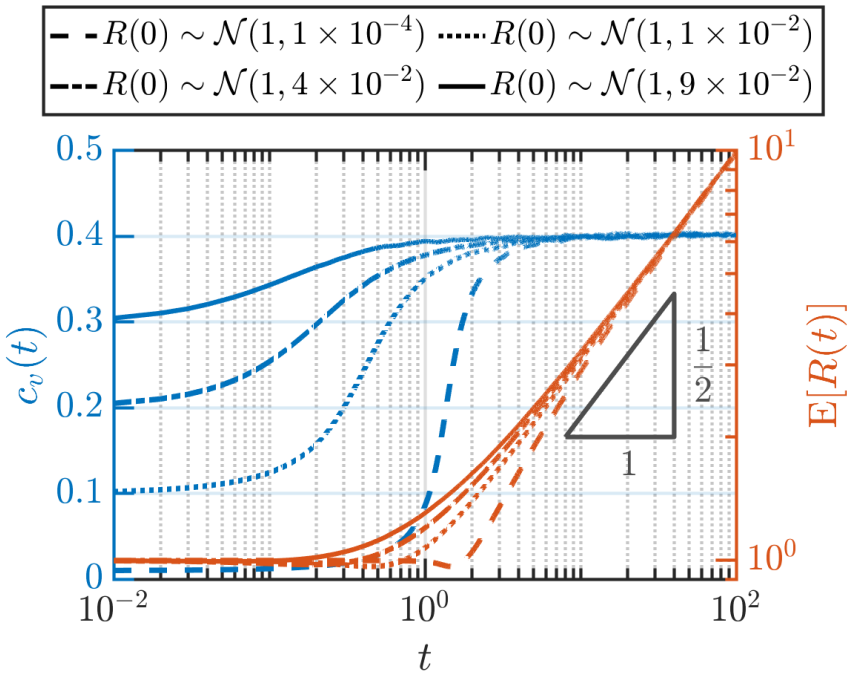

Figure 2.1: Time evolution of the coefficient of variation (left axis, blue) and mean grain size (right axis, red) for different starting distributions. These simulations were performed with $n = 16$. The coefficient of variation converges to a value of 0.4, indicating that self-similarity is achieved. Once self-similarity of the grain-size statistics are achieved, the mean grain size converges to a square root of time relationship.

model. In contrast to the Hillert distribution that is left skewed, our distribution is approximately symmetrical about the mean. In addition, our distribution is broader than the Hillert distribution. In the Hillert distribution, 99.9% of grains are smaller than 1.8E$[R_i]$, whereas in our distribution, the equivalent percentile is located at 2.2E$[R_i]$.

These differences from the prediction of the Hillert model mean that our distribution gives a better fit to histograms of distributions from experiments and numerical simulations that resolve and evolve the grain structure. In Figure 2.2, our distribution is compared to experimental data from iron (Zhang et al., 2004; Ullah et al., 2017; Zhang et al., 2018), steel (Liu et al., 2002), IN100 (Groeber et al., 2008), and β-titanium (Rowenhorst et al., 2010), gathered by serial sectioning and diffraction contrast tomography, and data from numerical simulations applying the vertex-vertex

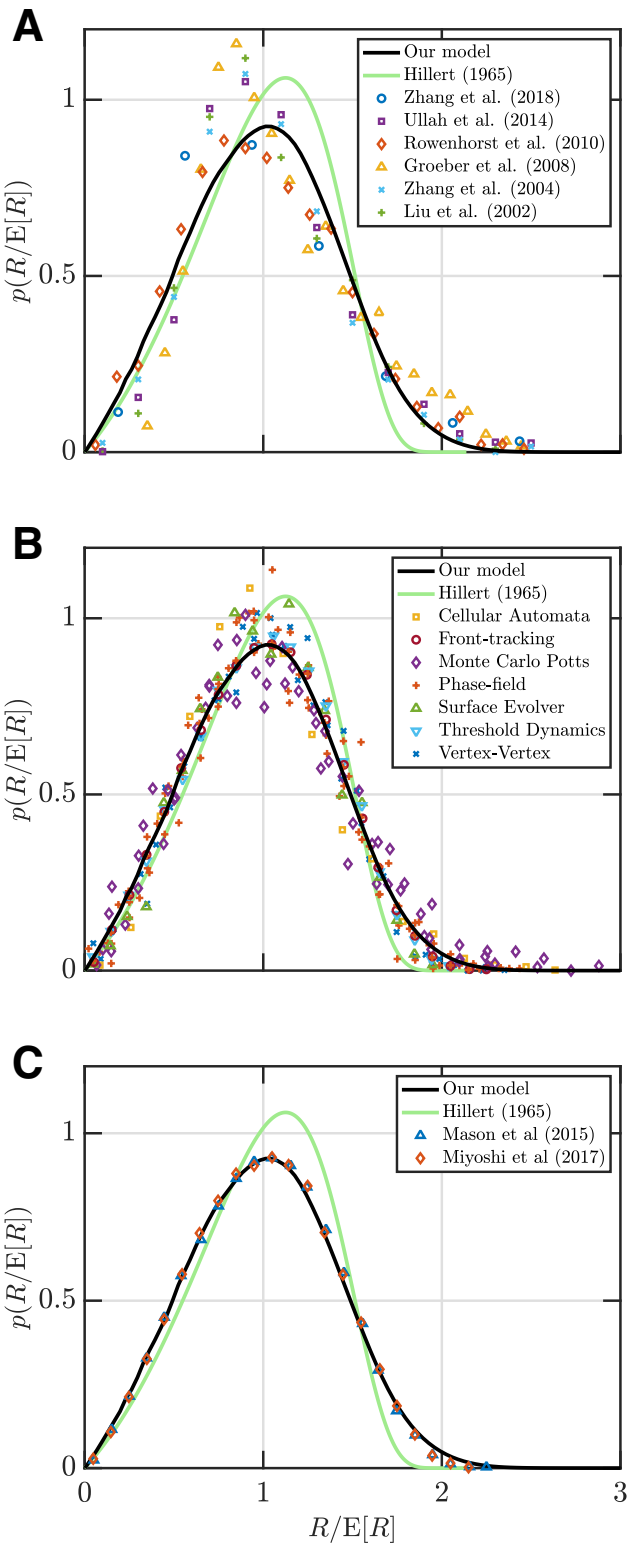

(*Caption overleaf.*)

Figure 2.2 *(previous page)*: Comparison of the predicted probability distribution of grain size normalised by the mean in our model compared to the predictions of Hillert's model and observations from (A) physical experiments and (B and C) numerical simulations. Our distribution was obtained from a model with $n = 16$. Experimental data is taken from (Liu et al., 2002; Zhang et al., 2004; Groeber et al., 2008; Rowenhorst et al., 2010; Ullah et al., 2014; Zhang et al., 2018). The histograms of distributions from numerical simulations derive from a wide variety of approaches: the vertex-vertex method (Fuchizaki et al., 1995; Weygand et al., 1999), the threshold dynamics method (Elsey et al., 2010), surface evolver (Wakai et al., 2000), the phase-field method (Krill and Chen, 2002; Kamachali and Steinbach, 2012; Kim et al., 2014; Miyoshi et al., 2017), the Monte Carlo Potts method (Kim et al., 2005; Zöllner and Streitenberger, 2006; Ullah et al., 2017), cellular automata (Ding et al., 2006) and a front tracking method (Mason et al., 2015). In (C) our predicted distribution is compared with the distributions from the state-of-the-art simulations of Mason et al. (2015), who use a front tracking algorithm, and Miyoshi et al. (2017), who use the phase-field method.

method (Fuchizaki et al., 1995; Weygand et al., 1999), the threshold dynamics method (Elsey et al., 2010), surface evolver (Wakai et al., 2000), the phase-field method (Krill and Chen, 2002; Kamachali and Steinbach, 2012; Kim et al., 2014; Miyoshi et al., 2017), the Monte Carlo Potts method (Kim et al., 2005; Zöllner and Streitenberger, 2006; Ullah et al., 2017), cellular automata (Ding et al., 2006) and a front tracking method (Mason et al., 2015). The mode of the experimental histograms is closer to the mode of our distribution than the Hillert distribution, and the tail of the experimental histograms compares favourably to our distribution. Our distribution lies within the envelope of histograms from numerical simulations; the mode and the tail of our distribution matches the histograms from numerical simulations.

Finally, in Figure 2.2C, we highlight the comparison with two state-of-the-art numerical simulations, performed by Mason et al. (2015) and Miyoshi et al. (2017). Mason et al. (2015) applied a front-tracking method that solves the MacPherson-Srolovitz equation (MacPherson and Srolovitz, 2007), which expresses the rate of volume change in terms of topological information, to high accuracy. Miyoshi et al. (2017) apply the phase-field method to a microstructure with a large number of grains

and take care to ensure that a true steady-state distribution is obtained. These simulations provide the most accurate available estimates of the steady-state grain-size distribution developed in normal grain growth and hence are the best distributions against which to compare our results. Our distribution is in excellent agreement with the distributions from Mason et al. (2015) and Miyoshi et al. (2017).

A fundamental observation from experiments and numerical simulations is that the mean grain size grows like the square root of time (Rios and Zöllner, 2018). Under our model, the mean grain size, plotted in Figure 2.1 as a function of time, grows like the square root of time following an initial transient. The transient extends to $t \approx 10$, which is comparable to the time taken for the coefficient of variation to converge to its value in the self-similar state. The length of the transient in the evolution of mean grain size depends on the initial variance of the grain-size distribution; the lower the initial variance, the longer the transient. Following the transient, the mean grain size in all simulations is well approximated by

$$\mathrm{E}[R_i(t)]^2 = a + bt. \tag{2.11}$$

The slope of this fit, $b = 0.98$, is greater than the value of 0.79 obtained under a pure Hillert model, indicating that the growth rate of mean grain size is increased by accounting for the heterogeneity in grain environments.

Figure 2.3 compares normalised, self-similar grain-size distributions obtained from simulations with different choices of n. As n increases, the mode of the distribution shifts to the right and the tail of the distribution shrinks, such that the distribution moves closer to the Hillert distribution. In the limit of large n, where the local environment encompasses the total population of grains, our model reduces to the Hillert model and so the Hillert distribution is expected. Hence the self-similar distributions that result from our model form a family that depend on the number of grains within

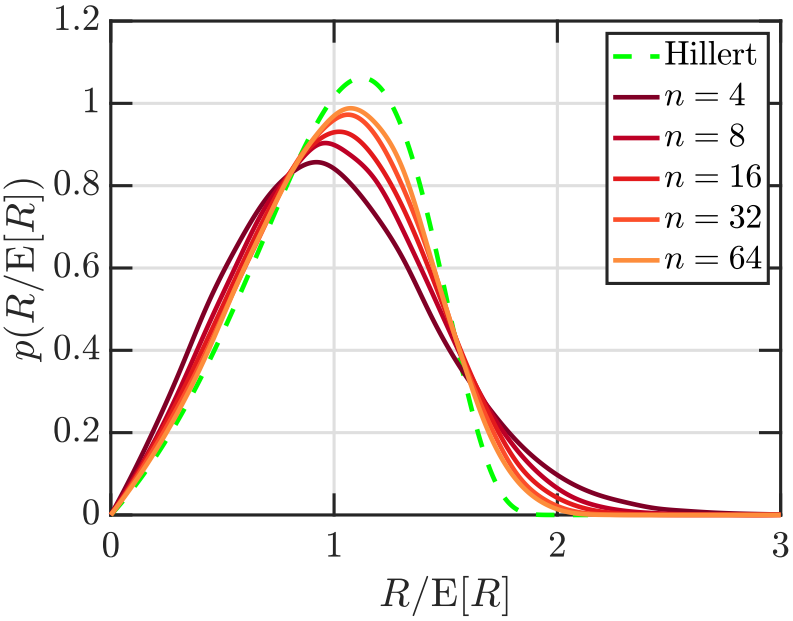

Figure 2.3: Normalised grain-size distributions from simulations with different choices of the number of grains within a local environment n, compared to the Hillert distribution. The simulations are initialised with normally distributed grain size with unit mean and variance of 0.3, and run until the distribution of grain size reaches steady state. As n increases, the distribution approaches the Hillert model.

the local environment and approach the Hillert distribution as n increases.

2.4 Discussion

2.4.1 Self-similar distribution

Our model, in which the Hillert theory is augmented with a random variable describing each grain's local environment, reproduces the key observations of normal grain growth: square-root of time kinetics and a self-similar distribution of grain size. The grain-size distribution it produces, with $n = 16$ chosen by analogy with space-filling polyhedra, is in better agreement with distributions from experimental data than the Hillert distribution and is in good agreement with distributions from numerical simulations. Furthermore, our distribution is in excellent agreement with the distri-

butions derived by the state-of-the-art numerical simulations of (Mason et al., 2015) and (Miyoshi et al., 2017). The improved agreement with experimentally derived histograms suggests that accounting for heterogeneity in grain environments represents the leading-order correction to Hillert's model.

Notwithstanding this improvement over the Hillert distribution, the mode of the experimental distributions is smaller than the mode obtained under our model. This inconsistency could result from systematic bias present in experimental distributions: smaller grains may be under-counted because of finite image resolution or due to the serial sectioning process applied to obtain three-dimensional information. As the distributions are normalised by an overestimated mean, this bias will act to change the shape of normalised histograms of grain size at small grain sizes and shift the mode of these histograms to smaller values. Furthermore, whilst experimental investigations attempt to isolate normal grain growth, there may be a number of processes acting in real materials that modify the kinetics of grain-size evolution away from idealised models. For example, the effects of anisotropy in grain-surface energy or mobility (e.g., Kazaryan et al., 2002), solute drag (e.g., Kim and Park, 2008), pore drag (e.g., Karato, 1989), and Zener pinning by unintended secondary phases (e.g., Nes et al., 1985) may act to modify grain-growth kinetics and consequently modify the distribution of grain size. As numerical simulations exclude these processes, they present a more direct test of our hypothesis.

A potential explanation for the broader shape of our distribution is that a correlation develops between R_i and S_i such that our model is effectively a correlation-field theory, similar to that proposed by (Marthinsen et al., 1996). A correlation may develop under our model because grains with relatively large local environments are more likely to shrink in size. The relationship between local environment radius and grain size is explored in Figure 2.4. A weak relationship exists between grain size and local environment radius, with the same sense as the correlation that Marthinsen

et al. (1996) observed in their Monte Carlo Potts model. However, local environment radius varies little with grain size compared to the variance of local environment radius at any given grain size. Our results thus indicate that the correlation between grain size and local environment is not a significant control on normal grain growth.

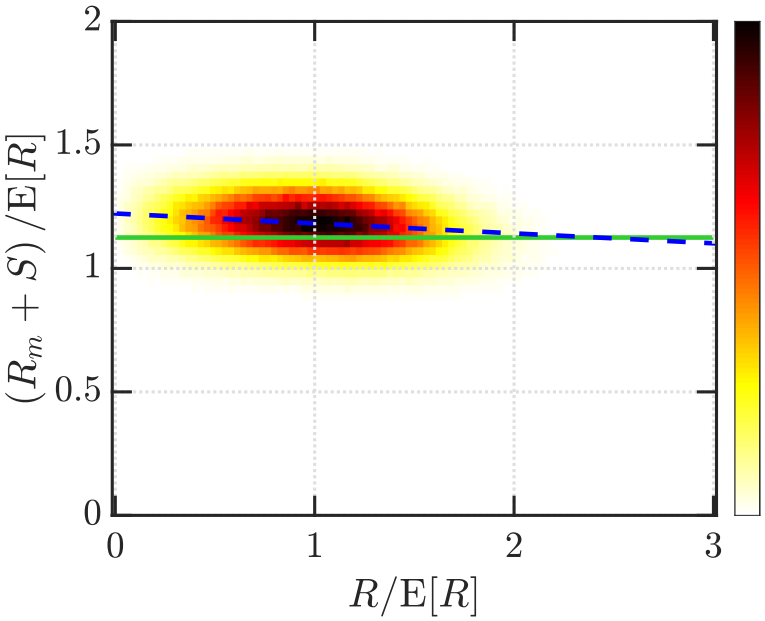

Figure 2.4: Heat map of grain size vs. local environment radius for the results of a simulation that achieved a self-similar state. In this simulation, n was equal to 16. The mean-field radius under the Hillert model is plotted as a solid green line. A linear fit is plotted as a dashed blue line. The heat map colour indicates the relative density of points, with white indicating low density and black indicating high density.

The true role of the local environment variable can be investigated by examining the grain-size trajectories of individual grains, plotted in Figure 2.5. For grains that are initially smaller than the mean, the local environment radius has little effect; instead the self-curvature term in Equation (2.7) dominates the evolution of grain size. For grains that are larger than the mean, the local environment radius dominates the evolution of grain size and a grain's self-curvature is unimportant. Since the local environment radius performs a random walk, it causes grains that are larger than the mean to also undergo a random walk. This mixing of deterministic evolution, for grains smaller than the mean, and random perturbations, for grains larger than the

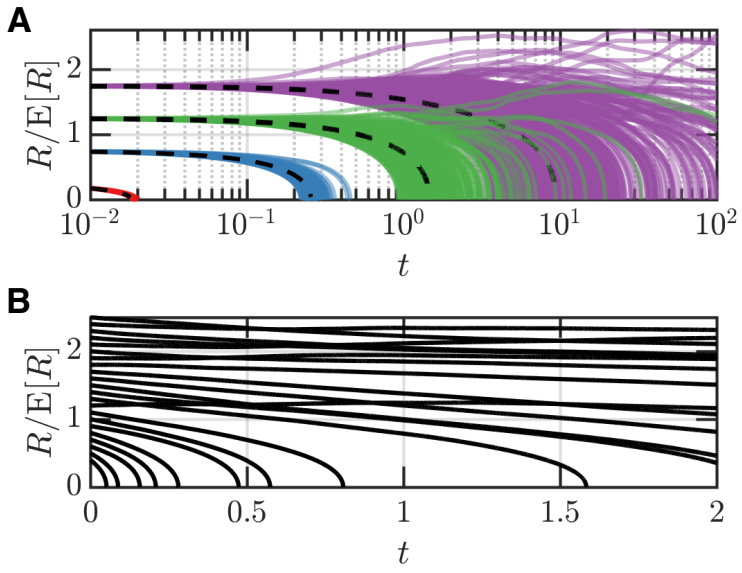

Figure 2.5: (A) Realizations of $R_i(t)$ normalised by the mean grain size compared to trajectories obtained under the Hillert model. For the simulation of these trajectories, n was taken to be equal to 16. Time t is relative to an initially self-similar state such that the trajectories are representative of self-similar evolution. Coloured lines show the evolution under our model for four different initial grain sizes $R_i(0) = 0.25, 0.75, 1.25, 1.75$. Hillert trajectories are plotted as black-dashed lines. For grain sizes that are small relative to the mean, the local environment effect is small and trajectories follow the trajectory of the Hillert model. For larger grains, the local environment effect may dominate and trajectories deviate from the Hillert trend. A logarithmic scale is used to highlight behaviour of trajectories to high model times. (B) Set of realisations of R_i normalised by the mean grain size once a self-similar distribution has been obtained, for $n = 16$. Compare to Figure 7b of Srolovitz et al. (1984).

mean, matches the observations made by Srolovitz et al. (1984) of grain-size trajectories in a Monte Carlo simulation of grain growth (compare Figure 7b of Srolovitz et al. (1984) with our Figure 2.5B).

In the Hillert model, the stability argument applied in the derivation of the grain-size distribution imposes an upper cut-off on its extent. This cut-off limits the range of the Hillert distribution and leads to the discrepancy between the Hillert distribution and observations. In our model, larger grains perform a random walk, and so the distribution extends to higher values of normalised grain size, leading to better agreement with distributions from experiments and numerical simulations.

2.4.2 Effect of local environment size

Simulations that explore the effect of the local environment size indicate that as n increases, the self-similar distribution approaches the Hillert distribution (Figure 2.3). Within the Hillert model, all grains in the global set form part of the local environment of any given grain. In our model, this corresponds to the limit of large n, where n becomes equal to the total number of grains considered. Mathematically, as n becomes large, the variance of S_i given by Equation (2.4) becomes small and so the magnitude of S_i shrinks towards zero. In the case that S_i is negligible, our Equation (2.1) reduces to the Hillert model. Hillert's model therefore represents an asymptotic limit of our model for large n.

The family of distributions generated by varying n can be compared against previously published distributions. The distributions derived by Rios (1999) agree well with results from experiments and computer simulations (Rios et al., 2006). Rios obtained a one-parameter family of distributions that depend on a parameter ν, with $\nu = 4$ corresponding to the Hillert distribution. Indeed, the Rios distribution arises by relaxing a stability argument that Hillert applied to constrain ν to be 4. Values of ν between 2 and 3.6 produce distributions that compare favourably against observed distributions (Rios and Glicksman, 2006*a*).

To compare against the Rios distributions, we determine the value of ν that generates the Rios distribution that most closely approximates our own distribution for a given n. To measure the closeness of two distributions, we define the statistical divergence between our model and the Rios distribution in terms of the total variation distance as

$$D(\nu, n) = \frac{1}{2} \int |p(x; n) - q(x; \nu)| \, \mathrm{d}x, \tag{2.12}$$

where $D(\nu, n)$ is the statistical divergence, x is the grain size normalised by the

mean, $p(x;n)$ is our own distribution for a given n and $q(x;\nu)$ is the Rios distribution as defined in Rios et al. (2006) for a given ν. The total variation distance is zero for distributions that match perfectly and is unity for distributions that do not overlap. We approximate the integral in Equation (2.12) using the trapezium rule and minimise $D(\nu, n)$ using MATLAB's *fminsearch* function to find the value $\nu = \nu^*$ that best approximates our own distribution at a fixed value of n.

For all of the values of n that we explore, there is a Rios distribution that matches our distribution. In each case, the minimised total variation distance is below 3%, indicating a correspondence between the two distributions. Figure 2.6A presents a comparison between our distribution for $n = 16$ and the best-fit Rios distribution, which has ν^* equal to 3.1. The relationship between the number of grains in a local environment n and the value of ν^* that generates the best-fitting Rios distribution is explored in Figure 2.6B. This relationship is approximated by

$$\nu^* = 4 - 3.6/\sqrt{n}. \tag{2.13}$$

This correspondence can be further explored by examining the steady-state grain-size kinetics. In Rios et al. (2006)'s approach, the rate of change of the square of the mean-field radius depends inversely on the parameter ν. We recast this prediction to depend on the local environment n using Equation (2.13) and compare it against the steady-state grain-size kinetics observed in our simulations in Figure 2.6C. The observed kinetics closely match the predicted kinetics derived using Equation (2.13), further highlighting the correspondence between the steady-state results of our stochastic model and the predictions of the phenomenological model of Rios et al. (2006). This correspondence between the distributions and the kinetics of the mean-field-radius suggests that ν might be interpreted as representing the average number of grains

adjacent to each individual grain. This interpretation is a testable prediction of our model.

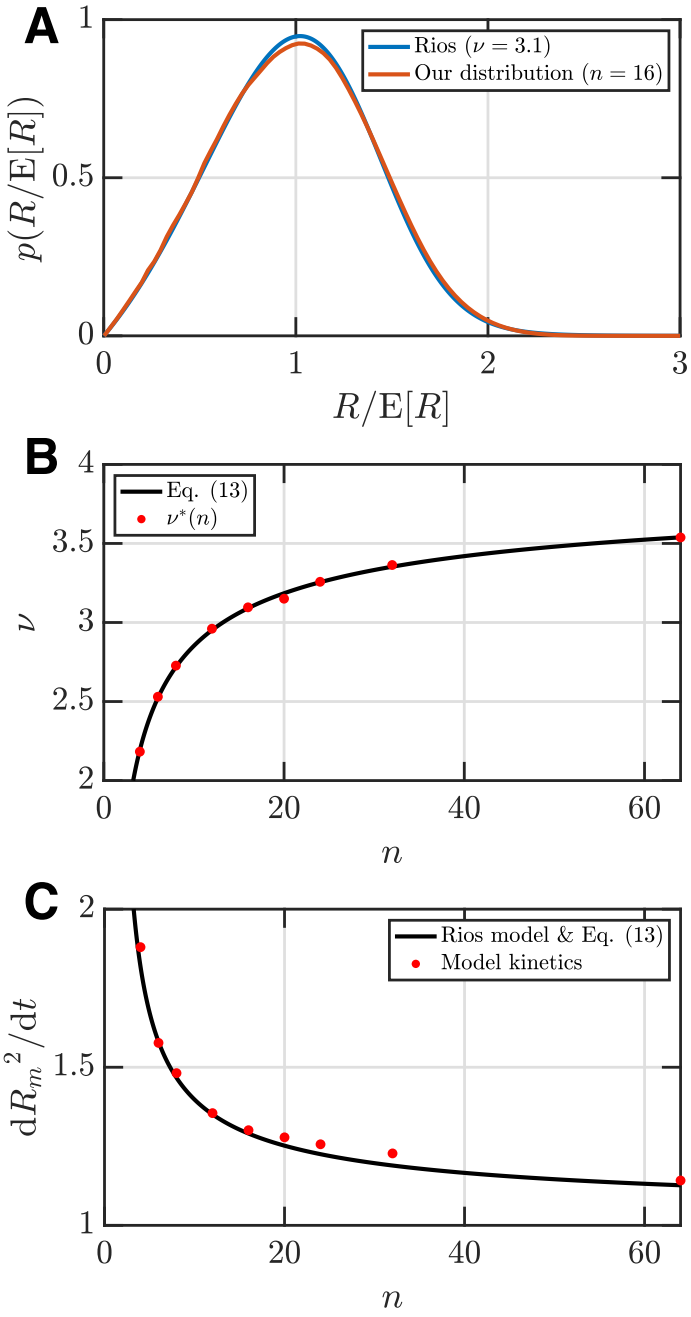

(*Caption overleaf.*)

Figure 2.6 *(previous page)*: (A) Comparison of the distribution obtained under our model with $n = 16$ and the most closely matching Rios distribution with $\nu = 3.1$. (B) The parameter $\nu*$ that generates the best-fitting Rios distribution against the size of the local environment n. The black line is a fit to ν^* given by Equation (2.13). (C) The rate of change of the square of the mean-field-radius against local environment n. The predicted kinetics from Rios et al. (2006) are recast in terms of the local environment n using Equation (2.13) (black line). The kinetics observed (red dots), calculated using a finite-difference approximation across a time step, match the predicted kinetics.

2.4.3 Model limitations

A critical assumption applied in our model is that the sampling distribution used to describe the probability density of the local environment radius $R_m + S_i$ can be approximated with a normal distribution. We test this assumption by subsampling the grains from one simulation to construct grain subsets, taking n to be equal to 16. We then calculate the local environment radius of each subset as $\mathrm{E}_i[{R_i}^2]/\mathrm{E}_i[R_i]$. This quantity is indeed normally distributed, with the statistics given by our approximation in Equation (2.4) (see Appendix 2.C). In general, the accuracy of this approximation will depend on the underlying distribution of grain size that is being sampled and the size of the local environment n, which determines the number of samples in each subset. Although our normal approximation for the sampling distribution holds well for the grain-size distributions we have considered, it may break down for arbitrary grain-size distributions far from steady state. In such cases, our model would not be applicable.

Another critical assumption is that the number of grains comprising any particular local environment is constant and equal to n. We have selected a reasonable value of n based on space-filling polyhedra. However, in practice, the number of faces and therefore the number of neighbours of a grain depends on the size of the grain, due to a size–topology correlation. Smaller grains should, in general, have fewer neighbours than larger grains and therefore smaller neighbourhoods. Consequently, the variance

in the local environment radius ought to be higher for smaller grains. Based on the observed size–topology relationships (e.g., Kamachali and Steinbach, 2012), we expect nearly an order of magnitude decrease in the variance of the local environment radius from the smallest to the largest grains. However, the impact of heterogeneity is not felt equally by all grains. As is evident in Figure 2.5, the evolution of smaller grains is dominated by the self-curvature term in Equation (2.1); the effect of the local environment only becomes important once the grain size exceeds the mean. The neighbourhoods of the largest grains are expected to be approximately twice as big as the neighbourhoods of grains whose size is equal to the mean (Kamachali and Steinbach, 2012), leading to only a factor of two difference in the variance of the local environment radius between these two cases. In principle, the correlation between neighbourhood size n and grain size R_i should influence the statistics of the local environment radius. However, over the range of grains for which the local environment radius matters, the impact of the size–topology correlation is limited. Future work could incorporate the dependence of neighbourhood size on grain size by altering the type of noise introduced by S to depend on the size of each grain directly.

2.4.4 Source of fluctuations

The source of fluctuations in stochastic models is typically assumed to be topological in nature (Pande and Moser, 2020; Mullins, 1998). If the full topological state of a three-dimensional grain is known, then the rate of change of its volume can be calculated exactly using the MacPherson-Srolovitz relationship (MacPherson and Srolovitz, 2007), which is deterministic. MacPherson and Srolovitz derive an approximation to this relationship, in which the rate of change of size of a grain is proportional to the difference between the square root of the number of its faces and a constant (MacPherson and Srolovitz, 2007) (see also a similar relationship due to Rios and Glicksman (2006*a*)). Events that modify the topological properties of

grains are expected to drive discrete changes in the growth rate of grains through this relationship. Such events are therefore a candidate source of noise in normal grain growth. For example, grain disappearances can alter the number of faces possessed by surrounding grains. Within our model, noise is calibrated to represent heterogeneity in the local environment of grains, which may be alternatively understood in terms of grain topology. The number of faces of a grain depends, in an average sense, on its relative size: smaller grains are expected to have fewer faces. Similarly, grains that are surrounded by smaller-than-average grains would be expected to have a greater number of faces. In our model, the local environment radius provides an average measure of the size of grains surrounding a given grain and therefore holds information that could be used to infer the topological properties of the grain. Consequently, local environments can be understood in topological terms; heterogeneity in local environments can be identified with heterogeneity in topological properties. This reasoning can be applied to the trajectories obtained under our model. In Figure 2.5B, there exists a grain trajectory that does not follow the (Hillert-like) trend of the grains that have a similar size. Instead of shrinking relative to the mean, its size relative to the mean grain size remains approximately constant. The reason for this is that it has a smaller local environment radius than the average, which stabilises it according to Equation (2.1). From the topological perspective, we can infer that due to its comparatively smaller local environment radius, the neighbouring grains are smaller, and so the number of faces that our grain possesses is correspondingly larger than would otherwise be expected for a grain of its size. According to the approximate MacPherson-Srolovitz equation, its volume (and therefore radius) is stabilised by its topology, consistent with our results.

The noise supplied to our model by the Ornstein-Uhlenbeck process for S_i differs from the white noise incorporated into previous stochastic models of normal grain growth (Pande and Dantsker, 1990; Pande et al., 2008; Pande and McFadden, 2010;

Pande and Moser, 2020). A key distinction lies in the time-correlation of the noise. As the noise applied in previous models is white noise, the time-correlation function in these models is a Dirac delta. In contrast, in our model noise is supplied to the grain-size kinetics by the local environment radius. The local environment radius is generated by an Ornstein-Uhlenbeck process that is correlated on a timescale τ as a result of the drift term in Equation (2.6). We have chosen this timescale to be the macroscopic timescale of normal grain growth. The fundamental assumption involved in the application of white noise is that the 'collisions' (in analogy to Brownian motion) driving the stochastic component are both fast and uncorrelated. These collisions are understood to act on a microscopic timescale that is much smaller than the macroscopic timescale, such that in the limit of the microscopic timescale tending to zero, a Dirac delta time correlation function is obtained. Mullins (1998) argued that the events constituting the collisions of normal grain growth would occur on the macroscopic timescale, and so could not give rise to a fluctuation term described by white noise. This critique does not apply to our model in which the noise supplied is correlated on the macroscopic timescale, and so can reasonably represent the random influence of the events described by Mullins.

Pande and Moser (2020) argue against Mullins's criticism of the application of a white noise term by applying a more global perspective. They assert that each collision event that drives the stochastic component of normal grain growth affects the entire set of grains. Consequently, as the number of grains in the system becomes large, the timescale for an individual event that may affect all grains becomes small, justifying the introduction of a white noise term. This justification cannot apply to the stochastic component of our model, as we have emphasised a more local perspective. In our model, grains are screened from the global environment and are influenced only by the grains with which they can exchange mass. As a result, the influence of any given event is more limited. This difference in perspective between local and

global scales constitutes a key distinction between our model and previous stochastic models.

There are other distinctions between our approach and previous stochastic models that apply white noise to the grain-growth rate. The amplitude of noise in our model is constrained by association with a specific hypothesis about heterogeneity in local environments. In contrast, in models that apply white noise, the amplitude of the white noise is a free parameter because no individual physical process is directly identified as the key contributor to the noise term. Given these differences between our model and other stochastic models of normal grain growth, it is surprising that the results of both approaches seem to be equivalent. Indeed, Pande and Moser (2020) compare the approximate solutions found by Pande and McFadden (2010) for their white-noise-driven model to the distributions obtained by the phase-field simulation of Miyoshi et al. (2017), the experimentally-derived distribution of Rowenhorst et al. (2010) and the phenomenological distribution due to Rios et al. (2006), as we have done. Pande and Moser find that their distribution is in agreement with the distributions obtained by Miyoshi et al. and Rowenhorst et al., and is congruent with the Rios distribution, as we have found with our distribution. Furthermore, as Pande and Moser (2020) note, the approximate grain-size distribution derived from their white-noise-driven model is analytically equivalent to the grain-size distribution that Streitenberger and Zöllner (2006) derived from their modified mean-field theory, which they calibrated against observations from the simulations of Zöllner and Streitenberger (2006). The close correspondence between the distributions obtained here, white-noise-driven models, and modified mean-field theories raises the question. Why do these different approaches result in such similar grain-size distributions?

2.5 Conclusions

By accounting for heterogeneity in the local environment of grains and its resultant effect on mass exchange between grains, our model resolves the discrepancy between the Hillert distribution and observations. It also matches the key characteristics of normal grain growth. The improved fit is achieved because heterogeneity in local environments causes relatively large grains to undergo a random walk in grain size, allowing some of these grains to grow larger than is possible under the Hillert model. Our distribution is therefore broader than Hillert's and provides a better match to observed distributions. It is in excellent agreement with distributions from state-of-the-art simulations. Our analysis suggests a physical meaning for the fitting parameter in the Rios distribution in terms of the size of the local environment.

The noise we have introduced into our model is fundamentally different to the unconstrained white noise typically introduced into stochastic models of normal grain growth. The amplitude of the noise in our model is determined by association with a hypothesis of heterogeneity in the local environments of grains. This hypothesis can be alternatively understood in terms of heterogeneity in grain topology. Furthermore, the noise in our model is correlated on the timescale of normal grain growth. It is therefore interesting that the grain-size distribution obtained by our model is similar to the distributions that develop in these other stochastic models.

Appendix

2.A Calculation of $\Omega(t)$

Requiring that the small sample statistics of S_i hold at the end of a timestep implies that

$$\mathrm{Var}[S_i(t+\Delta t)] = \frac{1}{n}\mathrm{Var}[R_i(t)]. \tag{2.A.1}$$

Under the Euler-Maruyama scheme, Equation (2.8) gives

$$S_i(t+\Delta t) = \left(1 - \frac{\Delta t}{\mathrm{E}[R_i(t)]^2}\right) S_i(t) + \Omega(t)\sqrt{\Delta t}\mathcal{N}(0,1). \tag{2.A.2}$$

Consequently, the variance of S_i following a timestep is given by

$$\mathrm{Var}[S_i(t+\Delta t)] = \left(1 - \frac{\Delta t}{\mathrm{E}[R_i]^2}\right)^2 \mathrm{Var}[S_i(t)] + \Omega(t)^2\Delta t. \tag{2.A.3}$$

By equating Equations (2.A.1) and (2.A.3), we can determine $\Omega(t)$ at any timestep such that Equation (2.4) holds,

$$\Omega(t)^2 = \left[\frac{1}{n}\mathrm{Var}[R_i(t)] - \left(1 - \frac{\Delta t}{\mathrm{E}[R_i]^2}\right)^2 \mathrm{Var}[S_i(t)]\right] / \Delta t, \tag{2.A.4}$$

which is Equation (2.10) in the main text.

2.B Choice of Δt

One method of choosing the appropriate time step Δt is to compare histograms of grain size normalised by the mean produced by the model with different choices of Δt. Figure 7A shows histograms of grain size normalised by the mean at $t = 1$, with the same initial condition of normally distributed grain size with mean equal to one and initial variance of 0.3, for a range of possible time steps. The histogram with $\Delta t = 0.1$ differs significantly from the other histograms, with a relative excess of grains of size close to zero. For $\Delta t = 0.01$ and smaller, the histogram converges to a shape independent of the choice of Δt, indicating that a Δt smaller than 10^{-3} is be appropriate.

Another method of evaluating the choice of Δt is to assess the relative error between the assumed statistics of S_i given by Equation (2.4) and the observed statistics of S within the model. Time series of the relative error in the variance of S for different choices of Δt are plotted in Figure 7B. The magnitude of the relative error decreases with decreasing Δt until $\Delta t = 10^{-5}$, after which decreasing the time step does not significantly reduce the magnitude of relative error, indicating that an appropriate choice of time step is 10^{-5}.

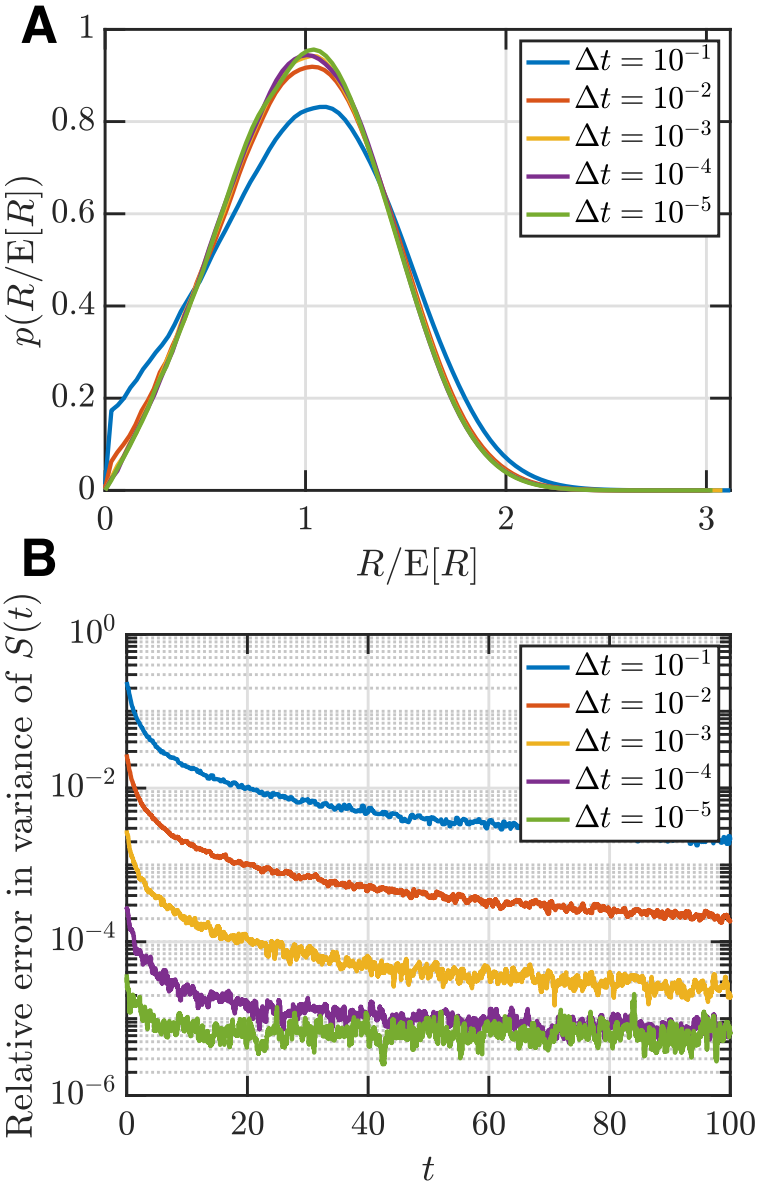

Figure 7: (A) Histograms of grain size normalised by the mean, obtained from models run with different choices of time step Δt (see legend). All model runs were started with the same initial distribution of grain size (normally distributed with unit mean and variance of 0.03). (B) Time series of relative error in the variance of $S(t)$ from models with different choices of time step Δt. All model runs were started with a normal distribution of grain size with unit mean and variance of 0.03. The relative error in variance of $S(t)$ was calculated as the difference between the expected variance of $S(t)$ from Equation (2.4) and observed variance of $S(t)$ normalised by the expected variance.

2.C Assessing the assumption that S is normally distributed

The small-sample statistics of the local environment radius can be assessed by subsampling with replacement the observed grain sizes R_i from the results of a model. The R_i resulting from a single model run that converged to steady state are subsampled with replacement to produce 10^6 sets of 16 samples. The local environment radius $R_m + S_i$ is then calculated for each set of $n = 16$ samples according to $\mathrm{E}_i[{R_i}^2]/\mathrm{E}_i[R_i]$. The histogram of the local environment radius so calculated is compared in Figure 8 to the distribution of $R_m + S_i$, where S_i is assumed to follow the statistics given by Equation (2.4). The distribution obtained by subsampling R_i agrees well with the assumed distribution, and the relative error in the mean and variance between the distributions is less than a percent. This validates the approximation used in Equation (2.4).

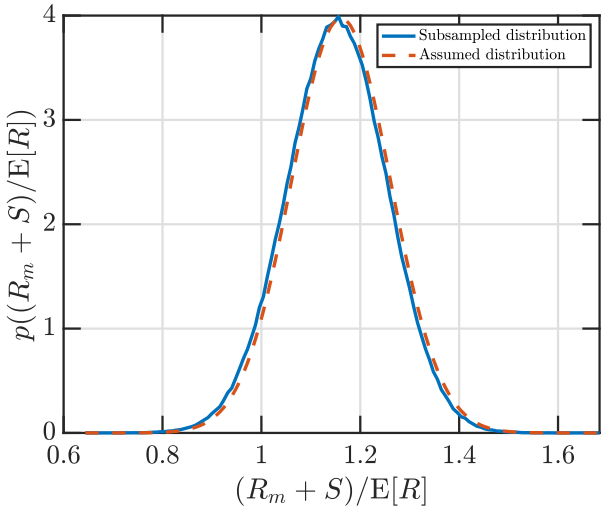

Figure 8: Comparison of the assumed distribution of S given by Equation (2.4) and the distribution obtained by subsampling a converged model to produce 10^6 sets of local environments containing $n = 16$ samples, and calculating the local environment radius directly.

Statement of Authorship for joint/multi-authored papers for PGR thesis

To appear at the end of each thesis chapter submitted as an article/paper

The statement shall describe the candidate's and co-authors' independent research contributions in the thesis publications. For each publication there should exist a complete statement that is to be filled out and signed by the candidate and supervisor **(only required where there isn't already a statement of contribution within the paper itself).**

Title of Paper	The role of grain-environment heterogeneity in normal grain growth: A stochastic approach.
Publication Status	x Published □ Accepted for Publication □Submitted for Publication □Unpublished and unsubmitted work written in a manuscript style
Publication Details	Breithaupt, T., Hansen, L. N., Toppaladoddi, S., & Katz, R. F. (2021). The role of grain-environment heterogeneity in normal grain growth: A stochastic approach. *Acta Materialia*, *209*, 116699.

Student Confirmation

Student Name:	Thomas Breithaupt		
Contribution to the Paper	Developed the model of stochastic grain growth, co-wrote the code to simulate grain growth with my supervisor (Richard Katz) and wrote the manuscript.		
Signature	T.P.Breithaupt	Date	11th November 2021

Supervisor Confirmation

By signing the Statement of Authorship, you are certifying that the candidate made a substantial contribution to the publication, and that the description described above is accurate.

Supervisor name and title: Richard F Katz, Professor of Geodynamics
Supervisor comments Tom is the lead author of this study because he conceived the hypothesis, developed the methodology, obtained the results, wrote the manuscript and handled the revision process.

Signature. 	Date	11 Nov 2021

This completed form should be included in the thesis, at the end of the relevant chapter.

Chapter 3

Dislocation theory of steady and transient creep in olivine

This work has been prepared for publication. I have made minor adjustments to the formatting and content of this work to put it within the context of this thesis..

3.1 Introduction

Many problems in the materials, engineering and geosciences require assessment of the mechanical behaviour of crystalline solids at extremely low strain rates. These include applications to gas turbines (Whittaker et al., 2013), power stations (Wilshire and Scharning, 2008), glaciers (Minchew et al., 2018), and Earth's interior (Pan et al., 2021). Understanding the mechanical properties of materials in these settings is crucial for predicting the creep-limited lifetime of engineering components and the response of the solid Earth to changing surface loads, such as shrinking ice sheets. The small strain rates in these settings are impractical or impossible to explore in laboratory experiments. Therefore, predictions are typically made by extrapolation from experiments performed at much higher strain rates. Confidence in such extrapolations should be based on a clear understanding of the physics of deformation. However, steady-state deformation data are largely rationalised using phenomeno-

logical power-law fits (Spigarelli and Sandström, 2018), and transient strain rates are often modelled using approaches that are not rooted in the underlying physics (Hansen et al., 2021). At this point, there is no physics-based model of steady-state and transient deformation that is self-consistent across multiple deformation regimes.

Deformation of crystalline solids occurs by the motion of crystal defects. In this study, we examine the role of line defects—dislocations—within the crystal lattice. Deformation as a consequence of dislocation motion has been divided into categories including low-temperature plasticity, dislocation creep, and grain-size-sensitive dislocation creep, each of which has been modelled as a physically distinct mechanism (e.g., Hirth and Kohlstedt, 2003). Going beyond these models of steady-state creep, the evolution of dislocation microstructure controls transient strain rates at low strains (Blum et al., 2002) and other classical features of deformation such as the Hall-Petch effect (Dunstan and Bushby, 2014) and the Bauschinger effect (Hansen et al., 2019). Here, we present a unified, physics-based, quantitative description of all these features of deformation associated with dislocation motion.

Deformation due to dislocation motion is sensitive to the density of dislocation lines within crystals. We therefore construct a model for evolution of dislocation density that makes physics-based, testable predictions about deformation at both low and high strain rates. The classical theory for dislocation-density evolution in the materials sciences is the Kocks-Mecking-Estrin (KME) model, which has been used to model low-temperature deformation of metals including silver, copper, aluminium, and nickel (Kocks, 1966, 1976; Essmann and Mughrabi, 1979; Mecking and Kocks, 1981; Estrin and Mecking, 1984; Estrin, 1998). This theory is derived from the hypothesis that dislocation density increases due to dislocation storage, a geometric description of the increase in dislocation-line length during dislocation glide, and decreases due to dynamic recovery, a description of strain-dependent dislocation annihilation that is thought to dominate at low temperatures (Nix et al., 1985). However,

extensions of the KME model to high temperatures are problematic because they exclude key aspects of dislocation physics, incorporating either phenomenological parameterizations (Kocks, 1976; Mecking and Kocks, 1981) or relying on an empirical scaling between the applied stress and dislocation density (Sandström and Hallgren, 2012; Spigarelli and Sandström, 2018).

We demonstrate that laboratory data from experiments at low and high temperatures can be explained in a self-consistent manner by accounting for two additional aspects of dislocation physics. First, we augment the KME theory with a model for static recovery that describes the high-temperature, time-dependent annihilation of dislocations. In this model, we emphasise the role of fast-diffusion pathways in dislocation annihilation. Second, we couple the theory of dislocation evolution to a flow law that explicitly describes the competing roles of dislocations as both carriers of deformation and generators of stress fields that act to oppose deformation. The combined model provides a parsimonious, physics-based explanation of (i) yield stresses at low temperatures, (ii) steady-state and transient creep at high temperatures, (iii) the scaling between dislocation density and stress, (iv) kinematic hardening, (v) the Bauschinger effect, and (vi) the Hall-Petch effect.

All of these processes and phenomena are relevant to olivine (Hirth and Kohlstedt, 2003, 2015; Hansen et al., 2019, 2021), a mineral that controls the strength of Earth's upper mantle. Olivine has three key advantages in testing our approach. First, its dislocation density can be readily measured using an oxidation-decoration technique (Kohlstedt et al., 1976) and there are many published experiments against which to compare model predictions (Durham et al., 1977; Bai and Kohlstedt, 1992; Kohlstedt and Goetze, 1974; Farla et al., 2011; Jung and Karato, 2001; Ohuchi et al., 2011; Hirth and Kohlstedt, 2015). Second, no physics-based model has self-consistently explained the scaling of the steady-state dislocation density with applied stress in olivine, which is empirically distinct from the classical case in which dislocation den-

sity is proportional to the applied stress squared (Hirth and Kohlstedt, 2015). Third, there are a variety of independent geophysical observations that constrain the behaviour of Earth's upper mantle at natural strain rates (e.g., Freed et al., 2012; Pan et al., 2021) that may eventually be used as a test of predictions of our model for strain rates inaccessible in the laboratory.

3.2 Model derivation

The two essential components of our model are an equation for the evolution of dislocation density and a flow law that describes how strain rate depends on dislocation density and other variables, such as applied stress. Both are outlined here and detailed in Appendix 3.A.

Dislocation density, ρ, evolves due to dislocation storage and dislocation recovery. Dislocation storage describes the increase in ρ with increasing plastic strain as dislocation loops expand. The storage rate is $\dot{\varepsilon}/(bL)$, where $\dot{\varepsilon}$ is the strain rate, b is the magnitude of the Burgers vector, and L is a length scale that describes the average distance travelled by a dislocation before it is stored in the lattice (Estrin, 1998). We assume that L is controlled by the presence of other dislocations and grain boundaries.

Dislocation recovery describes the decrease in ρ due to dislocation annihilation. Recovery may be characterised as dynamic, whereby its rate is strain-dependent, or as static, whereby its rate is time-dependent. Our model incorporates both types of recovery; to focus on novel aspects of the model and make connections with high-temperature creep data, we only discuss static recovery here.

In static recovery, dislocations of opposite sign are driven to climb and annihilate by the interaction of their stress fields (Blum, 1971). The rate of recovery depends on the amount of suitable dislocations, their separation, and the climb velocity (Blum,

1971). Dislocation climb requires diffusion of vacancies to the climbing segment of the dislocation. Classical treatments, which assume vacancies diffuse though the lattice, suggest the recovery rate is proportional to ρ^2 (Blum, 1971). However, vacancies can also diffuse along fast diffusion pathways, like dislocation cores and grain boundaries (Spingarn et al., 1979; Spingarn and Nix, 1979). We focus on the role of these fast diffusion pathways and neglect diffusion through the bulk lattice. To account for different types of pathways, the diffusivities of each type are weighted by the volume fraction of that pathway (Hart, 1957). The volume fraction of dislocation cores (pipes) is proportional to ρ, and hence, the rate of recovery controlled by pipe diffusion is proportional to ρ^3. In contrast, the volume fraction of grain boundaries is inversely proportional to the grain size d, and thus the rate of recovery controlled by grain-boundary diffusion is proportional to ρ^2/d.

Accounting for the rates of dislocation storage and static recovery, the evolution of dislocation density is given by

$$\dot{\rho} = \underbrace{\frac{1}{b}\left(m\sqrt{\rho} + \frac{n}{d}\right)\dot{\varepsilon}}_{\text{storage}} - \underbrace{\left(\mathcal{R}_{\text{gb}}(T)\frac{\rho^2}{d} + \mathcal{R}_{\text{pipe}}(T)\rho^3\right)}_{\text{static recovery}}, \tag{3.2.1}$$

where $\dot{\varepsilon}$ is the strain rate, m and n are material constants, T is the temperature, and $\mathcal{R}_{\times}(T)$ are rate coefficients for static recovery by grain boundary or pipe diffusion. The Arrhenius temperature dependence of these rate coefficients is associated with the diffusivity of the slowest-diffusing species along the respective pathway.

Equation (3.2.1) is coupled to a flow law that describes the dependence of strain rate on dislocation density, applied stress, and temperature. Dislocations are the carriers of deformation, so the flow law depends on dislocation density and velocity (Orowan, 1934). Dislocation motion is a thermally-activated process (Krausz, 1968)

described by a stress-dependent energy barrier, which leads to the flow law

$$\dot{\varepsilon} = A(T)\rho \sinh\left(\frac{\sigma - \sigma_{\mathrm{T}} - \sigma_{\mathrm{d}}}{\sigma_{\mathrm{ref}}(T)}\right), \tag{3.2.2}$$

where $A(T)$ is a rate coefficient with an Arrhenius dependence on temperature, and σ is the applied stress. $\sigma_{\mathrm{ref}}(T)$ is the reference stress, which is related to the strength of barriers to dislocation motion and has a linear dependence on temperature (Hansen et al., 2019, 2021).

Through thermodynamic considerations, we find that that the applied stress is opposed by two microstructurally-derived stresses, σ_{T} and σ_{d}. The classical Taylor stress, $\sigma_{\mathrm{T}} = \alpha\mu b\sqrt{\rho}$, describes the cumulative effect of stress fields generated by dislocations (Taylor, 1934). Here, μ is the shear modulus and α is a constant. The second, $\sigma_{\mathrm{d}} = \beta\mu b/d$, is the threshold stress, which classically represents the minimum applied stress required for a dislocation loop to expand within a grain (Gribb and Cooper, 1998), where β is a constant.

Equations (3.2.1) and (3.2.2) constitute our model for deformation due to dislocations at high temperature. The full model, detailed in Appendix 3.A, self-consistently describes transient and steady-state deformation at both low and high temperatures and incorporates grain-size effects. Given the applied stress, temperature, and grain size, these equations can be solved for the evolution of dislocation density and strain rate, both prior to and at steady state.

3.3 Model validation and calibration

Before the model can be applied, it must be calibrated and validated by comparison with data derived from deformation experiments. To this end, we use published data from steady-state (Figures 3.1–3.3) and transient (Figure 3.4) creep experiments on olivine. At steady state, the model predicts a (nonlinear) relationship among stress,

dislocation density, and strain rate. This relationship is modulated by the grain size that, for simplicity, we treat as an independent variable, though in fact grain-size evolution may be coupled to dislocation density (e.g. Platt and Behr, 2011). We do not consider oxygen fugacity, which is known to affect strain rates (Keefner et al., 2011). Since fugacity varies among experiments, we only consider data collected at the Ni–NiO buffer. Our calibration and subsequent extrapolation to mantle conditions are not particularly sensitive to differences among activation energies of different processes; we therefore assume that all temperature-dependent processes have the same activation energy, Q.

We first test the hypothesis that pipe diffusion plays a critical role in grain-size insensitive dislocation creep in olivine. To do so, we assume grain-boundary diffusion is negligible and calibrate our model against the steady-state experimental data on large-grained (0.9 mm) aggregates from Keefner et al. (2011). This calibration constrains the rate coefficients of the flow law (Equation 3.2.2) and pipe-diffusion recovery (Equation 3.2.1), as well as the activation energy. Figure 3.1 demonstrates that the model captures the stress and temperature dependence of strain rate. To highlight the stress dependence of strain rate, we normalise the data to one temperature using our fitted activation energy in the inset of Figure 3.1. Although our model is not formally a power law, it gives an apparent power law exponent of ~ 3.5 over the range of laboratory conditions, consistent with previous empirical analysis of this dataset (Keefner et al., 2011).

Figure 3.2 compares the predicted steady-state dislocation density with published measurements for single crystals and aggregates of olivine (Kohlstedt and Goetze, 1974; Durham et al., 1977; Bai and Kohlstedt, 1992; Jung and Karato, 2001; Farla et al., 2011; Ohuchi et al., 2011). At intermediate applied stresses (30–400 MPa), the model predicts that the dislocation density approximates a power law of applied stress with an exponent of 1.4, consistent with an empirical power-law fit (Bai and

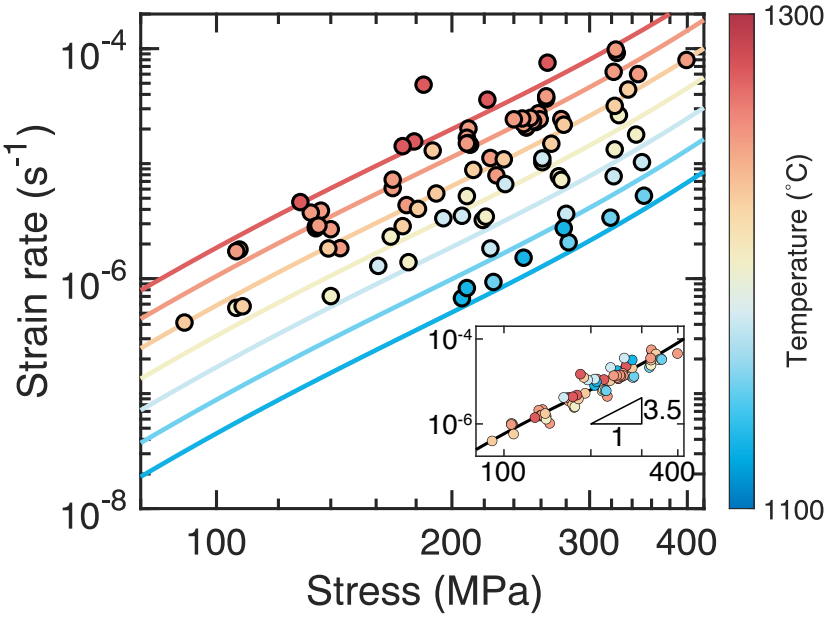

Figure 3.1: Strain rate as a function of applied stress predicted by our calibrated model, assuming that grain-size effects are negligible (solid lines). The mechanical data from Keefner et al. (2011) used in the calibration are plotted for comparison (circles) at different temperatures (indicated by colour). The inset compares model prediction at T = 1498 K with data normalised to this temperature.

Kohlstedt, 1992). However, at both small and large applied stress, the model predicts that dislocation density has a stronger dependence on applied stress, consistent with available experimental data (Figure 3.2). Aside from α, which relates the Taylor stress to the dislocation density, all parameters used to predict dislocation density are constrained by the calibration in Figure 3.1. The data in Figure 3.2 constrains α to be $2.29^{+0.14}_{-0.13}$. We note that the value of α only shifts the predicted dislocation-density curve to lower or higher dislocation density without affecting its shape.

We next calibrate the full model, including grain size effects, against experimental data from Hansen et al. (2011) and Keefner et al. (2011). The former used fine-grained ($\approx$ 10 µm) olivine aggregates. This calibration constrains the rate coefficients of the flow law (Equation 3.2.2) and both types of recovery (Equation 3.2.1), as well as the activation energy. Figure 3.3 compares the predicted grain-size dependence of strain rate against the experimental data. The experimental data are normalised to a single

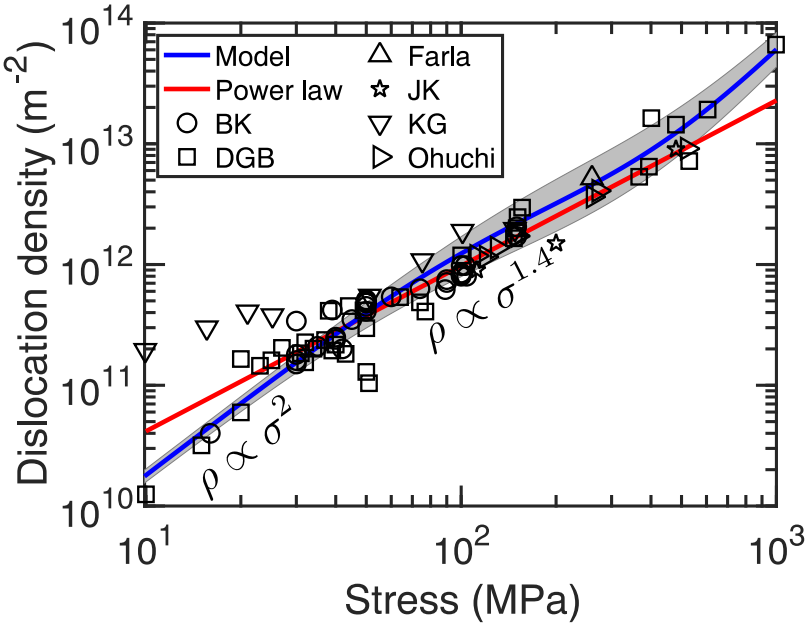

Figure 3.2: Dislocation density as a function of stress predicted by the calibrated model plotted in Figure 3.1 (blue line) compared to an empirical dislocation-density piezometer (Bai and Kohlstedt, 1992) (red line) and experimental data (black open symbols). The grey shaded area represents the 95% confidence interval from propagating the uncertainties in the underlying model parameters. Data are taken from experiments on single crystals (BK = Bai and Kohlstedt (1992), DGB = Durham et al. (1977), KG = Kohlstedt and Goetze (1974)) and aggregates (Farla = Farla et al. (2011), JK = Jung and Karato (2001), Ohuchi = Ohuchi et al. (2011)).

stress and temperature using the calibrated model. The calibrated model captures the stress, temperature, and grain-size dependencies of both datasets.

Finally, we consider the transient deformation predicted by our model. Hansen et al. (2021) performed stress-reduction experiments in which olivine single crystals are deformed at a constant applied stress until steady-state deformation is achieved, and then the applied stress is reduced to a new constant value. Transient deformation occurs after each stress step. Figure 3.4 demonstrates that our model correctly predicts the transient plastic strain. Importantly, in both the data and prediction, transients following $< 50\%$ reductions in the applied stress exhibit positive strain rates throughout (Figure 3.4A), whereas the transients following reductions of $> 50\%$ initially exhibit negative strain rates (Figure 3.4B). In our model, the negative plastic

strain rates result from the Taylor stress temporarily exceeding the (positive) applied stress, consistent with the Bauschinger effect.

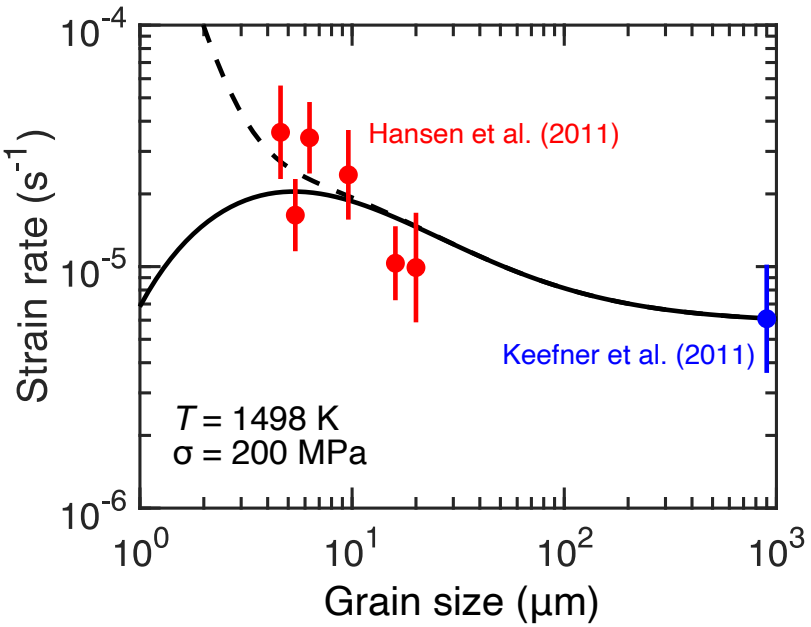

Figure 3.3: Strain rate as a function of grain size predicted by the calibrated model incorporating grain-size effects (solid line) compared to normalised mechanical data from Keefner et al. (2011) (blue) and Hansen et al. (2011) (red). The experimental data are normalised to a temperature of 1498 K and a stress of 200 MPa and then then grouped according to grain size. The circles represent the mean normalised strain rate within each group. The error bars represent one standard deviation of the normalised strain rate within each group. The strain rate predicted by combining the calibrated model with a flow law for diffusion creep (Hansen et al., 2011) is plotted as a dashed line.

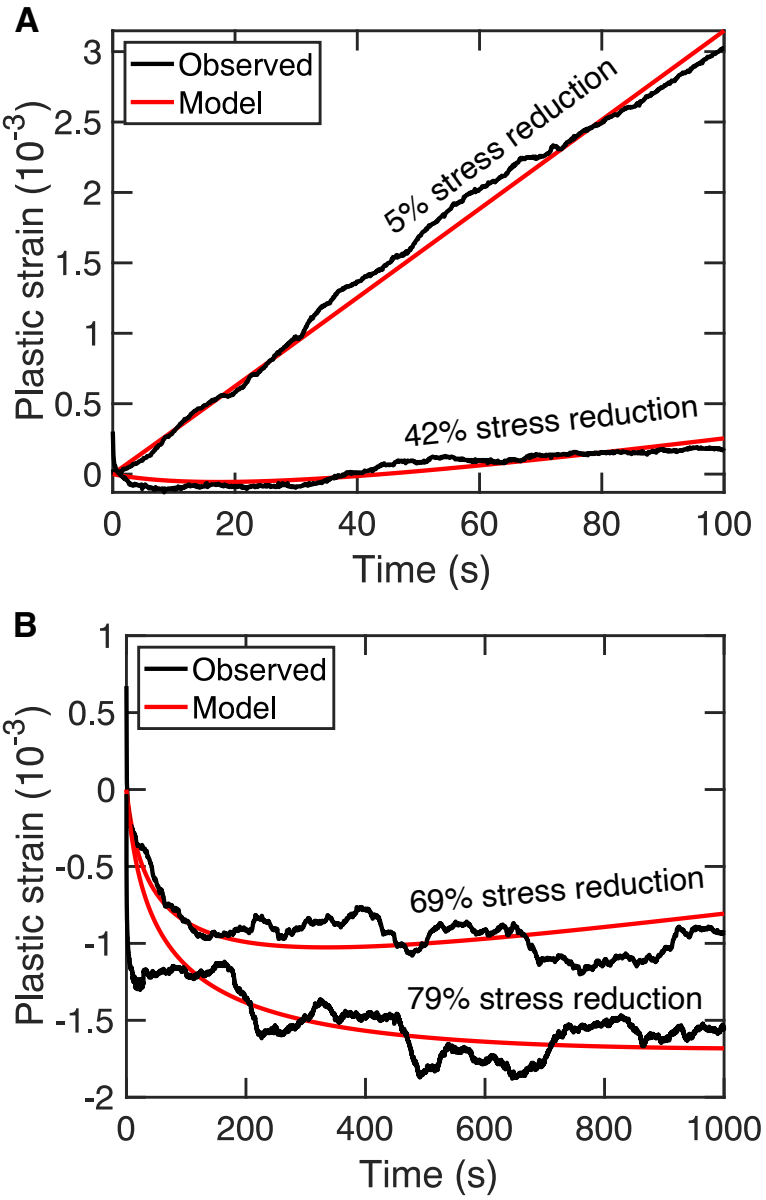

Figure 3.4: Comparison of transient deformation predicted by our model to experimental data. Plastic strain as a function of time from a stress reduction experiment (OxR0002) from Hansen et al. (2021) (black line) compared to the model prediction (red line). This experiment was performed on a single crystal compressed uniaxially in the $[101]_c$ orientation at 1523 K. The initial stress prior to reduction was 162 MPa. The curves are labelled with the percentage reduction in stress. In A, the plastic strain rate evolves over relatively short timescales (∼10 seconds), whereas in B, the plastic strain rate evolves over longer timescales (∼100 seconds).

3.4 Discussion

3.4.1 Deformation in the laboratory

Our model elucidates the microphysical relationships between dislocation density, applied stress, and strain rate that operate at laboratory conditions. The model illustrates that the steady-state dislocation density may be limited either by the Taylor stress or by recovery. In the first case, dislocation density increases until the Taylor stress approximately balances the applied stress, such that $\rho \propto \sigma^2$ and the strain rate becomes small. As a result, the dislocation storage rate becomes small and can balance the recovery rate. Alternatively, at steady state, the applied stress may significantly exceed the Taylor stress if dislocation density is limited instead by recovery. If recovery occurs mainly by pipe diffusion, the model predicts $\rho \propto \sigma^{2/3}$. The calibrated model predicts that, at laboratory conditions, both processes are significant, leading to the apparent $\rho \propto \sigma^{1.4}$ scaling observed in experimental data (Figure 3.2). This scaling previously lacked a physical explanation.

The ρ–σ scaling also influences the relationship between steady-state strain rate and applied stress. The steady-state strain rate is not linearly proportional to dislocation density as classically suggested by the Orowan equation because the Taylor stress is also dependent on the dislocation density. More fundamentally, Equation (3.2.1) demonstrates that the steady-state strain rate, $\dot{\varepsilon}_{ss}$, is controlled by the balance between dislocation storage and recovery, such that if pipe diffusion is the dominant recovery mechanism, $\dot{\varepsilon}_{ss} \propto \rho^{5/2}$. Combining this scaling for strain rate with the scaling between dislocation density and applied stress at laboratory conditions, we predict an apparent stress exponent of $(5/2) \times 1.4 = 3.5$, in agreement with experimental data on coarse-grained olivine (Figure 3.1).

Accounting for grain-boundary processes results in a model that is sensitive to

grain size, as illustrated in Figure 3.3. Grain size influences the steady-state dislocation density, and therefore strain rate, through recovery controlled by grain-boundary diffusion. Decreasing the grain size increases the rate of recovery, causing a corresponding decrease in the steady-state dislocation density and hence Taylor stress. At larger grain sizes, the strain rate is limited by the Taylor stress and hence the steady-state strain rate increases with decreasing grain size. However, at smaller grain sizes, the strain rate is instead limited by the availability of dislocations, and hence further decreasing the grain size decreases the strain rate. At constant applied stress, the dependence of the steady-state strain rate on dislocation density can be understood through Equation (3.2.2), which has a maximum as a function of dislocation density.

These grain size dependencies are consistent with available experimental data. For fine-grained samples ($\sim$10's µm) and laboratory-accessible stresses, our model predicts an inverse relationship between strain rate and grain size (Figure 3.3) and an approximate stress exponent of 3, congruent with empirical analyses (Hansen et al., 2011). These data were previously interpreted in terms of dislocation-accommodated grain-boundary sliding, in which the strain rate is limited by dislocation annihilation at grain boundaries (Langdon, 1994; Ferreira et al., 2021). This rate-limiting process is the same as the case considered here in which grain-boundary diffusion controls dislocation recovery. We note that recovery by grain-boundary diffusion has the same functional form as recovery due to grain-boundary migration, highlighting an additional link to models focused on migration as a recovery mechanism (Platt and Behr, 2011).

3.4.2 Deformation at geological strain rates

We have thus far demonstrated consistency between our model and experiments. We now examine predictions of our model beyond laboratory conditions. In particular, we consider applied stresses far smaller than those normally accessed in the laboratory

but typical within Earth's mantle. Figure 3.5 explores the predicted dependence of strain rate on applied stress for a range of grain sizes. In the limit of infinite grain size, for which grain-boundary diffusion does not contribute to recovery, we predict a transition in stress exponent from 3.5 at typical laboratory stresses to 5 at smaller applied stresses. The transition in stress exponent results from a transition in the ρ–σ relationship. As noted above, at small applied stresses, we predict $\rho \propto \sigma^2$ due to the reduced recovery rates associated with pipe diffusion, such that the Taylor stress approximately balances the applied stress (Figure 3.2). Therefore, the apparent stress exponent is given by $(5/2) \times 2 = 5$. A higher stress exponent is consistent with the limited laboratory data available for single crystals of olivine at low stresses ($\sim$ 30 MPa), for which the stress exponent across experiments varied between 3 and 5 (Bai et al., 1991).

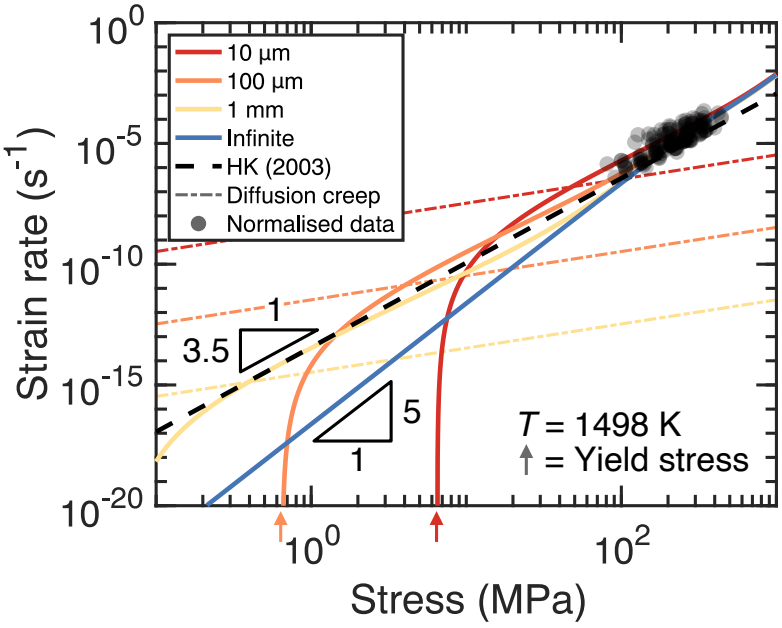

(*Caption overleaf.*)

Figure 3.5 *(previous page)*: Strain rate as a function of stress at a temperature of 1498 K. Curves are constructed from the calibrated model incorporating grain-size effects using grain sizes of 10 µm, 100 µm, and 1 mm, and from the calibrated model that neglects grain-size effects (infinite). Experimental data (black circles) from Keefner et al. (2011) and Hansen et al. (2011) are normalised to the same temperature using the fitted activation energy. Plotted for comparison are the dislocation creep flow law (black dashed) from Hirth and Kohlstedt (2003), and the diffusion creep flow law (coloured dot-dashed) from Hansen et al. (2011). The yield stresses for dislocation deformation are indicated by arrows below the stress axis.

At finite grain size, the predicted steady-state strain rate curves in Figure 3.5 have a complex relationship with the applied stress and grain size. Our model at steady-state can be simplified by assuming the applied stress balances the sum of the Taylor and threshold stresses, which approximately holds in Figure 3.5. Combining this balance with Equation (3.2.1) and (3.2.2) yields $\dot{\varepsilon}_{\mathrm{ss}} \propto (\sigma - \sigma_{\mathrm{d}})^4(\sigma_{\mathrm{d}}/\sigma)$. This approximate flow law has two limits. In the limit that $\sigma \gg \sigma_{\mathrm{d}}$, we recover an apparent stress exponent of 3 and a grain size exponent of 1, consistent with observations in the laboratory (Hansen et al., 2011). In the limit that $\sigma \to \sigma_{\mathrm{d}}$, $\dot{\varepsilon} \to 0$ such that the threshold stress σ_{D} acts as a yield stress that is inversely proportional to the grain size, which is consistent with recent evaluations of the Hall-Petch effect (Dunstan and Bushby, 2014).

The predicted scalings in Figure 3.5 illustrate an important point. The measured power-law exponents describing relationships between steady-state strain rates, applied stresses, grain size, and dislocation density are not necessarily intrinsic properties of deformation mechanisms in a given material. Instead, empirical exponents reflect the underlying balance in microphysical processes at laboratory conditions. Therefore, exponents measured in the laboratory do not necessarily apply outside of these conditions, even though the same set of microphysical processes operate. Consequently, power laws fitted at laboratory conditions should only be extrapolated with extreme care. Furthermore, although we have only considered the effect of grain

size and applied stress, the same considerations also apply to other state variables such as oxygen fugacity, water fugacity, and silica activity.

Figure 3.6 is a deformation-mechanism map exploring strain rate as a function of applied stress and grain size. We compare predicted strain rates to those derived from previous flow laws for dislocation creep (Hirth and Kohlstedt, 2003) and grain-size sensitive dislocation creep (Hansen et al., 2011). At typical laboratory strain rates ($\geq 10^{-5}\,\mathrm{s}^{-1}$), the predictions of our calibrated model are in agreement with the previous flow laws. However, at mantle stresses ($\sim$ 1 MPa) and grain sizes ($\sim$3 mm) (Hirth and Kohlstedt, 2015), the predicted strain rates are approximately an order of magnitude smaller than previous flow laws for dislocation deformation (Hirth and Kohlstedt, 2003; Hansen et al., 2011). The difference in the predicted strength of the mantle reflects the changes in the scalings of strain rate with applied stress and grain size predicted by our model outside of laboratory conditions. Indeed, our model predicts that deformation has a range of grain-size sensitivities, including both weakening and strengthening with decreasing grain size. Despite these differences, we find that our model at $d = 1$ mm and mantle stresses makes similar predictions to the Hirth and Kohlstedt (2003) dislocation creep flow law (Figure 3.5). This correspondence may explain the successful application of this dislocation creep flow law to geophysical models (e.g., Freed and Bürgmann, 2004). Finally, a significant region of the deformation mechanism map corresponds to no deformation at all by dislocation mechanisms, as stresses are lower than the threshold stress. Our model therefore predicts that other mantle deformation mechanisms, such as diffusion creep, will likely be more important to steady-state deformation than previously assumed. The predictions of the diffusion creep flow law from Hansen et al. (2011) are compared to our model in Figure 3.5. The higher strain rates at low applied stress associated with high-temperature diffusion creep would obscure the yielding behaviour predicted by our model.

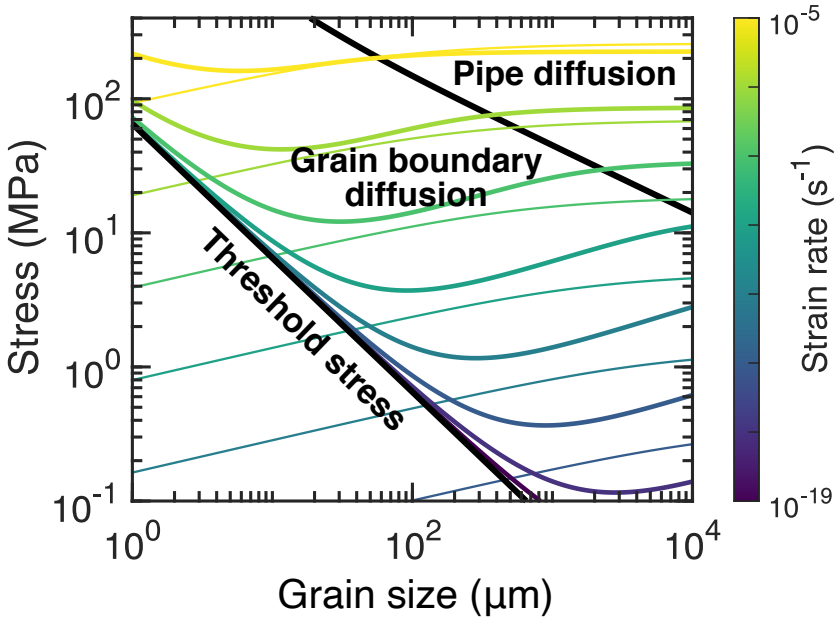

Figure 3.6: Deformation mechanism map of dislocation-accommodated deformation. The map is constructed as a function of grain size and stress at a temperature of 1498 K. Contours represent constant strain rate. Thick contours represent the strain rate predicted by our model and the thin contours are calculated using a combination of the dislocation creep flow law from Hirth and Kohlstedt (2003) and the grain-size sensitive dislocation creep flow law from Hansen et al. (2011). The colours of the contours indicate the strain rate. The threshold stress and the boundary between the different dominant recovery mechanisms (pipe diffusion and grain boundary diffusion) are plotted as thick black lines.

3.4.3 Transient deformation at geological conditions

Next, we consider the predictions of our model for time-dependent mantle deformation. Figure 3.7 explores how an abrupt change in applied stress affects deformation at mantle conditions. We assume an initially uniform differential stress of 1 MPa, for which the steady-state viscosity at the base of the lithosphere is $\approx 10^{20}$ Pa s. We then instantaneously increase the applied stress by 10%. Although both the old and new steady-state viscosities are similar, the transient viscosities differ significantly from the steady state. Instantaneously, the viscosity drops by approximately two orders of magnitude (to $\approx 10^{18}$ Pa s at the base of the lithosphere) and evolves over a timescale of months to years. The magnitude of the reduction in viscosity and the evolution

timescale are consistent with geophysical observations of processes associated with abrupt stress changes, such as post-seismic creep (Freed and Bürgmann, 2004; Freed et al., 2006, 2012) and glacial-isostatic adjustment (Pan et al., 2021). The ratio of the instantaneous to steady-state viscosity is approximately independent of depth. However, the rate of evolution towards steady state is depth dependent. Depths with smaller absolute transient viscosities, and therefore larger strain rates, evolve more quickly, indicating that dislocation storage controls the transient evolution of viscosity at mantle conditions. Thus, whilst steady-state deformation at mantle stresses is controlled by the recovery coefficients $\mathcal{R}_{\times}(T)$, transient deformation is sensitive to the flow law coefficient $A(T)$.

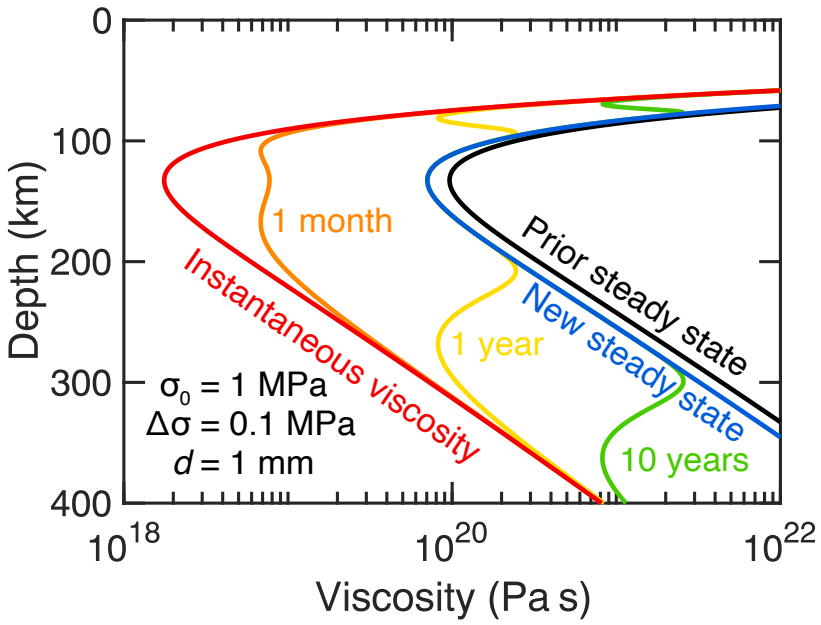

Figure 3.7: Viscosity as a function of depth predicted by our model assuming a mantle grain size of 1 mm. The initial steady-state viscosity under a uniform stress of 1 MPa is plotted as a black line. The coloured lines indicate the viscosity following a 0.1 MPa increase in stress for a variety of times (red = instantaneous, orange = 1 month following, yellow = 1 year following, green=10 years following, blue = new steady state). The temperature as a function of depth is calculated assuming a half-space cooling model and an adiabatic geotherm for a 50 million-year-old lithosphere with a potential temperature of 1350°C (pp. 185–187 Turcotte and Schubert, 2002). The activation volume is assumed to be 15 cm^3/mol (Dixon and Durham, 2018).

Transient, dislocation-accommodated deformation in Earth is commonly modelled using a nonlinear Burgers model, in which transient and steady-state viscosities possess the same sensitivity to the applied stress (Hansen et al. (2021), and references therein). However, our results indicate that transient and steady-state viscosities have a fundamentally different dependence on the applied stress. Moreover, our results demonstrate that transient and steady-state viscosities at mantle conditions are likely controlled by separate components of the dislocation microphysics. The evolution of other aspects of microstructure that we do not account for, such as grain size and crystallographic texture, will also influence the transient viscosity, but that evolution requires much larger strains than investigated here (Hansen et al., 2012). Therefore, we suggest the evolution of dislocation density is the most relevant process for predicting transient viscosity during stress changes that occur on human timescales, such as post-seismic creep and glacial-isostatic adjustment.

3.4.4 Broader implications

Although we have calibrated our model for olivine deformation, our formulation is applicable to a broad array of materials. Whilst the predicted transitions in stress exponent have not been directly observed in olivine, such transitions have been observed in solid-solution alloys (Yavari and Langdon, 1982), some of which have already been found to be good analogs for olivine (Cooper et al., 2016). For example, in experiments on an Al–Mg alloy, the apparent stress exponent decreases from 5 to 3 for applied stresses above 7 MPa (Oikawa et al., 1978). This transition in stress exponent is correlated with a change in the scaling of an empirically-observed back stress opposing deformation, which we take to be the Taylor stress in our model. At the smallest stresses, for which the stress exponent is 5, the back stress is observed to be approximately equal to the applied stress, whereas at higher stresses, the back stress is a fraction of the applied stress (Oikawa et al., 1978). These observations are in

agreement with the predictions of our model for olivine. We believe that this agreement underlines the importance of constructing microphysical models of deformation to make physics-based predictions at conditions far from the laboratory.

The calibrated model that we have presented provides a quantitative description of dislocation creep, grain-size-sensitive dislocation creep, and the Hall-Petch effect in olivine. The model is in agreement with observations of transient strain obtained from stress-reduction tests and is in broad agreement with estimated transient viscosities associated with post-seismic creep and post-glacial rebound. Our model is easily extended to incorporate dynamic recovery, the dominant dislocation annihilation process at low temperatures. Indeed, our formulation of this process, is consistent with that used by Hansen et al. (2019) to model strain hardening and the Bauschinger effect at low temperatures. As a result, our model also extends to deformation by low-temperature plasticity. An effect not captured by this work is the viscous anisotropy of single crystals of olivine. Future work will attempt to model this anisotropy by considering the anisotropic rates of recovery.

Appendix

3.A Derivation of model

Our theoretical framework comprises of a model for the evolution of dislocation density and a flow law that relates strain rate to dislocation density and applied stress. We consider each of these below, in turn. Although stress and strain rate are, in general, tensor quantities, we treat both as scalars; we are not considering the effects of anisotropy and use data from uniaxial deformation experiments. Furthermore, we make the simplifying assumption that dislocation density may be treated single, scalar variable. Consequently we do not distinguish between the densities of dislocations associated with individual slip systems or categories of dislocations such as geometrically-necessary, statistically-stored, mobile and immobile. We do not model grain-size evolution, rather we treat grain size as a model parameter.

3.A.1 Dislocation density evolution

Our model of dislocation-density evolution quantifies several processes that affect the density of dislocations. These include terms that act to increase dislocation density (storage) and those that decrease dislocation density (dislocation annihilation through dynamic and static recovery). We assume that each process operates independently

of the others and hence that the total rate of change of dislocation density is the linear combination of the separate rates,

$$\dot{\rho}_{\text{total}} = \dot{\rho}_{\text{storage}} - \dot{\rho}_{\text{dynamic}} - \dot{\rho}_{\text{static}}. \tag{3.A.1}$$

The rates of dislocation storage and dynamic recovery are modelled according to the Mecking and Kocks model (Mecking and Kocks, 1981). We complement this approach with the rate of static recovery, with an emphasis on the role of fast diffusion pathways.

We model increases in dislocation density by dislocation storage, a process first described by Kocks (Kocks, 1966, 1976; Mecking and Kocks, 1981; Estrin and Mecking, 1984; Estrin, 1998). Consequently, we do not model the operation of dislocation sources. Dislocation storage accounts for a geometrical property of dislocation glide; as dislocations glide, their total line length increases (Kocks, 1966). There is a corresponding increase in dislocation density because dislocation density is the total dislocation line length per unit volume. In contrast, the strain produced by dislocation motion is proportional to the area swept by the dislocation. Consequently, the rate of change of dislocation density with strain is inversely proportional to the lateral extent of the dislocation loops. An illustrative example is given by an expanding circular dislocation loop (Blum and Eisenlohr, 2009). The strain associated with the loop is proportional to the area swept by the loop as it expands (πr^2), whereas the dislocation density is proportional to the perimeter of the loop ($2\pi r$). As a result, $\Delta\rho/\Delta\varepsilon \propto 2/r$.

Dislocation storage is parameterised statistically, using the dislocation mean free path Λ, the distance travelled by a gliding dislocation before it is obstructed and ceases motion (Kocks, 1976; Mecking and Kocks, 1981; Estrin and Mecking, 1984; Estrin, 1998). The rate of dislocation storage is

$$\dot{\rho}_{\text{storage}} = \frac{1}{b\Lambda}\dot{\varepsilon}, \tag{3.A.2}$$

where b is the magnitude of the Burgers vector (Kocks, 1976; Mecking and Kocks, 1981; Estrin and Mecking, 1984; Estrin, 1998). There are several microstructural features that obstruct dislocation motion and thus control the mean free path (Estrin and Mecking, 1984; Estrin, 1998). Here we consider two such obstacles: grain boundaries and other dislocations. If grain boundaries act to impede dislocation motion, then $\Lambda \propto d$, where d is the grain size. If other dislocations act as obstacles, the mean free path is related to the dislocation density. Whether dislocations are either randomly distributed or organised into structures such as subgrains, the obstacle spacing is inversely proportional to the square root of dislocation density and hence $\Lambda \propto \rho^{-1/2}$. The effective mean free path should reflect the smallest of these microstructural length scales. Consequently, we follow Estrin (1998) and calculate Λ using a harmonic mean

$$\frac{1}{\Lambda} = m\sqrt{\rho} + n\frac{1}{d}, \tag{3.A.3}$$

where m and n are material constants.

We now consider the annihilation processes of dynamic and static recovery. Dynamic recovery is the annihilation of dislocations associated with dislocation glide (Kocks, 1976). During glide, a dislocation may pass near a dislocation of opposite sign, with which it can annihilate. Dynamic recovery is included as in the Kocks-Mecking-Estrin (KME) model (Kocks, 1976; Mecking and Kocks, 1981; Estrin and Mecking, 1984; Estrin, 1998). Its parameterisation may be interpreted according to the framework of Essmann and Mughrabi (1979), who assume that annihilation occurs when dislocations of opposite sign come within a critical distance y_c of each other. By modelling the probability that a moving dislocation will encounter a dislocation of opposite sign, the dynamic recovery rate can be calculated as

$$\dot{\rho}_{\text{dynamic}} = -\omega\rho|\dot{\varepsilon}| \tag{3.A.4}$$

where ω is a constant equal to $2y_c/b$ (Nes et al., 2002).

The KME model considers only storage and dynamic recovery. We extend this model with a parameterisation of static recovery, following the approach of Sandström and Hallgren (2012). However, in contrast to their approach, we emphasise the role of fast diffusion pathways. Static recovery is the time-dependent, endogenous process of dislocation annihilation. In this process, dislocation dipoles comprising dislocations of opposite sign are driven to climb and annihilate by the mutual attraction of their stress fields (Nix et al., 1985). Classically, static recovery follows second order kinetics (i.e. $\dot{\rho} \propto \rho^2$). Friedel (pp. 239, 1964) originally derived second order kinetics from detailed consideration of the spacing of a Frank network of dislocations. Blum (1971) applied a more heuristic argument to derive the same kinetics. The rate of static recovery should scale with dislocation density divided by the timescale of an annihilation event. Blum showed that this timescale, which depends on the dislocation spacing and climb velocity, is inversely proportional to the dislocation density, such that static recovery follows second order kinetics. Dislocation climb is accommodated by the diffusion of vacancies to the dislocation core and the climb velocity is proportional to the vacancy diffusivity. Therefore, the rate of static recovery is proportional to

$$\dot{\rho}_{\text{static}} \propto -D(T)\rho^2, \tag{3.A.5}$$

where $D(T)$ is the vacancy diffusivity, which we assume to have an Arrhenius dependence on temperature (e.g., Nix et al., 1985).

While previous models typically assume that vacancies predominantly diffuse through the lattice, the relatively open structures of crystal defects such as dislocation cores and grain boundaries provide faster diffusion pathways. We refer to diffusion along these pathways as pipe diffusion and grain-boundary diffusion, respectively (Spingarn et al., 1979; Spingarn and Nix, 1979). In olivine, dislocation

structures are known to be anisotropic (Bai and Kohlstedt, 1992), which may result in an anisotropic diffusivity of crystal vacancies.

The simplest model of diffusivity that accounts for high-diffusivity pathways was proposed by Hart (1957). Hart hypothesised that the effective diffusivity, accounting for both diffusion through the lattice and pipe diffusion, can be estimated as an average of the respective diffusivities of these pathways, weighted by volume fractions of the lattice ($f_{\text{lattice}} \approx 1$) and the dislocation cores ($f_{\text{pipe}} \approx \pi b^2 \rho$). Spingarn et al. (1979) performed a more detailed theoretical analysis confirming that Hart's is the relevant average for dislocation climb. Similarly, enhanced vacancy diffusivity in the vicinity of grain boundaries, due to grain-boundary diffusion, is assumed to increase the rate of dislocation climb (Spingarn and Nix, 1979). We include grain-boundary diffusion in our calculation of the effective diffusivity by assuming that the volume fraction of grain boundaries is $f_{\text{gb}} \approx 3\delta/d$, where δ is the grain boundary thickness. Increased rates of dislocation climb result in increased rates of static recovery. Consequently, accounting for the role and volume fraction of different diffusion pathways, we suggest the rate of static recovery is given by

$$\dot{\rho}_{\text{static}} = -\mathcal{R}_{\text{lattice}}(T)\rho^2 - \mathcal{R}_{\text{pipe}}(T)\rho^3 - \mathcal{R}_{\text{gb}}(T)\rho^2 \frac{1}{d}, \tag{3.A.6}$$

where $\mathcal{R}_{\times}(T)$ are rate coefficients with an Arrhenius dependence on temperature as

$$\mathcal{R}_{\times}(T) = \mathcal{R}^*_{\times} \exp\left(-\frac{Q_{\times}}{\mathrm{R}T}\right), \tag{3.A.7}$$

where R is the ideal gas constant. The activation energy, $Q_{\times}$, associated with each of these recovery mechanisms should reflect the underlying activation energy of the respective diffusion process.

Combining the terms for dislocation storage and recovery, our model is given by

$$\dot{\rho} = \underbrace{\frac{1}{b}\left(m\sqrt{\rho} + \frac{n}{d}\right)\dot{\varepsilon}}_{\text{storage}} - \underbrace{\omega\rho|\dot{\varepsilon}|}_{\substack{\text{dynamic} \\ \text{recovery}}} - \underbrace{\left(\mathcal{R}_{\text{lattice}}(T)\rho^2 + \mathcal{R}_{\text{pipe}}(T)\rho^3 + \mathcal{R}_{\text{gb}}(T)\rho^2\frac{1}{d}\right)}_{\text{static recovery}}. \tag{3.A.8}$$

3.A.2 Flow law

The flow law relates the strain rate due to dislocation motion to the applied stress. The strain rate depends on the density of moving dislocations and their velocity, expressed by the Orowan equation (Orowan, 1934),

$$\dot{\varepsilon} = \rho_m b v, \tag{3.A.9}$$

where ρ_m is the density of mobile dislocations and v is the dislocation velocity. In the present theory, we do not distinguish between mobile and immobile dislocations. Instead, we make the simplifying assumption that the mobile dislocation density ρ_m is approximated by the total dislocation density ρ.

To derive an expression for the dislocation velocity, we follow the approach of Hansen et al. (2019) and Hansen et al. (2021). Dislocation motion involves the rearrangement of atomic bonds in a thermally activated process (Krausz, 1968). Consequently, the rate of motion is proportional to a Boltzmann factor $\exp(-\Delta G/RT)$ with an activation energy $\Delta G(\sigma_{\text{eff}})$ that represents the energy barrier to be overcome for dislocation motion. In the presence of an effective stress σ_{eff}, the activation energy is reduced for motion of dislocations in the direction of the effective stress and increased for motion in the opposite direction (Krausz, 1968). The directional stress dependence of the activation energy biases the motion of dislocations to be in the direction of the effective stress. We make the simplifying assumptions that the activation energy is linearly dependent on the effective stress, and that this linear dependence is equal

and opposite in the forwards and reverse directions. The net velocity is proportional to the difference between the rates of forward and reverse motion. Consequently, the net velocity, as the difference between two exponential functions whose arguments have opposite sign, is proportional to the sinh of the effective stress (Krausz, 1968; Wu and Krausz, 1994). The consideration of forward and reverse rates of motion led Hansen et al. (2019) to obtain

$$v \propto \exp\left(-\frac{Q}{\mathrm{R}T}\right) \sinh\left(\frac{Q}{\mathrm{R}T}\frac{\sigma_{\mathrm{eff}}}{\sigma_{\mathrm{P}}}\right), \tag{3.A.10}$$

where Q is the activation energy in the absence of an effective stress, T is the temperature, σ_{eff} is the effective stress, and σ_{P} is the strength of local barriers to dislocation motion. The assumption that the activation energy has a linear dependence on the effective stress is consistent with a model in which the local barrier to dislocation motion is lattice friction, as discussed by Hansen et al. (2021). In this interpretation, σ_{P} is the Peierls stress. Substituting Equation (3.A.10) for dislocation velocity into Equation (3.A.9), the strain rate is given by

$$\dot{\varepsilon} = A(T)\rho \sinh\left(\frac{\sigma_{\mathrm{eff}}}{\sigma_{\mathrm{ref}}(T)}\right), \tag{3.A.11}$$

where $A(T)$ is a pre-factor with an Arrhenius dependence on temperature

$$A(T) = A^* \exp\left(-\frac{Q}{\mathrm{R}T}\right), \tag{3.A.12}$$

and A^* is a pre-exponential constant. $\sigma_{\mathrm{ref}}(T)$ is a temperature dependent reference stress that is given by

$$\sigma_{\mathrm{ref}}(T) = \sigma_{\mathrm{P}}\frac{\mathrm{R}T}{Q}. \tag{3.A.13}$$

To make Equation (3.A.11) useful in combination with the evolution of dislocation density of Equation (3.A.8), we need to relate the effective stress to the applied stress.

3.A.3 The applied stress and the effective stress

The effective stress is a combination of the applied stress and internal stresses arising from the presence of dislocations and grain boundaries. To understand how these stresses contribute to the effective stress, we analyse our model in terms of non-equilibrium thermodynamics (Jou et al., 1996; Lebon et al., 2008). In this context, the second law of thermodynamics takes the form of the entropy inequality, which states that the rate of internal entropy production must be positive (Müller, 1967; Coleman and Noll, 1974). A process is thermodynamically admissible if it is compatible with the entropy inequality (Coleman and Noll, 1974). We limit consideration to the internal entropy production rate associated with deformation, neglecting any potential coupling to other material processes (e.g., grain-size evolution). Consequently, the entropy inequality associated with our model is

$$\dot{\Sigma}^D = \frac{\sigma\dot{\varepsilon} - \gamma\dot{\rho}}{T} \geq 0, \tag{3.A.14}$$

where $\dot{\Sigma}^D$ is the internal entropy production rate associated with deformation. The energy per unit length of dislocation, γ, arises from the elastic strain of the lattice surrounding a dislocation and hence,

$$\gamma = c\mu b^2, \tag{3.A.15}$$

where c is a constant of order unity and μ is the elastic shear modulus (Hirth and Lothe, 1982, pp. 179–180). Substituting our model for $\dot{\rho}$ (Equation 3.A.8) into (3.A.14) and multiplying by T, the entropy inequality becomes

$$\left[\sigma - c\mu b\left(m\sqrt{\rho} - \frac{n}{d}\right)\right]\dot{\varepsilon} + \omega c\mu b^2\rho|\dot{\varepsilon}| + c\mu b^2\mathcal{R}_{\text{lattice}}(T)\rho^2 + c\mu b^2\mathcal{R}_{\text{pipe}}(T)\rho^3 + c\mu b^2\mathcal{R}_{\text{gb}}(T)\rho^2\frac{1}{d} \geq 0. \tag{3.A.16}$$

In (3.A.16), recovery terms are always associated with a positive source of entropy because they act to reduce the stored strain energy. Consequently, recovery is always compatible with the entropy inequality. In contrast, the first term is not necessarily associated with a positive entropy source. The entropy inequality, however, must hold for arbitrarily imposed deformations and dislocation densities, and so the strain rate dependent term must also be positive

$$\left[\sigma - c\mu b\left(m\sqrt{\rho} - \frac{n}{d}\right)\right]\dot{\varepsilon} \geq 0. \tag{3.A.17}$$

Substituting our derived flow law (3.A.11) for $\dot{\varepsilon}$, we find that

$$A(T)\rho\left[\sigma - c\mu b\left(m\sqrt{\rho} - \frac{n}{d}\right)\right]\sinh\left(\frac{\sigma_{\text{eff}}}{\sigma_{\text{ref}}(T)}\right) \geq 0. \tag{3.A.18}$$

Since $A(T)\rho$ is positive and sinh is an odd function of the effective stress, this inequality is satisfied if

$$\sigma_{\text{eff}} = \sigma - c\mu b\left(m\sqrt{\rho} - \frac{n}{d}\right), \tag{3.A.19}$$

thus defining the relationship between the applied stress σ and the effective stress. We identify the second and third terms of this equation as the back stress σ_{b}, such that $\sigma_{\text{eff}} = \sigma - \sigma_{\text{b}}$. Back stress is the macroscopic quantity that summarises the cumulative effect of the internal stresses produced by elements of the microstructure. The back stress is

$$\sigma_{\text{b}} = \alpha\mu b\sqrt{\rho} + \beta\mu b\frac{1}{d}, \tag{3.A.20}$$

where $\alpha = cm$ and $\beta = cn$ are constants. The first term takes the form of the classical Taylor equation (Taylor, 1934), which summarises the cumulative effect of stresses due to dislocation interactions. We therefore define this term to be the Taylor stress σ_{T},

$$\sigma_{\text{T}} = \alpha\mu b\sqrt{\rho}. \tag{3.A.21}$$

The second term also takes a classical form, representing the stress within a grain of size d that must be exceeded by the applied stress for a dislocation loop to expand (Gribb and Cooper, 1998). We therefore define this term to be the threshold stress σ_{d},

$$\sigma_{\mathrm{d}} = \beta\mu b/d, \tag{3.A.22}$$

and assume that $|\sigma| > \sigma_{\mathrm{d}}$ for dislocation-accommodated deformation to operate.

Using equation (3.A.20), the complete model is therefore given by

$$\dot{\rho} = \frac{1}{b}\left(m\sqrt{\rho} + \frac{n}{d}\right)\dot{\varepsilon} - \omega\rho|\dot{\varepsilon}| - \mathcal{R}_{\mathrm{lattice}}(T)\rho^2 - \mathcal{R}_{\mathrm{pipe}}(T)\rho^3 - \mathcal{R}_{\mathrm{gb}}(T)\rho^2\frac{1}{d}, \tag{3.A.23}$$

$$\dot{\varepsilon} = A(T)\rho\sinh\left[\frac{\sigma - \sigma_{\mathrm{b}}}{\sigma_{\mathrm{ref}}(T)}\right]. \tag{3.A.24}$$

Once material parameters and grain size are specified, this system of two equations can be solved for the evolution of dislocation density and strain, given the applied stress.

3.B Restatement of model in terms of Taylor stress

The model derived above determines the strain and dislocation-density rates in terms of the dislocation density, applied stress, and the back stress (the latter comprising the threshold and Taylor stresses). However, the dislocation density and the Taylor stress are related by the Taylor equation (Equation 3.A.21), and so one variable may be eliminated in favour of the other. Because the back stress may be inferred from measurements in a mechanical experiment, we eliminate the dislocation-density term in favour of the components of back stress (Taylor and threshold stress). This

approach leads to

$$\dot{\sigma}_{\mathrm{T}} = M\left(\frac{\sigma_{\mathrm{T}}+\sigma_{\mathrm{d}}}{\sigma_{\mathrm{T}}}\dot{\varepsilon} - \frac{\sigma_{\mathrm{T}}}{\sigma_{\mathrm{T,\,max}}}|\dot{\varepsilon}| - \mathcal{R}'_{\mathrm{lattice}}(T)\sigma_{\mathrm{T}}^3 - \mathcal{R}'_{\mathrm{pipe}}(T)\sigma_{\mathrm{T}}^5 - \mathcal{R}'_{\mathrm{gb}}(T)\sigma_{\mathrm{T}}^3\sigma_{\mathrm{d}}\right), \tag{3.B.1}$$

$$\dot{\varepsilon} = A'(T)\sigma_{\mathrm{T}}^2 \sinh\left(\frac{\sigma-\sigma_{\mathrm{T}}-\sigma_{\mathrm{d}}}{\sigma_{\mathrm{ref}}(T)}\right), \tag{3.B.2}$$

where $M = cm^2\mu/2$ is a modulus associated with the evolution of Taylor stress and primes denote temperature-dependent factors whose pre-exponential factors have been redefined to absorb constants. We have introduced $\sigma_{\mathrm{T,\,max}}$, which, in the absence of a threshold stress represents an upper bound on the Taylor stress due to dynamic recovery. Dislocation storage and dynamic recovery, when framed in terms of the Taylor stress, take a similar form to the back stress model considered by Hansen et al. (2019). Consequently, we can estimate some model parameters using the fitted constants from that previous study: the modulus M to be 135^{+55}_{-47} GPa and $\sigma_{\mathrm{T,\,max}}$ to be 1.8 ± 0.2 GPa.

3.C Assumptions and simplifications

The full model of Equations (3.B.1) and (3.B.2) is applicable at low temperature, for which dynamic recovery is more important, and high temperature, for which static recovery is dominant. Our interest in the present work is high-temperature deformation, hence we neglect the dynamic recovery term. Furthermore, we neglect recovery by lattice diffusion because it gives rise to a stress–strain-rate exponent of 3 and a stress–dislocation-density exponent of 2. Both of these exponents are inconsistent with laboratory measurements of olivine deformation (Hirth and Kohlstedt, 2015).

Moreover, since the focus of the present work is on understanding the consequences of dislocation-density evolution, we neglect temporal variations in mean grain size.

These variations could be written in terms of an equation for $\dot{d}$, which would be coupled to Equations (3.B.1) and (3.B.2) through the threshold stress σ_D. We defer this consideration to future work and simplify Equation (3.B.1) to

$$\dot{\sigma}_{\mathrm{T}} = M\left(\frac{\sigma_{\mathrm{T}}+\sigma_{\mathrm{d}}}{\sigma_{\mathrm{T}}}\dot{\varepsilon} - \mathcal{R}'_{\mathrm{pipe}}(T)\sigma_{\mathrm{T}}^{5} - \mathcal{R}'_{\mathrm{gb}}(T)\sigma_{\mathrm{T}}^{3}\sigma_{\mathrm{d}}\right). \tag{3.C.1}$$

Solutions to this reduced equation are analysed in the main text.

3.D The limit of large grain size

In the limit $\sigma_D \ll \sigma_T$ corresponding to large grain size (or the mechanical context of a single crystal), dislocation storage controlled by grain size and recovery controlled by grain-boundary diffusion are both negligible. Dropping these contributions from Equations (3.B.2) and (3.C.1) leads to the grain-size-independent model

$$\dot{\sigma}_{\mathrm{T}} = M\left[\dot{\varepsilon} - \mathcal{R}'_{\mathrm{pipe}}(T)\sigma_{\mathrm{T}}^{5}\right], \tag{3.D.1}$$

$$\dot{\varepsilon} = A'(T)\sigma_{\mathrm{T}}^{2}\sinh\left(\frac{\sigma-\sigma_{\mathrm{T}}}{\sigma_{\mathrm{ref}}(T)}\right). \tag{3.D.2}$$

In the main text we demonstrate that this model can explain canonical observations of dislocation creep in deformation of single crystals and polycrystalline samples with large grain size. It provides a good fit to the observed, steady-state stress–strain-rate relationship (Figure 3.1), stress–dislocation-density relationship (Figure 3.2) for olivine, as well as the evolution of strain rate under transient creep (Figure 3.4).

3.E Determination of the Taylor constant

In the calibrated model, we eliminate dislocation density in favour of the Taylor stress. We can calculate the predicted steady-state Taylor stress at a given applied

stress using Equations (3.D.1) and (3.D.2). The dislocation density may then be calculated by rearranging the Taylor equation to yield

$$\rho = \left(\frac{\sigma_{\mathrm{T}}(\sigma)}{\alpha \mu b} \right)^2 . \tag{3.E.1}$$

However, α is an unknown constant that is not constrained during the model calibration with mechanical data. Instead, we calibrate α using observations of dislocation density at different applied stresses. Errors in the measurement of dislocation density are proportional to the dislocation density (Farla et al., 2011), and so we regress against the logarithm of dislocation density. As a result, we rearrange Equation (3.E.1) to give

$$\log(\rho^i \mu b^2 / \sigma_{\mathrm{T}}(\sigma^i)) = -2\log(\alpha) + \epsilon^i, \tag{3.E.2}$$

where ϵ are observational errors that are assumed to be random, uncorrelated with zero mean, and the superscript i refers to the i^{th} observation, $i = 1 \ldots N$. The only unknown in Equation (3.E.2) is intercept $-2\log(\alpha)$ and so Equation (3.E.2) is an intercept-only model. The least squares estimate of $-2\log(\alpha)$ is therefore given by

$$-2\log(\alpha) = \frac{1}{N} \sum_{i=1}^{N} \log \left[\rho^i \mu b^2 / \sigma_{\mathrm{T}}(\sigma^i) \right] . \tag{3.E.3}$$

Using this approach, we calibrate α to be $2.29^{+0.14}_{-0.13}$. Importantly, the shape of the predicted dislocation-density–applied stress curve does not depend on the value of α. The calibrated value of α only has the effect of scaling the predicted dislocation-density by a constant value.

3.F Transient creep solutions

We compare the predicted transient plastic strain following stress reductions to observations from Hansen et al. (2021) in Figure 3.4. The experiments that we compare against were performed on single crystals. We therefore apply our model in the limit of infinite grain size. The single crystal used in the experiments plotted in Figure 3.4 was orientated in the $[101]_c$ direction. As olivine exhibits significant plastic anisotropy (Bai et al., 1991), the parameters that we have calibrated for polycrystalline aggregates do not apply to single crystals. Instead, we estimate these parameters using the observed data by rearranging Equation (3.D.1) and (3.D.2) at steady state to obtain

$$A'(T) = \frac{\dot{\varepsilon}_0}{\sigma_{\mathrm{T},0}^2 \sinh\left(\frac{\sigma_0 - \sigma_{\mathrm{T},0}}{\sigma_{\mathrm{ref}}(T)}\right)}, \tag{3.F.1}$$

$$\mathcal{R}'_{\mathrm{pipe}}(T) = \frac{\dot{\varepsilon}_0}{\sigma_{\mathrm{T},0}^5}, \tag{3.F.2}$$

where $\dot{\varepsilon}_0$ is the steady-state strain rate prior to stress reduction, σ_0 is the applied stress prior to stress reduction, and $\sigma_{\mathrm{T},0}$ is the steady-state Taylor stress prior to stress reduction. Finally, we require the modulus M, which we estimate using Hansen et al.'s fitted parameters to be 26 MPa, for this crystallographic orientation.

The steady-state strain rate prior to reduction is observed to be $\dot{\varepsilon}_0 = 3.76 \times 10^{-5}$ s^{-1} at an applied stress $\sigma_0 = 162$ MPa. Hansen et al. estimate that the steady-state Taylor stress prior to reduction is $\sigma_{\mathrm{T},0} = 84$. However, we find that $\sigma_{\mathrm{T},0} = 104$ MPa better matches the transient strain-time curves.

Given $A'(T)$, $\mathcal{R}'(T)$, and M, we then numerically integrate Equation (3.D.1) and (3.D.2) to obtain the predicted strain-time curves in Figure 3.4.

3.G Model parameters

Assumed values			
Parameter	Units	Value	Reference
μ	GPa	65	Bai and Kohlstedt (1992)
b	m	5×10^{-10}	Bai and Kohlstedt (1992)
β	-	2	Gribb and Cooper (1998)
σ_{P}	GPa	3.1 ± 0.4	Hansen et al. (2019)
M	GPa	135^{+55}_{-47}	Hansen et al. (2019)
Fitted values			
Parameter	Units	Pipe model (Figure 3.1)	Full model (Figure 3.3)
A'^*	$\mathrm{MPa}^{-2}\mathrm{s}^{-1}$	$10^{6.44\pm1.25}$	$10^{6.94\pm1.25}$
$\mathcal{R}'^*_{\mathrm{pipe}}/A'^*$	MPa^{-3}	$10^{-6.43\pm0.45}$	$10^{-7.89\pm0.19}$
$\mathcal{R}'^*_{\mathrm{gb}}/A'^*$	MPa^{-2}	N/A	$10^{-3.40\pm0.37}$
Q	kJ/mol	453 ± 37	450 ± 35
Inferred values			
Parameter	Units	Pipe model (Figure 3.1)	Full model (Figure 3.3)
$\mathcal{R}'^*_{\mathrm{pipe}}$	$\mathrm{MPa}^{-5}\mathrm{s}^{-1}$	$10^{0.01\pm1.38}$	$10^{-0.95\pm1.21}$
$\mathcal{R}'^*_{\mathrm{gb}}$	$\mathrm{MPa}^{-4}\mathrm{s}^{-1}$	N/A	$10^{3.53\pm1.24}$
A^*	$\mathrm{m}^2\mathrm{s}^{-1}$	$10^{-1.81\pm1.3}$	$10^{-1.32\pm1.3}$
$\mathcal{R}^*_{\mathrm{pipe}}$	$\mathrm{m}^4\mathrm{s}^{-1}$	$10^{-11.1\pm1.45}$	$10^{-12.0\pm1.32}$
$\mathcal{R}^*_{\mathrm{gb}}$	$\mu\mathrm{m}\ \mathrm{m}^2\mathrm{s}^{-1}$	N/A	$10^{2.52\pm1.30}$

Table 3.G.1: Parameters from the calibrated model for olivine. Assumed values are taken from the literature. Fitted values are those directly constrained by the model calibration. Inferred values are calculated from the fitted values using the calibrated $\alpha = 2.29^{+0.14}_{-0.13}$. Where possible, the covariance matrix of the model calibration was used to estimate confidence intervals. In the absence of a covariance matrix, confidence intervals were estimated using interval propagation. Superscript asterisks indicate the pre-exponential constant of a parameter assumed to have an Arrhenius dependence on temperature with Q. Primed variables are pre-exponential factors from the model in which dislocation density has been eliminated.

Statement of Authorship for joint/multi-authored papers for PGR thesis

To appear at the end of each thesis chapter submitted as an article/paper

The statement shall describe the candidate's and co-authors' independent research contributions in the thesis publications. For each publication there should exist a complete statement that is to be filled out and signed by the candidate and supervisor **(only required where there isn't already a statement of contribution within the paper itself).**

Title of Paper	Dislocation theory of steady and transient creep of crystalline solids: predictions for olivine
Publication Status	□ Published □ Accepted for Publication x Submitted for Publication □Unpublished and unsubmitted work written in a manuscript style
Publication Details	Breithaupt, T., Katz, R. F., Hansen, L. N., and Kumamoto, K.M. (2021). Dislocation theory of steady and transient creep of crystalline solids: predictions for olivine Submitted to the journal *Science Advances*.

Student Confirmation

Student Name:	Thomas Breithaupt		
Contribution to the Paper	Developed the theoretical model of dislocation density evolution and wrote the manuscript		
Signature	T.P.Breithaupt	Date	11th November 2021

Supervisor Confirmation

By signing the Statement of Authorship, you are certifying that the candidate made a substantial contribution to the publication, and that the description described above is accurate.

Supervisor name and title: Richard F Katz, Professor of Geodynamics
Supervisor comments Tom is the lead author of this study because he conceived the hypothesis, developed the methodology, obtained the results, and wrote the manuscript.

Signature 	Date	11 Nov 2021

This completed form should be included in the thesis, at the end of the relevant chapter.

Chapter 4

Dislocation recovery kinetics in olivine

4.1 Introduction

The material properties of olivine, the primary mineral that makes up the upper mantle, are fundamental to understanding a wide range of geodynamic processes. The microstructure of olivine plays a key role in determining these properties. Key features of microstructure are dislocations—line defects in the crystal lattice—that can control rheological, diffusional, and seismological properties, as well as influence the broader rock microstructure. The canonical role of dislocations is as carriers of deformation because their motion through the crystal lattice results in plastic strain. Classically, the rate of dislocation deformation is understood through the Orowan equation, which predicts that the strain rate is proportional to the density of dislocations and their average velocity (Orowan, 1934). Consequently, the dislocation density plays a key role in determining the effective viscosity of crystalline materials. In the presence of an oscillating stress, dislocations undergo damped vibration, and thus dissipate strain energy (Granato and Lücke, 1956). As a result, models of dislocation density are necessary to predict the attenuation of seismic waves (e.g., Farla et al., 2012). In addition to these dynamic properties, dislocations affect chem-

ical transport in materials because they possess an open structure compared to the bulk lattice, and thus provide fast pathways for diffusion, termed pipe diffusion (e.g., Spingarn et al., 1979). Finally, dislocations strain the surrounding lattice, and thus store strain energy. This stored energy is sufficient to drive the migration of grain boundaries and thus influence grain-size evolution (e.g., Platt and Behr, 2011; Speciale et al., 2020). Through this influence on grain size, the dislocation density can also exert a control on material properties associated with grain size. Thus, to predict the properties of rocks in the upper mantle, it is necessary to understand and model the processes that affect dislocation density.

Dislocations are introduced to the lattice by deformation, and with progressive strain the dislocation density evolves towards a steady state. Empirically, the steady-state dislocation density follows a piezometric power-law relationship with applied stress (Bai and Kohlstedt, 1992; Hirth and Kohlstedt, 2015, and Chapter 3). However, the steady-state dislocation density reflects a balance between competing processes. Of particular interest are recovery processes, which describe the rate of decrease in density. These processes can be investigated through recovery experiments, in which pre-deformed samples are annealed and the decrease in dislocation density is measured. At high temperatures, recovery in olivine is widely assumed to be rate-limited by the climb of dislocations controlled by lattice diffusion of vacancies (e.g., Karato et al., 1993). However, the quantitative evidence to support this assumption is limited. Moreover, recent analysis of the creep properties and the dislocation density piezometer in olivine suggest that vacancy diffusion may instead be facilitated by pipe diffusion i.e., diffusion along dislocation cores or grain boundary diffusion (Hirth and Kohlstedt, 2015, also see Chapter 3). These different diffusion mechanisms result in different recovery kinetics, which would need to be considered in analyses of previous recovery experiments. More broadly, there are a diverse set of recovery processes that may operate in recovery experiments in olivine, and the extent to which these

processes operate in recovery experiments is unknown.

In this chapter, we first consider the recovery processes that may operate in recovery experiments, and then consider the recovery kinetics arising from each of these processes that would be observed. We then review the data from previous recovery experiments in olivine, which largely focus on the effects of temperature, pressure, and chemical environment on recovery and therefore cannot be used to assess recovery kinetics. Finally, we describe new experiments that track dislocation density as a function of time, and thus can be used to infer recovery kinetics.

4.2 Models of recovery

Recovery processes cause decreases in dislocation density, the total dislocation line length per unit volume. Thus, recovery can either be achieved by the annihilation of dislocations of opposite sign or by a decrease in line length of dislocation loops, both of which require dislocation motion. This motion consists of out-of-plane climb and in-plane glide of dislocation segments, either of which may be rate-limiting. These considerations lead to a diverse set of recovery processes, the rates of which depend differently on the dislocation density, temperature, pressure, and chemical environment. The recovery processes are typically modelled using ordinary differential equations (ODEs). Consequently, there is an implicit assumption that spatial heterogeneity in dislocation density, the varying properties of different dislocation slip systems, and the inherent fluctuations in dislocation motion can be averaged out. In this section, we examine models each of these processes in turn and the corresponding kinetic predictions for recovery experiments.

4.2.1 Static climb-controlled recovery

The canonical process of dislocation recovery involves mutual dislocation annihilation in which the rate of recovery is limited by the climb of dislocation segments (e.g., Karato et al., 1993). First, pairs of dislocation segments of opposite sign glide to form dislocation dipoles, pairs of dislocation segments of opposite sign on different glide planes. These dislocation segments that make up the dipoles then climb towards each other and ultimately annihilate. The formation of dislocation dipoles by glide is assumed to be sufficiently fast such that climb limits the rate of annihilation. As the climbing motion of the dislocation segments is driven by their mutual interactions, and not by a macroscopic applied stress, this process is termed static recovery (e.g. Nix et al., 1985). This recovery process may be modelled within many different frameworks (e.g., Friedel, 1964; Blum, 1971; Nes, 1995) that lead to ODEs with the same functional form. Consideration of the availability of dislocations to annihilate, the mutual interactions driving climb, and the mean separation of dislocation dipoles leads to the classical result that the recovery rate is proportional to the square of dislocation density (e.g., Blum, 1971). Moreover, dislocation climb requires the diffusion of material towards or away from the climbing segment, and thus recovery rate is sensitive to the vacancy diffusivity. These factors imply that the static recovery rate is proportional to

$$\dot{\rho} \propto -D\rho^2, \tag{4.2.1}$$

where ρ is the dislocation density, $\dot{\rho}$ is the rate of dislocation density, and D is the vacancy diffusivity of the slowest diffusing species. Typically, it is assumed that vacancies diffuse towards or away from the dislocation through the lattice. However, the vacancy diffusivity can be enhanced by fast diffusion pathways within the microstructure, such as dislocation cores and grain boundaries (Spingarn et al., 1979; Spingarn and Nix, 1979). The effective diffusivity, which accounts for these fast

diffusion pathways, can be calculated using an average of the diffusivities for each respective pathway, weighted by the volume fraction of that pathway (Hart, 1957). For dislocation cores, the volume fraction is proportional to the dislocation density. For grain boundaries, the volume fraction is inversely proportional to the grain size d. Thus, the static recovery rate accounting for the effective vacancy diffusivity is given by

$$\dot{\rho} = -\mathcal{R}_{\text{lattice}}\rho^2 - \mathcal{R}_{\text{pipe}}\rho^3 - \mathcal{R}_{\text{gb}}\rho^2 d^{-1}, \tag{4.2.2}$$

where $\mathcal{R}_\times = \mathcal{R}_\times(T)$ are rate coefficients associated with diffusion along the lattice, pipes, and grain boundaries, respectively. Here, $\times$ is a placeholder for the relevant diffusion pathway. These rate coefficients will, in principle, depend on the temperature T, pressure, and chemical environment. The temperature and pressure dependence of these coefficients reflects that of the diffusivity of the slowest-diffusing species along the respective pathway. The chemical environment influences the recovery rate through its effect on the concentration of the defects that control dislocation motion. For simplicity, in this work we explicitly consider the effect of temperature only, which may be modelled with an Arrhenius dependence as

$$\mathcal{R}_\times(T) = \mathcal{R}_\times^* \exp\left(-\frac{Q_\times}{\mathrm{R}T}\right), \tag{4.2.3}$$

where R is the ideal gas constant, $Q_\times$ is the activation energy, and $\mathcal{R}_\times^*$ are the pre-exponential constants associated with each recovery mechanism.

4.2.2 Glide-controlled recovery

As an alternative to climb-controlled recovery, recovery may be controlled by the glide motion of dislocations. In particular, deformation experiments performed on olivine have demonstrated an observable macroscopic stress generated by the dislocation microstructure, termed the back stress (Hansen et al., 2019; Wallis et al., 2020; Hansen

et al., 2021; Wallis et al., 2021). This back stress can drive dislocation motion and therefore recovery in the absence of an applied stress. In Chapter 3, we demonstrated through thermodynamic considerations that the back stress can be calculated from the dislocation density using the Taylor formula. The back stress, σ_{B}, is therefore given by $\alpha\mu b\sqrt{\rho}$, where α is a constant, μ is the shear modulus, and b is the magnitude of the Burgers vector (Taylor, 1934). The back stress causes the sample to deform through the glide of dislocations at a rate that can be calculated using the flow law

$$\dot{\varepsilon} = -A\rho \sinh\left(\frac{Q_g}{RT}\frac{\alpha\mu b\sqrt{\rho}}{\sigma_{\mathrm{P}}}\right), \tag{4.2.4}$$

where $\dot{\varepsilon}$ is the plastic strain rate, $A = A(T)$ is the rate constant associated with glide, Q_g is the activation energy of dislocation glide, and σ_{P} is the Peierls stress (Hansen et al., 2019, 2021). We assume that the rate constant $A(T)$ has the same functional form as the rate coefficients for static recovery expressed in Equation (4.2.3). We highlight that, as illustrated in Equation (4.2.4), the back stress results in a negative strain rate, which may induce recovery either by forcing dislocations of opposite sign to encounter each other or by shrinking dislocation loops. We now consider each of these cases in turn.

4.2.2.1 Glide-controlled annihilation

The net motion of dislocations, as expressed by the negative plastic strain rate, will intermittently bring dislocation segments of opposite sign in different glide planes in close proximity. If the distance between these dislocation segments is sufficiently small, then the strong stress interactions between them can drive short range diffusion, which facilitates climb and annihilation, even at low temperatures (Nes, 1997). This process can be modelled by assuming that if dislocation segments of opposite sign come within a critical distance of each other, they annihilate (Essmann and Mughrabi,

1979). By consideration of the probability that a moving dislocation segment will encounter one of opposite sign during motion, the recovery rate for this mechanism is found to be

$$\dot{\rho} = -\omega\rho|\dot{\varepsilon}|, \tag{4.2.5}$$

where ω is a non-dimensional parameter that scales with the critical distance for annihilation (Essmann and Mughrabi, 1979).

4.2.2.2 Storage-controlled recovery

Alternatively, the reverse plastic strain caused by the back stress can reduce the dislocation density by reducing the total dislocation line length. For dislocation loops, the dislocation density is proportional to the loop perimeter, whereas the strain accommodated by the loop is proportional to its area (e.g., Kocks, 1966). During forward deformation, dislocation loops expand, resulting in positive strain and a concomitant increase in dislocation density, in a process termed dislocation storage (Kocks, 1966, 1976; Mecking and Kocks, 1981; Estrin and Mecking, 1984; Estrin, 1998). In contrast, the reverse plastic strain driven by the back stress will cause dislocation loops to shrink, concomitantly decreasing the dislocation density. Dislocation storage is modelled using the dislocation mean free path, which is usually modelled statistically in terms of the spacing of obstacles to dislocation motion (Kocks, 1976; Mecking and Kocks, 1981; Estrin and Mecking, 1984; Estrin, 1998). In Chapter 3, we considered the role of grain boundaries and dislocation structures in limiting dislocation motion, leading to the following expression for the dislocation density rate due to storage

$$\dot{\rho} = \frac{1}{b}\left(m\sqrt{\rho} + \frac{n}{d}\right)\dot{\varepsilon}, \tag{4.2.6}$$

where m and n are constants and d is the grain size.

4.2.3 Kinetic descriptions of recovery

In this section, we consider the generic kinetic model typically applied to recovery experiments performed on olivine, and the connections that can be made between it and the underlying physics.

4.2.3.1 n^{th}-order kinetics

The classic empirical recovery kinetics are n^{th}-order recovery kinetics, which are given by

$$\dot{\rho} = -k\rho^n, \tag{4.2.7}$$

where $k = k(T)$ is the rate constant and n is the kinetic order. k is assumed to be proportional to an Arrhenius factor with an empirical activation energy, Q. Integration of this equation yields

$$\rho(t) = \begin{cases} \rho_0 \exp\left(-kt\right), & \text{if } n = 1, \\ \dfrac{\rho_0}{\left(1 + (n-1)\, k\rho_0^{n-1} t\right)^{1/(n-1)}}, & \text{if } n \neq 1, \end{cases} \tag{4.2.8}$$

where ρ_0 is the initial dislocation density and t is the time. Often, analysis of experimental data proceeds by assuming the kinetic order n and rearranging Equation (4.2.8) for k, yielding

$$k = \begin{cases} \dfrac{1}{t} \log\left(\dfrac{\rho_0}{\rho(t)}\right) & \text{if } n = 1, \\ \dfrac{1}{(n-1)t}\left(\dfrac{1}{\rho(t)^{n-1}} - \dfrac{1}{\rho_0^{n-1}}\right) & \text{if } n \neq 1, \end{cases} \tag{4.2.9}$$

which may be calculated directly from the experimental results.

4.2.3.2 Contextualisation of empirical kinetics

The parameters k and n may be contextualised in terms of a specific recovery mechanism by comparing Equation 4.2.7 with the ODE's discussed above. For the case of static climb-controlled recovery, this comparison is both simple and exact. Static recovery controlled by either lattice diffusion or by grain-boundary diffusion results in 2^{nd} order kinetics ($n = 2$), in which k is $\mathcal{R}_{\text{lattice}}$ or $\mathcal{R}_{\text{gb}}/d$, respectively. Alternatively, static recovery controlled by pipe diffusion results in kinetics that are 3^{rd} order ($n = 3$), and k is given by $\mathcal{R}_{\text{pipe}}$.

In contrast to the case of static climb-controlled recovery, glide-controlled recovery does not exactly correspond to n^{th} order recovery kinetics. Indeed, there are no exact analytical solutions in terms of elementary functions for the ODE models of glide-controlled recovery given above. However, for sufficiently small dislocation densities, the sinh dependence of the flow law (Equation 4.2.4) can be linearised to yield n^{th} order kinetics by using the approximation $\sinh(x) \approx x$.

As discussed above, there are two mechanisms for glide-controlled recovery: glide controlled annihilation and storage-controlled recovery. For glide-controlled annihilation, using this linearisation, we obtain $n = 2.5$ and

$$k = \omega b \cdot \left(A \frac{Q_g}{RT} \frac{\alpha \mu}{\sigma_{\text{P}}} \right) \tag{4.2.10}$$

The kinetics resulting from linearisation of storage-controlled recovery depend on the limiting obstacle that controls the dislocation mean free path. If grain boundaries are the limiting obstacle, then $n = 1.5$ and

$$k = \frac{n}{d} \cdot \left(A \frac{Q_g}{RT} \frac{\alpha \mu}{\sigma_{\text{P}}} \right), \tag{4.2.11}$$

whereas if other dislocations are the limiting obstacles, then $n = 2$ and

$$k = m \cdot \left(A \frac{Q_g}{RT} \frac{\alpha \mu}{\sigma_{\mathrm{P}}} \right). \tag{4.2.12}$$

For these approximate kinetics to hold, the argument of the sinh in Equation (4.2.4) must be sufficiently small. The argument is proportional to the square root of dislocation density and inversely proportional to the temperature. Thus, the approximation is more accurate for smaller dislocation densities and at higher temperatures. As this approximation relies upon small dislocation densities, the accuracy of the approximation improves as recovery proceeds. Alternative approximate solutions can be found if the argument of the sinh term is large, which lead to logarithmic recovery kinetics. As these alternative solutions are more accurate for high-dislocation densities and at low temperatures, they are unlikely to apply in high-temperature recovery experiments. For completeness, we consider the log-recovery kinetics that may arise from the processes that we have discussed in Appendix 4.A. Finally, we note that Farla et al. (2011) discusses a further type of recovery kinetics, which is in fact equivalent to n^{th} order kinetics. We explore the correspondence between these models in Appendix 4.B.

4.3 Previous recovery experiments

In this section, we review previous recovery experiments performed on olivine (Ricoult, 1979; Toriumi and Karato, 1978; Kohlstedt et al., 1980; Karato and Sato, 1982; Karato and Ogawa, 1982; Karato et al., 1993; Farla et al., 2011; Wang et al., 2016; Wang and Katsura, preprint). In all of these experiments, well-characterised pre-deformed olivine samples were annealed at high temperatures. The samples were then examined to determine the extent of dislocation recovery. The majority of dislocation recovery experiments have been motivated by the hypothesis that dislocation recovery and dislocation creep are both rate-limited by the same process of dislocation climb. If correct, the sensitivity of creep viscosity to temperature, pressure, and chemical environment at upper-mantle conditions can be evaluated using the results of recovery experiments. As a result of this hypothesis, the recovery process operating in these experiments is usually assumed to be static climb-controlled recovery accommodated by lattice diffusion, which has 2^{nd} order kinetics. Indeed, the majority of these studies assume 2^{nd} order kinetics *a priori* and instead focus on determining the sensitivity of recovery to temperature, pressure, and chemical environment. The only systematic investigations into the order of recovery kinetics in olivine have been performed by Toriumi and Karato (1978), Ricoult (1979), Karato and Ogawa (1982) and Farla et al. (2011).

Both Toriumi and Karato (1978) and Karato and Ogawa (1982) performed two anneals of different durations at the same experimental conditions. In principle, by tracking the decrease in dislocation density with time, the order of recovery kinetics can be determined. Toriumi and Karato performed the pair of anneals on a set of three naturally deformed olivines from different localities and found that their experimental data were consistent with 2^{nd} order kinetics. However, in a comment on this work, Ricoult and Gueguen (1980) queried the robustness of this result, as they

suggested that the uncertainties in measurements of dislocation densities were likely much greater than those reported by Toriumi and Karato. If these uncertainties are accounted for, then the experimental data would also be consistent with 1^{st} order kinetics. In response, Karato and Toriumi (1980) noted that whilst the experimental data from each sample may be consistent with 1^{st} order kinetics in isolation, the aggregated dataset was inconsistent with such kinetics. However, aggregation of their dataset relies on the untested assumption that chemical differences associated with the different origins of their samples does not affect recovery. Furthermore, Karato and Toriumi (1980) indicate that their starting samples were specifically chosen to possess unusually high homogeneity in dislocation structure. This choice was made to facilitate sample characterisation, and led to reported measurement errors that were lower than expected by Ricoult and Gueguen (1980). However, as a result of this choice, their recovery kinetics might not be representative of recovery kinetics in samples with more typical microstructures. Karato and Ogawa (1982) subsequently performed a pair of anneals on a single crystal of San Carlos olivine. They concluded that their data were inconsistent with 1^{st} order kinetics, but with only two datapoints, there remain a broad variety of plausible recovery processes.

Ricoult (1979) performed annealing experiments on dunites, in which they observed dislocation recovery over a range of annealing durations (0.1, 1, 10, and 100 hours) across a spectrum of temperatures. However, utilisation of this dataset to determine kinetic order is difficult, as Ricoult focused on determining the minimum dislocation density in each annealed sample. The relationship between the minimum dislocation density and the average dislocation density is unknown. Ricoult attempted to distinguish between 1^{st} and 2^{nd} order kinetics using this dataset. However, due to the large measurement uncertainties, these kinetic models were indistinguishable.

Farla et al. (2011) annealed a sample of sol-gel olivine at 1300°C for four different durations. However, they did not use these data to investigate the recovery kinetics

and instead assume 2nd order kinetics *a priori*. Farla et al. (2011) calculate rate constants from each of these anneals. If 2nd order kinetics operated in their experiments, all of the rate constants would be equal. The scatter in their calculated rate constants is comparable to the estimated uncertainty in the rate constants, so these data are not inconsistent with 2nd order kinetics within the context of this analysis. However, since no systematic analysis of the kinetic order was performed, direct support from previous experiments for the choice of 2nd order kinetics remains limited.

An alternative approach to this problem involves examining the aggregate dataset formed from all recovery experiments. Although similar dislocation densities and annealing durations were used within each study, these factors vary from study to study. Therefore, in principle, the order of recovery kinetics can be determined from the aggregated dataset. The correct kinetic order will collapse the aggregated dataset onto a single trend. Figure 4.1 explores the temperature dependence of empirically derived rate constants obtained from Equation (4.2.9) under the assumption that recovery follows 2nd order kinetics. The envelope of aggregated dataset spans nearly four orders of magnitude and thus these assumed kinetics do not collapse the dataset. This problem also extends to other choices of n (see Figure 4.7, in which $n = 3$). Indeed, although k's derived from any individual study follow a tight trend in Figure 4.1, each study's results are systematically offset from each other, suggestive of interexperiment bias.

There are a number of plausible sources of interexperiment bias in these recovery experiments, such as the different starting materials used in each experiment, the differing proportions of dislocations of different slip systems that are present, and the different chemical environments used, including different oxygen and water fugacities and silica activities. Furthermore, Farla et al. (2011) postulated that the interexperiment bias arises from the different microscopy techniques employed by different studies. Techniques with greater resolution may resolve a greater number of disloca-

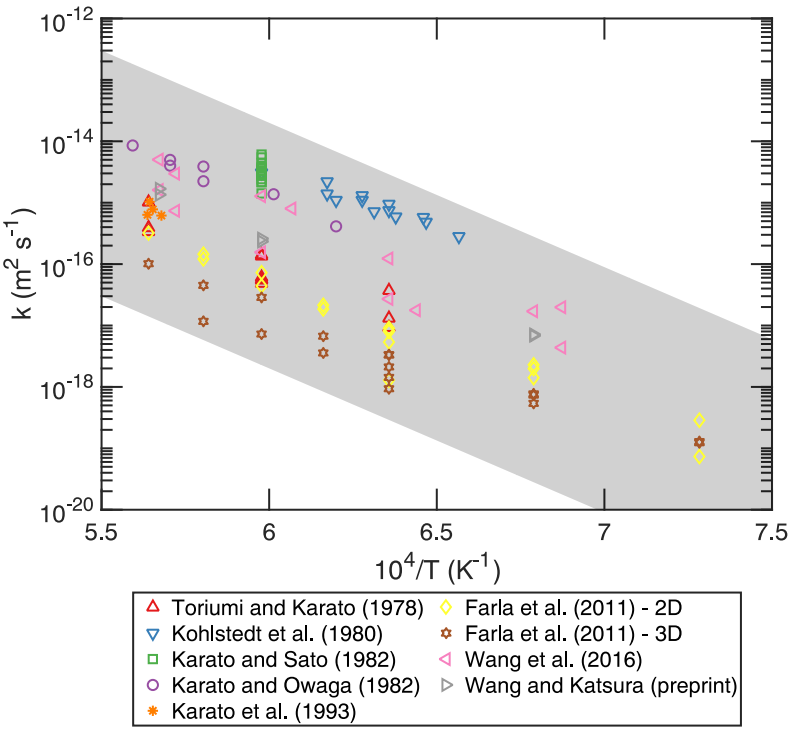

Figure 4.1: Comparison of 2nd order rate constant, k, calculated from previous recovery experiments conducted at atmospheric pressure (Toriumi and Karato, 1978; Kohlstedt et al., 1980; Karato and Sato, 1982; Karato and Ogawa, 1982; Karato et al., 1993; Farla et al., 2011; Wang et al., 2016; Wang and Katsura, preprint). The rate constant is plotted with respect to inverse temperature. Although the aggregate dataset follows a broad trend, there is significant variation in the inferred rate constant from one study to another. To assist the reader, an envelope of the aggregated dataset is plotted as a gray patch, which is constructed by assuming an activation energy of 450 kJ mol^{-1} (Chapter 3). The envelope spans four orders of magnitude at a constant temperature.

tions, and thus a larger dislocation density for the same sample. Thus, newer, higher resolution techniques would observe systematically lower rate constants. Their hypothesis was supported by a correlation within the studies they considered between observed rate constants and the resolution of the microscopy technique used among the studies they considered. However, they did not consider data from Toriumi and Karato (1978), who used an optical microscope—the lowest resolution technique—but observed rate constants comparable in magnitude to those determined by Farla

et al. (2011) using much higher resolution technqiues (see Figure 4.1). Consequently, other sources of interexperiment bias are required to explain this anomaly.

Whilst there are many plausible sources of observed interexperiment bias, it is difficult to quantitatively assess the individual contributions of each source. Indeed, it seems likely that the observed interexperiment bias results from a combination of these sources. Thus, it is inappropriate to try to determine the order of recovery kinetics in olivine using the aggregated dataset of all previous investigations, and the order of recovery kinetics remains unclear. A further complication is that different recovery experiments may involve different recovery mechanisms due to the wide range of experimental conditions explored across these studies, and that the recovery observed in individual experiments may reflect the contribution of multiple recovery mechanisms. Consequently, new data specifically gathered to determine the order of recovery kinetics is necessary.

4.4 Experimental method

To address the problem of determining the order of recovery kinetics, recovery experiments need to be performed that track the decrease in dislocation density over time. To perform these experiments, we used samples deformed as part of previous studies. Samples of pre-deformed San Carlos olivine from two previous studies were used in these experiments; PI-1436 from Schneider (2008) and PI-1543 from Hansen et al. (2011). We give an overview of the experimental histories of these samples here, greater detail can be found in Schneider (2008) and Hansen et al. (2011).

PI-1436 is a single crystal of San Carlos olivine that was deformed in a triaxial compression gas-medium, high-temperature deformation apparatus (Paterson, 1990; Paterson and Olgaard, 2000). This sample was oriented in the $[110]_c$ direction for deformation (Schneider, 2008). The deformation direction controls the slip systems

that are activated and the dislocation structures that develop during deformation (Bai and Kohlstedt, 1992). Consequently, this sample is expected to have an analogous microstructure to the samples used in recovery experiments by Karato and Sato (1982) and Karato et al. (1993), whose samples were pre-deformed in the same orientation. Schneider (2008) deformed this sample in a series of constant load steps at 1200°C to determine a stress exponent. The chemical environment of these experiments was controlled by an orthopyroxene coating, which set the silica activity, and a nickel jacket, which set the oxygen fugacity to be at the nickel-nickel oxide buffer. The final load corresponded to an applied stress of 218 MPa.

In contrast, PI-1543 is a polycrystalline aggregate, which Hansen et al. (2011) fabricated by isostatically hot-pressing powders of San Carlos olivine. This sample was also used in creep tests consisting of constant load steps that were performed in a gas-medium, high-temperature deformation apparatus (Paterson, 1990). The oxygen fugacity of this sample was also set by a nickel jacket. Hansen et al. (2011) determined the grain size of this sample to be 16 µm by applying the mean-intercept method to electron backscatter diffraction (EBSD) maps. This grain size is nearly identical to the grain size of the San Carlos polycrystalline aggregate (13 µm) used in recovery experiments by Farla et al. (2011). In the final step of the creep test, this sample was deformed at 1250°C and 440 MPa, which was held for sufficient strain to achieve mechanical steady state.

For our recovery experiments, the original samples of the single crystal, PI-1436, and polycrystalline aggregate, PI-1543, were sectioned into multiple pieces. One piece of each original sample was retained so that the starting dislocation microstructure could be characterised. Pairs of one piece of the single crystal and one piece of the polycrystalline aggregate were placed in nickel envelopes, which were attached to thermocouples with platinum wires. The samples were then annealed in a horizontal gas-mixing furnace at 1350°C. The oxygen fugacity within the furnace was controlled

using a CO-CO_2 gas mixture with a mixture ratio of 2/55. The mixture ratio was chosen to maintain the oxygen fugacity close to the nickel-nickel oxide buffer. The temperature within the furnace was increased up to 1350°C at a rate of 300°C h^{-1}.

Each pair of samples was annealed for a different duration: 1, 2, 3, 5, or 12 hours. The pair of samples were held in the hot zone of the furnace by the thermocouple wires. At the end of each anneal, the thermocouple wires were retracted, pulling the nickel envelope holding the samples to the cold zone of the furnace. This removal process took 15 minutes. The furnace was then shut down and the process repeated for all of the sample pairs.

To prepare the samples for microstructural characterisation, the samples were first polished with diamond lapping film to 0.5 µm grit. The dislocations within these samples were then decorated using an oxidation-decoration technique Kohlstedt et al. (1976). In this method, the samples are heated in a box oven in an air atmosphere at 900°C for 30 minutes, oxidising their surfaces as well as fast diffusion pathways such as grain boundaries and dislocations. The samples were then polished with diamond lapping film (0.5 µm grit) to remove the surface oxidation layer. This processes leaves the oxidised internal microstructure intact. Finally, the samples were polished with colloidal silica (0.04 µm grit) for 5 minutes.

The dislocation microstructures were then imaged using a JEOL 6500 scanning electron microscope. The accelerating voltage was held at 30 keV. Backscattered electron images were collected with a Centaurus backscatter detector. The images were collected at a variety of magnifications appropriate to the density of the dislocation microstructure within each sample. Each image is 2048×1536 pixels and covers an area ranging from 60 μm^2 to 3000 μm^2. Several images were obtained for each sample.

To determine the final dislocation density for each sample, dislocations were counted in each backscattered electron image. However, because of the sometimes subjective nature of identifying dislocations, the main author was blinded as to which

experiments each image corresponded to reduce the potential influence of the author's expectations on the results. The author was unblinded after the dislocations in all images were counted. The raw backscattered electron images contained some scanning artefacts and shot noise (see Figure 4.2) that prevented the use of the contrast thresholding methods that were applied by Farla et al. (2011). Instead, the images were first filtered using a nonlocal means filter, using the MATLAB function *imnlmfilt* (Buades et al., 2005). This filter smooths shot noise whilst maintaining the sharp contrast between the decorated dislocations and the background, facilitating the process of identifying the dislocations. Figure 4.2 compares a raw backscattered electron image with the corresponding filtered image. Following filtering, each image was subdivided into 12 sub-images, each of which are 512×512 pixels and range from 5 µm^2 to 250 µm^2 in area. For some images, there was a gradient in image quality across the image, such that the dislocation structure could only be clearly discerned at one end of the image. Only sub-images in which the dislocation structure could be clearly discerned were used. The dislocations within each image were then manually counted. In contrast to Farla et al. (2011), no attempt was made to exclude dislocations from counting that appeared to be organised into structures such as walls. This decision was taken because the decision to assign dislocations to these structures can be subjective in some images. Furthermore, for some images, the majority of dislocations appeared to be organised into these structures. Finally the dislocation density for each sub-image was calculated as

$$\rho = 2\frac{N}{A}, \tag{4.4.1}$$

where N is the number of dislocations counted in each image, and A is the area of the sub-image (pp. 89–90 in Karato, 2008). The dislocation density given by Equation (4.2.9) is areal count density, whereas the true dislocation density is defined as the total line length of dislocations per unit volume. The correction factor of 2 in Equation (4.2.9) is derived from calculating the number of dislocation intersec-

tions with a plane for given true dislocation density, assuming that dislocations are randomly orientated.

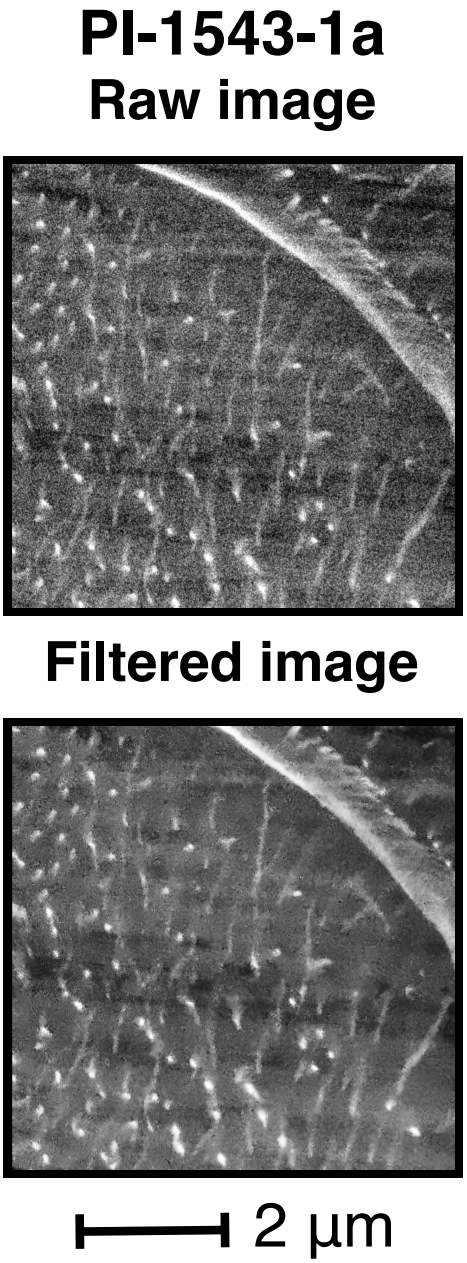

Figure 4.2: Comparison of images of dislocation microstructure (PI-1543-1a) before and after filtering with *imnlmfilt*. The non local means filter reduces the shot noise in the image whilst maintaining the contrast between the decorated dislocations and the background of the image.

4.5 Results

4.5.1 Dislocation microstructure

Typical dislocation microstructures following annealing for PI-1543 are shown in Figure 4.3. In the starting microstructure (Figure 4.3A), dislocations appear to be randomly positioned across the sample surface. After only 1 hour of annealing (Figure 4.3B), dislocations are aligned in approximately linear structures. These linear structures are also present in samples that have undergone a greater duration of annealing. Some of these features exhibit branches, which is particularly evident in the images corresponding to two hours of annealing (see Figure 4.3C). The proportion of dislocations that comprise these linear structures does not follow a simple trend with annealing duration. For example, in the image corresponding to two hours of annealing, nearly all dislocations are part of linear structures, whereas in the image corresponding to five hours of annealing, a significant proportion of dislocations are not. The dislocation density and structure varies between grains. However, each image contains only a few grains, and so the distribution of dislocation densities between grains cannot be investigated further.

4.5.2 Dislocation density

Observations of dislocation density are detailed in Table 4.5.1 and plotted in Figure 4.4. The dislocation density within both PI-1436 and PI-1543 broadly decreases with increasing annealing duration. Compared to the polycrystalline sample, the single crystal sample, PI-1436, starts with a higher initial dislocation density and evolves to a lower dislocation density, suggesting that the recovery rate in PI-1436 is greater. However, there is significant noise around these trends. The range of dislocation density measurements, represented in Figure 4.4 by the extent of the vertical bars,

appears to be higher for PI-1543. However, this difference reflects the greater number of measurements obtained from samples made from this starting material. For the two-hour anneal, the same number of measurements were made for both the single crystal and polycrystalline sample, and the range of measurements is similar.

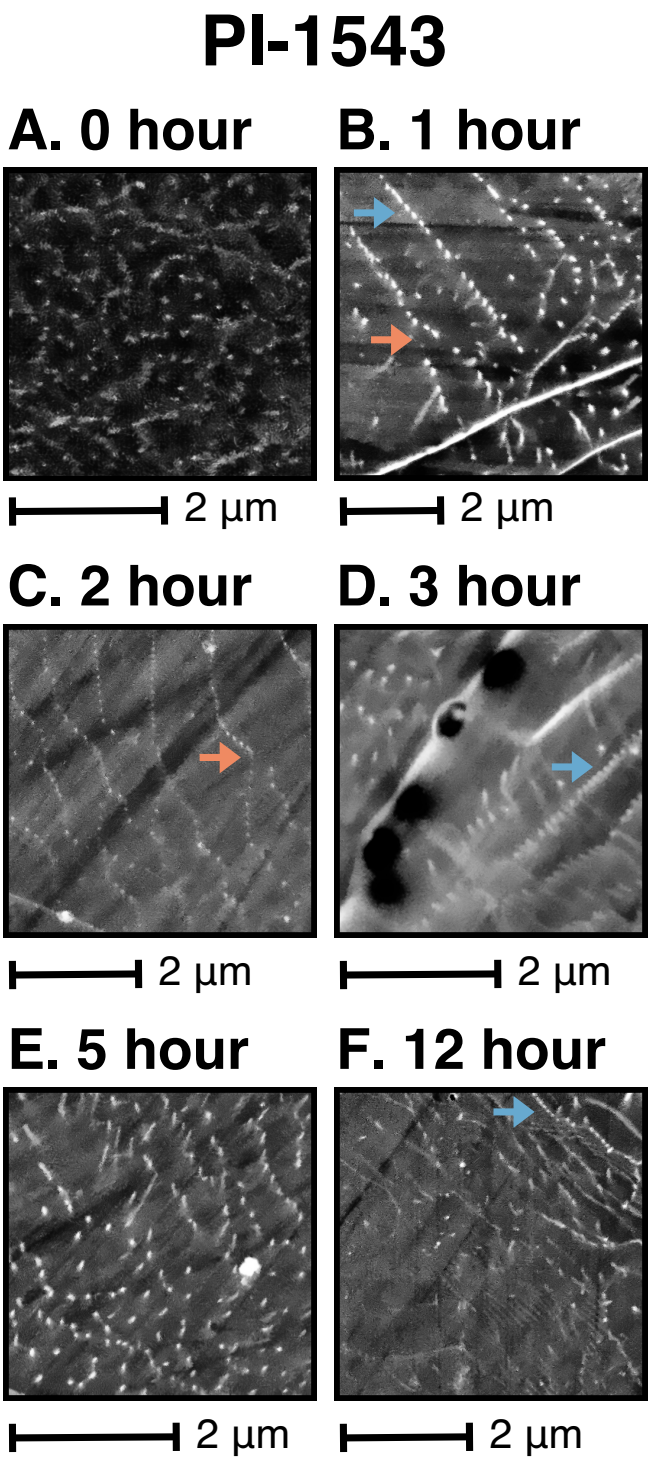

Figure 4.3: Representative images of the dislocation microstructure for PI-1543 after (A) 0, (B) 1, (C) 2, (D) 3, (E) 5, and (F) 12 hours of annealing. The blue arrows highlight some of the straight, linear structures that form following annealing. The red arrows highlight areas in which these linear structures branch in two, and therefore have some curvature.

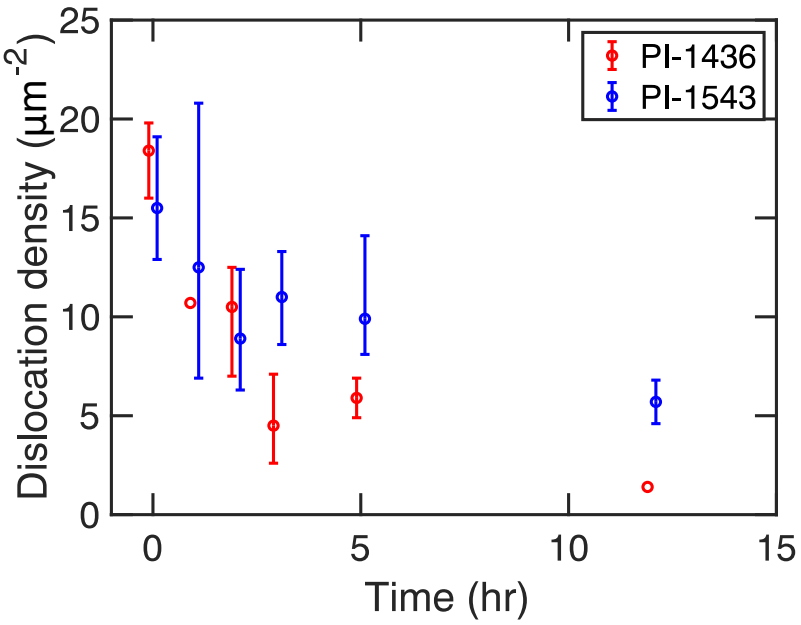

Figure 4.4: Observed dislocation density as a function of time. The range of dislocation density measurements collected from images at each annealing duration is indicated by the vertical bar. The mean value is plotted with an open circle. For annealing durations in which only one datapoint is available, no vertical bar is plotted. Data obtained from PI-1436 is red and data from PI-1536 is blue. Each point and bar is offset by 6 minutes from the actual anneal time so that the data obtained from each starting material can be easily discerned.

Sample	Image	t (hr)	Image average ρ (μm^{-2})	Sample average ρ (μm^{-2})
PI-1436	PI-1436-0a	0	19.5	
	PI-1436-0b	0	16.0	
	PI-1436-0c	0	19.8	18.4
	PI-1436-1a	1	10.7	10.7
	PI-1436-2a	2	7.0	
	PI-1436-2b	2	12.1	
	PI-1436-2c	2	12.5	
	PI-1436-2d	2	10.5	10.5
	PI-1436-3a	3	7.1	
	PI-1436-3b	3	4.5	
	PI-1436-3c	3	2.6	4.7
	PI-1436-5a	5	6.9	
	PI-1436-5b	5	4.9	5.9
	PI-1436-12a	12	1.4	1.4
PI-1543	PI-1543-0a	0	19.12	
	PI-1543-0b	0	12.9	
	PI-1543-0c	0	14.6	15.5
	PI-1543-1a	1	8.1	
	PI-1543-1b	1	6.9	
	PI-1543-1c	1	14.4	
	PI-1543-1d	1	20.8	12.5
	PI-1543-2a	2	9.9	
	PI-1543-2b	2	6.9	
	PI-1543-2c	2	12.4	
	PI-1543-2d	2	6.3	8.9
	PI-1543-3a	3	13.3	
	PI-1543-3b	3	8.6	11.0
	PI-1543-5a	5	8.7	
	PI-1543-5b	5	8.8	
	PI-1543-5c	5	8.1	
	PI-1543-5d	5	14.1	9.9
	PI-1543-12a	12	4.6	
	PI-1543-12b	12	6.8	
	PI-1543-12c	12	6.5	
	PI-1543-12d	12	5.0	5.7

Table 4.5.1: Summary of recovery experiments.

4.6 Discussion

4.6.1 Determination of kinetic order

4.6.1.1 Statistical approach

We now consider the kinetic order that is best supported by our experiments. To discriminate among the different models of recovery, we require a quantitative model selection criterion. We use the Akaike Information Criterion (AIC) (Akaike, 1974) for this purpose. The AIC is derived from an information-theoretic paradigm and is defined as the expected, relative information lost when a model is used to approximate an abstract, conceptual reality (Burnham and Anderson, 2001; Anderson and Burnham, 2004). The 'best' model, which is the most parsimonious model with the greatest strength of evidence, can be selected out of a large set of hypotheses as the model with the smallest AIC (Burnham and Anderson, 2001). As the size of our datasets is small, we use the small-sample second-order AIC, which is defined as

$$\mathrm{AIC} = -2\ln(\mathcal{L}) + 2P + \frac{2P(P+1)}{N-P-1}, \tag{4.6.1}$$

where P is the number of estimated parameters in the model, and N is the number of datapoints (Burnham and Anderson, 2001). $\mathcal{L}$ is the value of the maximised likelihood function, obtained from fitting the model according to the maximum likelihood method, and is defined as the product of the probability of observing each datapoint under the fitted model. To apply the maximum likelihood method to regression, an underlying probability distribution must be assumed for the regression errors. Here, we assume that the regression errors are normally distributed. As a result, the maximum likelihood estimates of the model parameters are equivalent to the least-squares

estimates. Under this assumption, the log-likelihood is given by

$$\ln(\mathcal{L}) = -\frac{N}{2} \ln\left(\frac{\mathrm{SSR}}{N}\right), \tag{4.6.2}$$

up to an additive constant, which does not affect model selection by the AIC and is therefore neglected here. Here, SSR is the sum of squared residuals. Later, we consider the appropriate assumed probability distribution in more detail.

Under the AIC paradigm, all models are compared to the best model, i.e., the model with the smallest AIC. A useful statistic is the relative AIC, Δ, defined as the difference between the model AIC and the minimum AIC value across all models considered. This statistic summarises the strength of model evidence in favour of that model. $\Delta < 2$ indicates that the model has substantial support, $4 < \Delta < 7$ indicates that the model has considerably less support, and $\Delta > 10$ indicates that the model is unsupported (Burnham and Anderson, 2001). Alternatively, the value of Δ may be used to calculate Akaike weights, $w = \exp(-\Delta/2)$. The normalised values of Akaike weights may be loosely interpreted as the probability that the model is the best out of the set of considered models (Burnham and Anderson, 2001).

4.6.1.2 Comparison of kinetic models to data

We now apply the AIC approach to the problem of recovery kinetics. We apply a variety of models with different kinetic orders (i.e., n) to the datasets gathered from annealing of PI-1436 and PI-1543, as well as to the time series reported by Farla et al. (2011) for sol-gel olivine. We consider the values of n suggested by the review of recovery processes presented above $(1.5, 2, 2.5, 3)$. For completeness, we also consider 1^{st} order kinetics, which are not supported by any of the physical processes that we have considered but have been considered empirically by previous studies (Toriumi and Karato, 1978; Karato and Ogawa, 1982). We do not consider a model

with $n = 1.5$ for PI-1436, as that value corresponds to a grain-boundary mechanism that does not apply for a single crystal. For each model, we use Equation (4.2.8) with a specified value of n and fit the rate constant, k, and the initial dislocation density, ρ_0. We include all data listed in Table 4.5.1 in this procedure.

The results of the model fits are plotted in Figure 4.5. The differences between the time series predicted by each model, plotted as the gray envelope, are small, except for PI-1436. For PI-1436, all of the fitted models pass through the same initial dislocation density and diverge significantly beyond 5 hours. This divergence likely results from insufficient data at larger annealing times to discern differences between the possible kinetic models. The results of the statistical analysis are given in Table 4.6.1. For PI-1436, the AIC selected model is $n = 2$, whereas for PI-1543 and the Farla et al. time series, $n = 3$ is the selected model. However, for PI-1436 and PI-1543, the weight of model evidence in favour of these selected models is small (all $\Delta < 2$) and there is substantial support for all of the models we have considered. In contrast, for the Farla et al. (2011) time series, there is considerably less support for kinetics with $n = 1, 1.5,$ and 2, indicating that kinetics with $n = 2.5$ or 3 are much better supported by the experimental data.

Dataset	n	ρ_0 (µm^{-2})	k (m$^{2(n-1)}$s^{-1})	Δ	w
PI-1436	1	18.5	$10^{-3.3}$	0.83	0.24
	1.5	-	-	-	-
	2	18.5	$10^{-17.1}$	0	0.36
	2.5	18.5	$10^{-23.6}$	0.77	0.25
	3	18.5	$10^{-30.1}$	1.7	0.15
PI-1543	1	15	$10^{-3.9}$	1.23	0.14
	1.5	13.9	$10^{-11.1}$	0.89	0.17
	2	14.3	$10^{-17.6}$	0.55	0.2
	2.5	14.7	$10^{-24.1}$	0.24	0.23
	3	15	$10^{-30.6}$	0	0.26
Farla et al. (2011) time series	1	8.1	$10^{-4.5}$	7.11	0.019
	1.5	7.6	$10^{-11.6}$	5.84	0.035
	2	7.8	$10^{-17.9}$	4.23	0.079
	2.5	8	$10^{-24.3}$	2.29	0.21
	3	8.1	$10^{-30.6}$	0	0.66

Table 4.6.1: Summary of statistical analysis of time series of dislocation density. Each row of the table corresponds to a model fit, where n is the kinetic order, k is the maximum likelihood estimate of the rate constant, Δ is the AIC relative to the best model, and w is the normalised Akaike weights. For each dataset, the model selected by the AIC has Δ equal to zero.

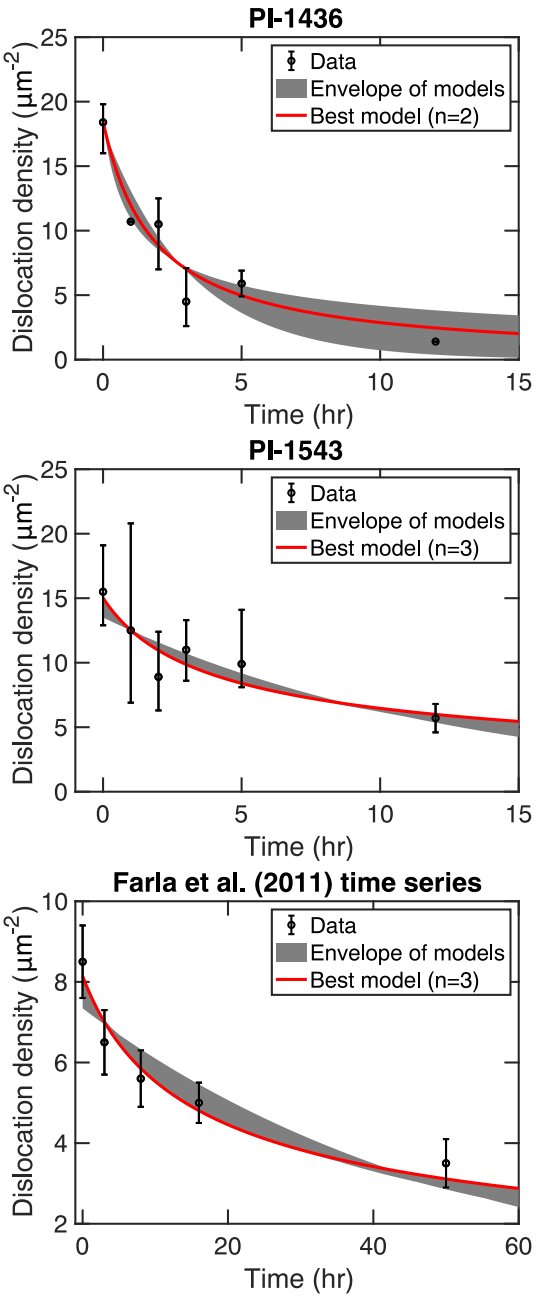

Figure 4.5: Comparison of model fits for PI-1436, PI-1543, and Farla et al. (2011). Points correspond to the mean dislocation density at each annealing duration. For PI-1436 and PI-1543, the vertical bars correspond to the range of observations at that annealing duration. For the Farla et al. (2011) time series, the vertical bars correspond to twice the standard error of the measurement. The envelope of model predictions is plotted as the gray envelope. The AIC best model ($n = 2$ for PI-1436 and $n = 3$ for PI-1543 and the Farla et al. time series) are plotted as red lines.

The fitted rate constants are similar across all three datasets for each choice of n, differing by less than an order of magnitude. This agreement suggests that the same rate constant may be appropriate for all three datasets. Indeed, for 3$^{\text{rd}}$ order kinetics, the rate constants derived from fitting PI-1543 and the time series from Farla et al. (2011) are identical. Moreover, since the three datasets have different initial dislocation densities, combining the datasets may give greater leverage in determining the best kinetic model. To test the hypothesis that the same rate constant applies to all datasets, we apply the same fitting procedure to an aggregated dataset. To avoid biasing the aggregated dataset, we only include the mean values of dislocation density at each annealing duration from PI-1436 and PI-1543, so each dataset contributes a similar amount of data. In addition to fitting a variety of kinetic models, we also consider a base-case model in which each of the datasets is fitted with its own rate constant and the n selected by the previous AIC analysis for that dataset. As a result, the base-case model consists of combining the AIC selected models for each dataset. In this process, we account for the reduced size of the datasets for PI-1436 and PI-1543.

The results of the analysis of the aggregated dataset are given in Table 4.6.2, and time series predictions of the model selected by the AIC ($n = 3$) are compared to each dataset in Figure 4.6. Firstly, we consider the hypothesis that the same rate constant applies to all datasets. The time-series predictions agree with the data gathered at small annealing durations. However, for PI-1436, the model overpredicts the dislocation density at large annealing durations, and for the time series from Farla et al. (2011), the model underpredicts dislocation density at long annealing times. This may be indicative of a small, interexperimental bias between these datasets. However, the base-case model, in which each dataset has a separate rate constant, has a Δ greater than 4, indicating that the best single rate constant model has considerably more support under the AIC paradigm than the base case. Thus, the aggregation

of these datasets is supported by this analysis. Under the aggregated dataset, 1st order kinetics are unsupported by the data. However, aggregation does not improve the discrimination between the cases of $n = 2, 2.5,$ or 3 relative to the analysis of the Farla et al. (2011) time series alone. 3rd order kinetics are best supported, and 2nd order kinetics have considerably less support but cannot be discarded.

n	ρ_0 (µm^{-2})			k (m$^{2(n-1)}$s^{-1})	Δ	w
	PI-1436	PI-1543	Farla et al. (2011)			
1	13.2	14.8	9.6	$10^{-4.5}$	10.86	0.0026
1.5	-	-	-	-	-	-
2	15.8	16.1	9.1	$10^{-17.3}$	4.33	0.068
2.5	16.8	16.3	8.9	$10^{-23.8}$	1.66	0.26
3	17.5	16.3	8.8	$10^{-30.3}$	0	0.60
*					4.23	0.072

Table 4.6.2: Summary of statistical analysis of aggregated dataset. Each row of the table corresponds to a model fit. * refers to the base-case model, in which each constituent dataset is fitted with its own rate constant, as detailed in the text. n is the kinetic order, k is the maximum likelihood estimate of the rate constant, Δ is the AIC relative to the best model, and w is normalised Akaike weight. The model selected by the AIC has Δ equal to zero.

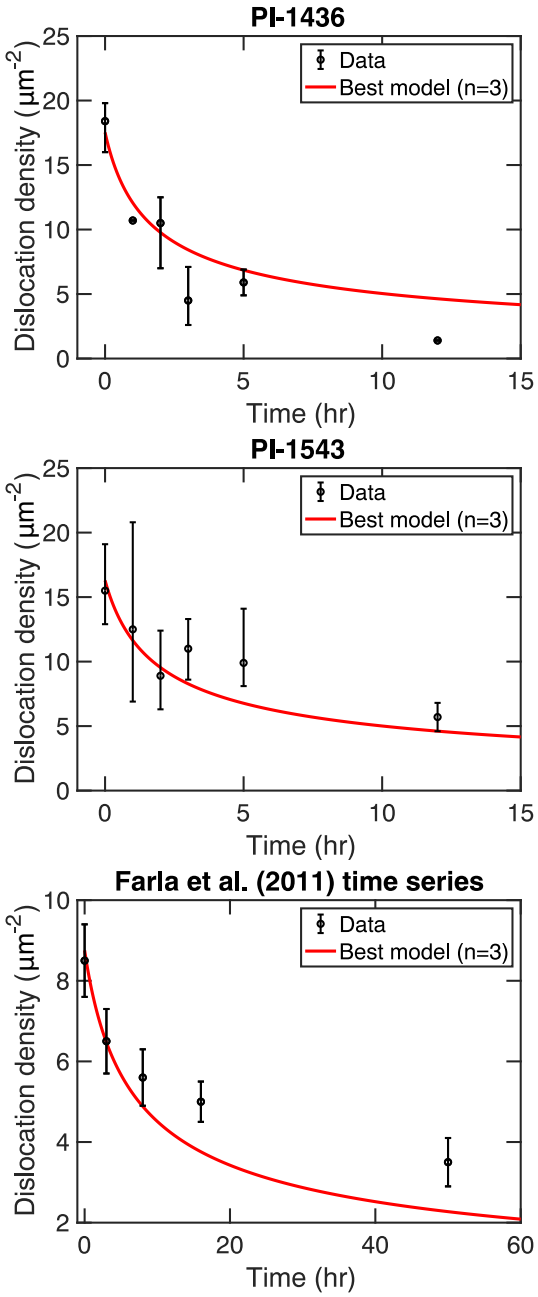

Figure 4.6: Comparison of the predictions of the AIC best model for the aggregated dataset ($n = 3$) against experimental data from PI-1436, PI-1543, and Farla et al. (2011). Points correspond to the mean dislocation density at each annealing duration. For PI-1436 and PI-1543, the vertical bars correspond to the range of observations at that annealing duration. For the Farla et al. (2011) time series, the vertical bars correspond to twice the standard error of the measurement. The envelope of model predictions is plotted as the gray envelope. The best model, as determined by the AIC, is plotted as a red line.

4.6.1.3 Dominant process

Our statistical analysis of the dislocation density time series suggests that $n = 2.5$ or 3 are best supported, which in our framework correspond to glide-controlled annihilation or static recovery controlled by pipe diffusion, respectively. Glide-controlled annihilation is expected to dominate at low temperature, high dislocation density conditions, that are distinct from those investigated here. Indeed, the mathematical formulation of this process considered above, is identical to the dynamic recovery process considered in the context of creep in Chapter 3. This recovery mechanism is required to model creep of olivine at room-temperature conditions, but is negligible at high temperatures. Thus, glide-controlled annihilation is unlikely to be the dominant recovery process in these experiments.

The dominant recovery process can also be explored using the observed microstructures. Linear arrays of dislocations are pervasive throughout the microstructures of the annealed samples (see Figure 4.3), which we interpret as dislocation walls. Dislocation walls were also present in the microstructures reported by Farla et al. (2011). Moreover, these walls possess a branching or polygonal structure (see Figure 4.3B), which we interpret as dislocation cells. The formation of these recovery structures requires the operation of dislocation climb (Raabe, 2014). These observations are consistent with a climb-controlled recovery mechanism. Thus, combined these lines of evidence with the statistical analysis presented above, we suggest that static recovery controlled by pipe diffusion is the dominant recovery mechanism operating in these experiments.

4.6.2 Recontextualisation of previous results

The majority of previous recovery experiments have focused on determining the sensitivity of recovery to temperature, pressure, and chemical environment (Ricoult, 1979;

Toriumi and Karato, 1978; Kohlstedt et al., 1980; Karato and Sato, 1982; Karato and Ogawa, 1982; Karato et al., 1993; Farla et al., 2011; Wang et al., 2016; Wang and Katsura, preprint). The studies quantitatively examine the sensitivity of recovery to these factors, determining variables such as activation energy and activation volume (e.g. Kohlstedt et al., 1980). These quantitative results are then used to critically assess models of creep in olivine and to extrapolate predictions about material properties within the upper mantle. However, the determination of these variables, and the subsequent conclusions drawn, are sensitive to the kinetic order chosen for data analysis. We have demonstrated that data from Farla et al. (2011) better support 3^{rd} order kinetics over the 2^{nd} order kinetics that were assumed in the determination of the temperature-sensitivity of these data. Consequently, reanalysis of this dataset is necessary to determine the activation energy of recovery associated with these kinetics. We emphasise that the appropriate kinetic order for other experimental datasets remains unknown. Indeed, differences in recovery kinetics remain a plausible source of the interexperimental bias in previous recovery experiments (Figure 4.1 and Section 4.3). However, to provide a comparison to the Farla et al. (2011) dataset, we also reanalyse the data with the fastest observed recovery rate in Figure 4.1, taken from the experiments of Kohlstedt et al. (1980) at atmospheric pressure.

Figure 4.7 is an Arrhenius plot of recalculated rate constants against inverse temperature, in which the rate constants are determined assuming 3^{rd} order kinetics. Similar to Figure 4.1, there remains a large interexperiment bias between the datasets of Kohlstedt et al. (1980) and Farla et al. (2011). Moreover, the scatter in each dataset is enhanced by the revaluation with higher order kinetics. This increase in scatter reflects the larger exponent on dislocation density in the calculation of the rate constant (Equation 4.2.9), which compounds the large uncertainties in the determination of dislocation density.

The activation energies determined by fitting the experimental data from Kohlst-

Source	Material	Measurement technique	k^* ($m^4\,s^{-1}$)	Q ($kJ\,mol^{-1}$)
Farla et al. (2011)	Sol-gel olivine	3D SEM	$10^{-22.3\pm1.8}$	245 ± 55
		2D SEM	$10^{-15.8\pm4.3}$	410 ± 130
	San Carlos olivine	3D SEM	$10^{-17.5\pm1.8}$	380 ± 55
		2D SEM	$10^{-15.9\pm1.7}$	405 ± 50
Kohlstedt et al. (1980)	San Carlos olivine	TEM	$10^{-9.5\pm4.6}$	515 ± 140
Chapter 3	-	-	$10^{-12.0\pm1.32}$	450 ± 35

Table 4.6.3: Summary of reanalysis of the temperature sensitivity of recovery in previous datasets. Farla et al. (2011) utilised two techniques to measure dislocation density, a 3D technique that attempted to measure the dislocation density as the line length per unit volume, and a 2D technique similar to the one used in this work. Kohlstedt et al. (1980) used transmission electron microscopy (TEM) to measure dislocation density. The 3rd order recovery kinetics predicted in Chapter 3 from analysis of deformation data is included for comparison. k^* is the pre-exponential constant for the rate constant $k(T)$ and Q is the activation energy. Listed uncertainties correspond to the 95% confidence interval.

edt et al. (1980) and Farla et al. (2011) are listed in Table 4.6.3. The fitted activation energies are broadly similar within uncertainty and approximately equal to $400\,kJ\,mol^{-1}$ across all datasets we consider, with the exception of the dataset from Farla et al. (2011) performed on sol-gel olivine in which dislocation density was measured with a 3D technique. Our fitted activation energies are larger than those determined by previous analyses and the magnitude of this increase depends on the experimental design of the study. From a theoretical perspective, studies that use a fixed annealing time across all annealing temperatures, such as Kohlstedt et al. (1980), will have the largest increases in activation energy under reanalysis. Indeed, the activation energy determined for this dataset is $\approx 200\,kJ\,mol^{-1}$ larger than in the original analysis.

In Figure 4.7, we also explore the effect of the microscopy technique used to measure dislocation density on the apparent activation energy. In their original analysis, Farla et al. (2011) focused on their measurements of dislocation densities obtained from their 3D technique, which measures the total dislocation line length. The ap-

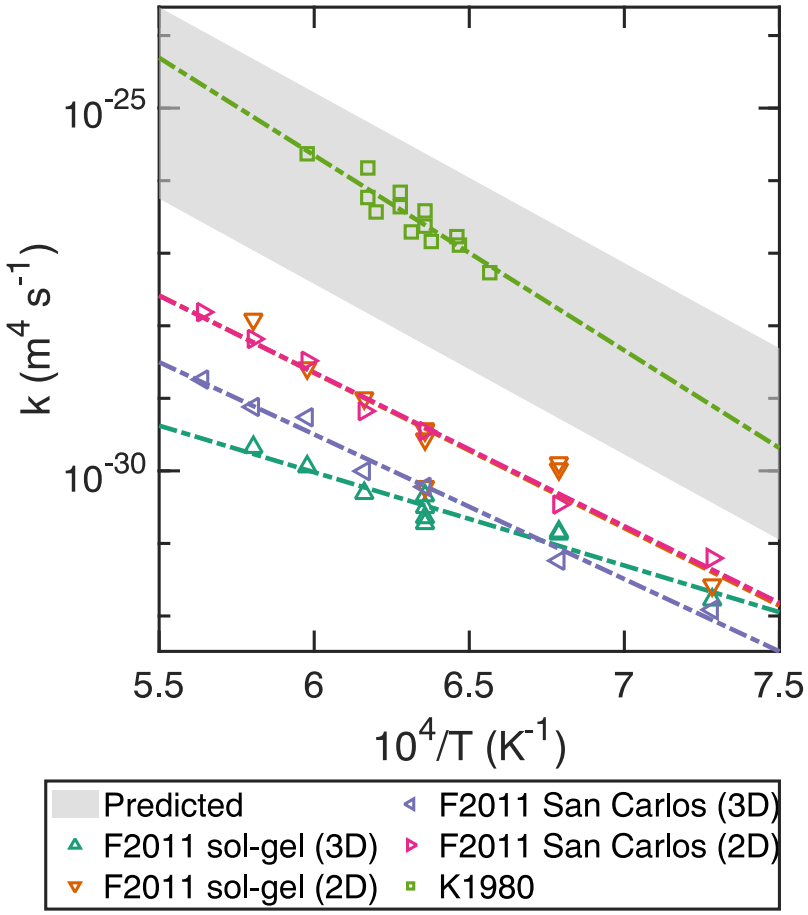

Figure 4.7: Comparison of rate constants, k, recalculated from previous recovery experiments conducted at atmospheric pressure assuming 3rd order kinetics (Kohlstedt et al., 1980; Farla et al., 2011). The rate constant is plotted with respect to inverse temperature. Four datasets are available from Farla et al. (2011) corresponding to two types of starting material (sol-gel vs San Carlos) and two measurement techniques (3D vs 2D). All of these datasets are plotted here. Regression lines (dash-dotted lines) have the same color as the data used in their construction. The gray envelope corresponds to the 3rd order recovery kinetics determined in Chapter 3 from deformation data, accounting for the 95% confidence interval determined in that study. K1980 = Kohlstedt et al. (1980), F2011 = Farla et al. (2011).

parent activation energies for the rate constants derived from annealing of sol-gel and San Carlos olivine samples were markedly different. This difference persists in our analysis. However, Farla et al. (2011) also obtained dislocation density measure-

ments using the same 2D technique as used in the present study. In direct contrast to the 3D-derived rate constants, the 2D-derived rate constants for sol-gel and San Carlos olivine samples overlap within measurement uncertainty with very similar apparent activation energies. Although the source of this discrepancy is unclear, these results highlight an additional effect of systematic measurement biases. In addition to systematically shifting the magnitude of rate constants as discussed by Farla et al. (2011), biases associated with the different techniques used to measure dislocation density can also bias fitted parameters such as activation energy.

The analysis of recovery experiments in olivine suggests that static recovery controlled by pipe diffusion operates as a recovery process in olivine, with an activation energy of approximately $400\,\mathrm{kJ\,mol^{-1}}$. These conclusions support the model proposed in Chapter 3, which was calibrated using data from deformation experiments on olivine. Indeed, we found that the steady-state stress dependence of both strain rate and dislocation density in dislocation creep of olivine could only be explained if dislocation recovery occurred by this process. The predicted rate constants derived from this approach are plotted in Figure 4.7. Its magnitude matches the rate constants derived from the data of Kohlstedt et al. (1980), but is significantly larger than those derived from the data of Farla et al. (2011). This discrepancy may be partially explained by systematic measurement bias, as the model in the previous chapter was calibrated using dislocation density measurements predominantly gathered using lower resolution techniques.

4.7 Conclusions

It has been widely assumed in the literature that dislocation recovery in olivine takes place through the process of static recovery controlled by lattice diffusion. However, quantitative evidence to support this hypothesis has previously been extremely limited. By reviewing the physical principles of dislocation recovery, we have constructed a set of candidate processes that may operate in annealing experiments, as well as corresponding kinetics that may be observed. Statistical analysis of the decrease in dislocation density with time in annealing experiments suggests that a different process dominates in recovery experiments: static recovery controlled by pipe diffusion.

Appendix

4.A Logarithmic recovery kinetics

For large dislocation densities and at low temperatures, the argument of the sinh termin the flow law (Equation 4.2.4) will be large, allowing two approximations to be applied in the derivation of recovery kinetics. Firstly, the variation of dislocation density outside of the sinh may be neglected by replacing factors of ρ with the initial dislocation density ρ_0. Secondly, the sinh itself may be approximated with an exponential, $\sinh(x) \approx (1/2)\exp(x)$. This approach leads to logarithmic recovery kinetics of the form

$$\rho(t)^{1/2} = \rho_0^{1/2} - C\log\left(1 + Dt\right), \tag{4.A.1}$$

where C and D are variables. In particular, D is a variable specific to the recovery mechanism that depends on the initial dislocation density. Although recovery kinetics of this form have not been applied to olivine, they have been successfully applied to recovery in metals (e.g., Nes, 1995). Within our approach, for all of the glide-controlled recovery processes, C is given by

$$C = \frac{\sigma_{\mathrm{P}}}{\alpha\mu b}\frac{RT}{Q_g}. \tag{4.A.2}$$

For glide-controlled annihilation, D is given by

$$D = \frac{1}{4}\alpha b\omega A\rho_0^{3/2}\frac{\mu}{\sigma_{\mathrm{P}}}\frac{Q_g}{RT}\exp\left(\frac{Q_g}{RT}\frac{\alpha\mu b\sqrt{\rho_0}}{\sigma_{\mathrm{P}}}\right). \tag{4.A.3}$$

In the case of storage-controlled recovery limited by grain boundaries,

$$D = \frac{1}{4}\alpha n\frac{1}{d}A\rho_0^{1/2}\frac{\mu}{\sigma_{\mathrm{P}}}\frac{Q_g}{RT}\exp\left(\frac{Q_g}{RT}\frac{\alpha\mu b\sqrt{\rho_0}}{\sigma_{\mathrm{P}}}\right), \tag{4.A.4}$$

and for storage-controlled recovery limited by dislocation obstacles,

$$D = \frac{1}{4}\alpha mA\rho_0\frac{\mu}{\sigma_{\mathrm{P}}}\frac{Q_g}{RT}\exp\left(\frac{Q_g}{RT}\frac{\alpha\mu b\sqrt{\rho_0}}{\sigma_{\mathrm{P}}}\right). \tag{4.A.5}$$

These approximations rely on the argument of the sinh term being large. Moreover, since this approximation requires dislocation densities to be large, as recovery proceeds, the accuracy of this approximation decreases. Indeed, for sufficiently large times, Equation (4.A.1) makes the unphysical prediction that the square root of dislocation density becomes negative. Nes (1995) found that the approximations underpinning log recovery kinetics hold for approximately an order of magnitude reduction in dislocation density.

4.B Correspondence with other kinetic models

In their review of recovery kinetics, Farla et al. (2011) discusses a kinetic model derived by Nes (1995), which takes the form

$$\sqrt{\rho} = \sqrt{\rho_0}\left(1 + \frac{t}{\tau}\right)^{-p}, \tag{4.B.1}$$

where p is an exponent and τ is a recovery timescale. Farla et al. (2011) contrasts kinetics of this form against the empirical n^{th} order recovery kinetics. However,

these kinetic models are simply rearrangements of each other, where the exponent is determined by $p^{-1} = 2(n-1)$ and timescale by $\tau^{-1} = (n-1)k\rho_0^{n-1}$. Finally, we note that although Nes derived these kinetics from a dislocation-network growth model, there is also a correspondence between the exponents derived under Nes's approach and ours. For example, if diffusion occurs through the lattice, then Nes derived $p = 1/2$, which corresponds to the value of $n = 2$ that we have derived. Similarly, if pipe-diffusion controls recovery, then Nes derived $p = 1/4$, which corresponds to $n = 3$.

Chapter 5

Conclusion

5.1 Summary of results

In **Chapter 2**, I extend the canonical model of grain growth, the Hillert model, with a stochastic term to account for heterogeneity in the local environments of grains. By simulating the evolution of a large set of grains, I determine the grain-size distribution and kinetics predicted by the model within the normal grain growth regime. The predicted grain-size distribution is more symmetrical and broader in extent than the Hillert distribution. Moreover, the grain-size distribution matches observations drawn from a large range of experiments and numerical simulations that resolve and evolve the grain structure. The grain-growth kinetics within the normal grain growth regime follow a parabolic relationship, in which the square of the mean grain size is proportional to the mean. Outside of the normal grain growth regime, grain-growth kinetics are much slower.

I investigate the effect of the local environment of grains by examining the grain-size trajectories of individual grains. For grains much smaller in size than the mean, self-curvature dominates the evolution of grain size. In contrast, grains that are much larger in size than the mean undergo a random walk, which reflects that taken by its

local environment radius. An important parameter in defining the local environment is the neighbourhood size, which corresponds to the number of grains within the neighbourhood of an individual grain. As the neighbourhood size becomes large, the grain-size distribution tends towards the Hillert distribution.

There is a close correspondence between the family of grain-size distributions that develop under our model and the Rios distributions, a one-parameter family of grain-size distributions developed from relaxing a constraint applied in the development of the Hillert model. The Rios distributions depend on the Rios parameter, a phenomenological variable whose value is often determined by comparison with experimental grain-size distributions. I compared the grain-size distributions predicted by the model against the family of Rios distributions and observed a relationship between the neighbourhood size and the Rios parameter that generates the best-fitting Rios distribution. This relationship can be successfully applied to predict the grain-growth kinetics in my model.

Finally, I consider the connections between my model and grain topology. Normal grain growth is deeply connected to the topological properties of grains, which can be approximately summarised using the number of faces of a grain. In analytical models of grain growth, this topological information is incorporated indirectly through the size-topology relationship, which predicts the average number of faces possessed by a grain using its grain size relative to the mean. Within my model, each grain possesses a local environment radius, whose value reflects the size of the neighbouring grains. Grains that are surrounded by other grains that are relatively large will possess fewer faces on average, and vice versa. Consequently, the local environment radius allows us to make more inferences about grain topology relative to previous analytical models of grain growth.

In **Chapter 3**, I develop a model for the evolution of dislocation density in terms of two fundamental processes: dislocation storage and dislocation recovery. In devel-

oping this model, I consider the role that fast-diffusion pathways provided by dislocations and grain boundaries have on the rate of recovery. This model is closed with a flow law that expresses the plastic strain rate in terms of the dislocation density and applied stress. Through thermodynamic considerations, I derive the result that the back stress must be equal to the classical Taylor stress. The full model can be solved at a given applied stress, temperature and grain size for dislocation density and strain rate, both prior to and at steady state.

I calibrate the model against data derived from controlled deformation experiments. At steady state, the calibrated model captures the stress, temperature, and grain-size dependence of strain rate observed in experiments. Moreover, the calibrated model predicts the steady-state dependence of dislocation density on applied stress. The model can also be used to predict transient deformation and captures the transient evolution of plastic strain observed in recent stress-reduction experiments.

Beyond replicating the empirical trends between dislocation density, applied stress, grain size and strain rate, the model can also be used to infer the origin of these trends. In particular, the empirical trends in dislocation creep can be explained if recovery is controlled by pipe diffusion, and the trends in grain-size sensitive dislocation creep can be explained if recovery is controlled by grain-boundary diffusion. Importantly, the model predicts that different trends would operate outside of laboratory conditions, suggesting that relationships fitted at laboratory conditions should only be extrapolated with extreme care.

I consider the predictions of the model for steady-state deformation at geological strain rates. At geological conditions, the model predicts that recovery is limited by grain-boundary diffusion, and thus intracrystalline deformation at these conditions is grain-size sensitive. Another key feature of the model is that it predicts a yield stress for deformation, which may be significant relative to ambient mantle stresses for small grain sizes. This yield stress is inversely proportional to the grain size, consistent with

evaluations of the Hall-Petch effect. If grain size within the upper mantle is sufficiently small, then dislocation-accommodated deformation will be inhibited.

I explore the predictions of the model for transient deformation within the upper mantle, by calculating the transient viscosities following a 10% increase in the applied stress. In this analysis, small changes in applied stress result in a disproportionately large (approximately two orders of magnitude) decrease in the viscosity. This effect occurs because deformation is sensitive to the effective stress, which is a small fraction of the applied stress. However, following a change in the applied stress, the effective stress is approximately equal to the change in applied stress, which is comparatively much larger. The modelled transient viscosities evolve on the timescale of years and are comparable in magnitude with those inferred from geophysical observations.

In **Chapter 4**, I examine dislocation recovery experiments performed on olivine. I consider the different recovery processes that could operate in these experiments, and the corresponding kinetics that would be observed. Previous studies have assumed *a priori* that the dominant recovery process in these experiments is static recovery controlled by lattice diffusion. In contrast, I identify an array of potential recovery processes. Previous recovery experiments are insufficient to distinguish between these potential recovery processes due to the large interexperiment biases between them.

I conduct new annealing experiments, which track the decrease in dislocation density with time. I combine this new dataset with a dataset from Farla et al. (2011), which was not previously analysed to determine recovery kinetics. I analyse these datasets using the Akaike Information Criterion (AIC), which can be used to distinguish amongst many model hypotheses. The calculated AIC values suggest that all the datasets considered can be modelled with the same recovery kinetics. The model evidence suggests that dominant recovery process in these experiments is likely to be static recovery controlled by pipe diffusion. This result is consistent with the hypothesis set out in Chapter 3.

In light of this result, I reanalyse the temperature dependence of recovery rate in data from previous experiments. The calculated rate constants have comparable activation energies to that value obtained for this mechanism in Chapter 3. The large interexperiment bias remains in this reanalysis. Rate constants calculated from the model calibrated in Chapter 3 are comparable in magnitude to those calculated using data from Kohlstedt et al. (1980), but orders of magnitude greater than those calculated using data from Farla et al. (2011).

5.2 Future work

There are a number of ways that the approaches to modelling microstructure developed in this thesis can be extended and built upon. Moreover, the model of dislocation-deformation developed in Chapter 3 leads to a number of testable hypotheses. In this section, I propose a number of potential avenues for future study.

5.2.1 Coupling grain size and dislocation-density evolution

Dislocations strain the surrounding lattice and therefore store strain energy. If neighbouring grains have different dislocation densities, and therefore strain energies, the grain boundary separating these grains will migrate to reduce the overall energy of the system, in a mechanism termed strain energy driven grain-boundary migration (ρGBM) (e.g., Platt and Behr, 2011). Through the removal of grains with high dislocation density from the microstructure, ρGBM can drive grain growth.

To model the effect of ρGBM, a model of dislocation density evolution must be coupled to a grain growth model. In the geosciences, this coupling has been attempted by Holtzman et al. (2018) and Mulyukova and Bercovici (2019*b*). However, these studies use phenomenological models of dislocation density evolution, which limits their broader applicability. The dislocation density evolution model developed in

Chapter 3 could be coupled to grain growth using the framework of non-equilibrium thermodynamics. Indeed, this dislocation density evolution model has been developed with thermodynamic consistency in mind (see Section 3.A.3).

We can gain insights into the nature of this prospective coupled model by considering the basic principles that would operate in the model. Since the strain-energy due to dislocations is approximately linear in dislocation density, each grain would be driven to shrink at a rate proportional to its dislocation density. For the total volume of grains to be conserved, this tendency would need to be counteracted by a mean-field dislocation density. Grains with an excess dislocation density relative to the mean-field value would shrink, and vice versa. However, the mean-field dislocation density would not simply be the average dislocation density. Applying the dislocation density equivalent of Equation (2.3) to this model reveals that the mean-field dislocation density is given by $\mathrm{E}[R^2\rho]/\mathrm{E}[R^2]$, where R is the grain size, ρ is the dislocation density and $\mathrm{E}[\cdot]$ is the expectation value. Thus, calculation of the mean-field dislocation density will require knowledge of the joint dislocation-density grain-size distribution. If dislocation density is independent of grain size, then the mean-field dislocation density reduces to the average dislocation density. However, under the qualitative picture of ρGBM presented above, we would expect larger grains to have smaller-than-average dislocation densities because their growth has been facilitated by their smaller dislocation densities. This correlation would cause the mean-field dislocation density to be smaller than the average dislocation density and could potentially facilitate the acceleration of the ρGBM mechanism.

A further potential improvement to this prospective coupled model would be the incorporation of a local environment dislocation density, analogous to the local environment radius developed in Chapter 2. However, the development of a stochastic differential equation for this parameter would be difficult because the mean-field dislocation density is sensitive to the joint distribution of dislocation density and grain

size, and these parameters may evolve on different timescales.

An additional complicating factor would be the effect of ρGBM on the grain topology. As discussed in Chapter 2, parameterisations of normal grain growth that consider grain radii work because of an underlying grain size-topology relationship, which expresses the average number of faces a grain of a given size is expected to possess. ρGBM may disrupt this relationship. Indeed, the operation of ρGBM has been identified in experimental samples by the disruption of the grain-size topology relationship (Boneh et al., 2017). The disrupted size-topology relationship would alter the kinetics of surface-energy grain growth, which would need to be considered in any prospective coupled model. These limitations also apply to models that couple normal grain growth to other processes, such as the palaeowattmeter developed by Austin and Evans (2007).

5.2.2 Stochastic dislocation-density evolution

In this thesis, I have considered the effect of stochastic fluctuations on grain-size evolution. However, sources of random noise are also present in the dislocation microstructure. In this thesis, I have applied the concept of back stress, which is a macroscopic stress that summarises the internal stresses due to dislocations and grain boundaries. However, at the microscopic level, the internal stress is highly spatially heterogeneous (e.g., Wallis et al., 2020, 2021, for observations in olivine), which results in a correspondingly spatially heterogeneous effective stress. Moving dislocations sample this spatially heterogeneous effective stress, which from the perspective of these dislocations is equivalent to fluctuating, noisy effective stress (Hähner, 1996).

In Chapters 3 and 4, we have modelled dislocation density evolution using ordinary differential equations, and thereby assumed that stress fluctuations average out to have no overall effect on dislocation dynamics. However, there are phenomena that have been linked to the effect of a noisy effective stress. For example, in certain

materials such as ice, dislocations are observed to move cooperatively, in intermittent bursts termed dislocation avalanches that have been linked to stochastic dynamics (Weiss, 2019).

Stochastic models of dislocation dynamics have been constructed previously (e.g., Hähner, 1996; Weiss et al., 2015). However, the focus of these studies has been the nature of the appropriate random noise to drive stochastic dislocation dynamics. These models are derived from phenomenological descriptions of dislocation dynamics and do not attempt to also explain the empirical scaling relationships between applied stress, temperature, grain size and strain rate, as we have done in Chapter 3. In contrast, the dislocation density evolution model presented in Chapter 3 could be augmented with stochastic terms to attempt to explain stochastic dislocation phenomena. Future work could consider the potential impact of stochastic dislocation dynamics on these scaling relationships, and on their extrapolation to low-strain rate settings.

5.2.3 Testable hypotheses

In Chapter 3, I have developed a model of dislocation density evolution that explains the empirical scaling relationships between applied stress, temperature, grain size and strain rate in intracrystalline deformation of olivine. The model makes several testable predictions about intracrystalline deformation in the laboratory.

Hypotheses regarding the grain-boundary diffusion regime may be difficult to test due to the contribution of competing deformation mechanisms such as diffusion creep (see Figure 3.5). However, the pipe diffusion regime may be accessed using deformation experiments on single crystals of olivine, in which the grain-boundary diffusion mechanism is suppressed. In this regime, the model predicts that:

1. The steady-state strain rate is proportional to the steady-state back stress raised to the fifth power.

2. The steady-state effective stress is proportional to the steady-state back stress raised to the third power.

3. The steady-state back stress is proportional to the square root of the dislocation density, consistent with the Taylor equation.

These hypotheses could be tested through a series of stress-reduction experiments, which can be used to infer the steady-state back stress at a given applied stress Hansen et al. (2021). The first and second hypotheses can be tested by performing a series of these experiments at an array of applied stresses. To test the third hypothesis, the stress-reduction experiments would need to be complemented with measurements of dislocation density, which could be done using the oxidation-decoration technique applied in Chapter 4.

Bibliography

Akaike, H. (1974), 'A new look at the statistical model identification', *IEEE transactions on automatic control* **19**(6), 716–723.

Anderson, D. and Burnham, K. (2004), 'Model selection and multi-model inference', *Second. NY: Springer-Verlag* **63**(2020), 10.

Atkinson, H. (1988), 'Overview no. 65: Theories of normal grain growth in pure single phase systems', *Acta Metallurgica* **36**(3), 469–491.

Austin, N. J. and Evans, B. (2007), 'Paleowattmeters: A scaling relation for dynamically recrystallized grain size', *Geology* **35**(4), 343–346.

Bai, Q. and Kohlstedt, D. (1992), 'High-temperature creep of olivine single crystals, 2. dislocation structures', *Tectonophysics* **206**(1-2), 1–29.

Bai, Q., Mackwell, S. and Kohlstedt, D. (1991), 'High-temperature creep of olivine single crystals 1. mechanical results for buffered samples', *Journal of Geophysical Research: Solid Earth* **96**(B2), 2441–2463.

Balay, S., Abhyankar, S., Adams, M. F., Brown, J., Brune, P., Buschelman, K., Dalcin, L., Eijkhout, V., Gropp, W. D., Kaushik, D., Knepley, M. G., May, D. A., McInnes, L. C., Mills, R. T., Munson, T., Rupp, K., Sanan, P., Smith, B. F.,

Zampini, S., Zhang, H. and Zhang, H. (2018), PETSc users manual, Technical Report ANL-95/11 - Revision 3.9, Argonne National Laboratory.

Balay, S., Gropp, W. D., McInnes, L. C. and Smith, B. F. (1997), Efficient management of parallelism in object oriented numerical software libraries, *in* E. Arge, A. M. Bruaset and H. P. Langtangen, eds, 'Modern Software Tools in Scientific Computing', Birkhäuser Press, pp. 163–202.

Bercovici, D. (2003), 'The generation of plate tectonics from mantle convection', *Earth and Planetary Science Letters* **205**(3-4), 107–121.

Bierson, C. and Nimmo, F. (2016), 'A test for Io's magma ocean: Modeling tidal dissipation with a partially molten mantle', *Journal of Geophysical Research: Planets* **121**(11), 2211–2224.

Blum, W. (1971), 'Role of dislocation annihilation during steady-state deformation', *Physica Status Solidi (b)* **45**(2), 561–571.

Blum, W. and Eisenlohr, P. (2009), 'Dislocation mechanics of creep', *Materials Science and Engineering: A* **510**, 7–13.

Blum, W., Eisenlohr, P. and Breutinger, F. (2002), 'Understanding creep—a review', *Metallurgical and Materials Transactions A* **33**(2), 291–303.

Boneh, Y., Wallis, D., Hansen, L. N., Krawczynski, M. J. and Skemer, P. (2017), 'Oriented grain growth and modification of 'frozen anisotropy'in the lithospheric mantle', *Earth and Planetary Science Letters* **474**, 368–374.

Breithaupt, T., Hansen, L. N., Toppaladoddi, S. and Katz, R. F. (2021), 'The role of grain-environment heterogeneity in normal grain growth: A stochastic approach', *Acta Materialia* **209**, 116699.

Brown, L. (1989), 'A new examination of classical coarsening theory', *Acta metallurgica* **37**(1), 71–77.

Buades, A., Coll, B. and Morel, J.-M. (2005), A non-local algorithm for image denoising, *in* '2005 IEEE Computer Society Conference on Computer Vision and Pattern Recognition (CVPR'05)', Vol. 2, IEEE, pp. 60–65.

Burnham, K. P. and Anderson, D. R. (2001), 'Kullback-leibler information as a basis for strong inference in ecological studies', *Wildlife research* **28**(2), 111–119.

Cerpa, N. G., Wada, I. and Wilson, C. R. (2017), 'Fluid migration in the mantle wedge: Influence of mineral grain size and mantle compaction', *Journal of Geophysical Research: Solid Earth* **122**(8), 6247–6268.

Coleman, B. D. and Noll, W. (1974), The thermodynamics of elastic materials with heat conduction and viscosity, *in* 'The Foundations of Mechanics and Thermodynamics', Springer, pp. 145–156.

Cooper, R. F., Stone, D. S. and Plookphol, T. (2016), 'Load relaxation of olivine single crystals', *Journal of Geophysical Research: Solid Earth* **121**(10), 7193–7210.

Ding, H., He, Y., Liu, L. and Ding, W. (2006), 'Cellular automata simulation of grain growth in three dimensions based on the lowest-energy principle', *Journal of Crystal Growth* **293**(2), 489–497.

Dixon, N. A. and Durham, W. B. (2018), 'Measurement of activation volume for creep of dry olivine at upper-mantle conditions', *Journal of Geophysical Research: Solid Earth* **123**(10), 8459–8473.

Dunstan, D. and Bushby, A. (2014), 'Grain size dependence of the strength of metals: The hall–petch effect does not scale as the inverse square root of grain size', *International Journal of Plasticity* **53**, 56–65.

Durham, W., Goetze, C. and Blake, B. (1977), 'Plastic flow of oriented single crystals of olivine: 2. observations and interpretations of the dislocation structures', *Journal of Geophysical Research* **82**(36), 5755–5770.

Elsey, M., Esedoglu, S. and Smereka, P. (2010), 'Large-scale simulation of normal grain growth via diffusion-generated motion', *Proceedings of the Royal Society A: Mathematical, Physical and Engineering Sciences* **467**(2126), 381–401.

Essmann, U. and Mughrabi, H. (1979), 'Annihilation of dislocations during tensile and cyclic deformation and limits of dislocation densities', *Philosophical Magazine A* **40**(6), 731–756.

Estrin, Y. (1998), 'Dislocation theory based constitutive modelling: foundations and applications', *Journal of Materials Processing Technology* **80**, 33–39.

Estrin, Y. and Mecking, H. (1984), 'A unified phenomenological description of work hardening and creep based on one-parameter models', *Acta Metallurgica* **32**(1), 57–70.

Farla, R. J., Jackson, I., Gerald, J. D. F., Faul, U. H. and Zimmerman, M. E. (2012), 'Dislocation damping and anisotropic seismic wave attenuation in earth's upper mantle', *Science* **336**(6079), 332–335.

Farla, R., Kokkonen, H., Gerald, J. F., Barnhoorn, A., Faul, U. H. and Jackson, I. (2011), 'Dislocation recovery in fine-grained polycrystalline olivine', *Physics and Chemistry of Minerals* **38**(5), 363–377.

Ferreira, F., Hansen, L. and Marquardt, K. (2021), 'The effect of grain boundaries on plastic deformation of olivine', *Journal of Geophysical Research: Solid Earth* .

Fischer, F., Svoboda, J. and Fratzl, P. (2003), 'A thermodynamic approach to grain growth and coarsening', *Philosophical Magazine* **83**(9), 1075–1093.

Freed, A. M. and Bürgmann, R. (2004), 'Evidence of power-law flow in the mojave desert mantle', *Nature* **430**(6999), 548–551.

Freed, A. M., Bürgmann, R., Calais, E., Freymueller, J. and Hreinsdóttir, S. (2006), 'Implications of deformation following the 2002 Denali, Alaska, earthquake for postseismic relaxation processes and lithospheric rheology', *Journal of Geophysical Research: Solid Earth* **111**(B1).

Freed, A. M., Hirth, G. and Behn, M. D. (2012), 'Using short-term postseismic displacements to infer the ambient deformation conditions of the upper mantle', *Journal of Geophysical Research: Solid Earth* **117**(B1).

Friedel, J. (1964), *Dislocations*, Addison-Wesley series in metallurgy and materials, reprinted with corrections edn, Pergamon ; [Distributed in USA by] Addison-Wesley Pub. Co, Oxford : Reading, Mass.

Fuchizaki, K., Kusaba, T. and Kawasaki, K. (1995), 'Computer modelling of three-dimensional cellular pattern growth', *Philosophical Magazine B* **71**(3), 333–357.

Granato, A. and Lücke, K. (1956), 'Theory of mechanical damping due to dislocations', *Journal of applied physics* **27**(6), 583–593.

Gribb, T. T. and Cooper, R. F. (1998), 'Low-frequency shear attenuation in polycrystalline olivine: Grain boundary diffusion and the physical significance of the andrade model for viscoelastic rheology', *Journal of Geophysical Research: Solid Earth* **103**(B11), 27267–27279.

Groeber, M., Ghosh, S., Uchic, M. D. and Dimiduk, D. M. (2008), 'A framework for automated analysis and simulation of 3d polycrystalline microstructures.: Part 1: Statistical characterization', *Acta Materialia* **56**(6), 1257–1273.

Hähner, P. (1996), 'On the foundations of stochastic dislocation dynamics', *Applied Physics A* **62**(5), 473–481.

Hall, C. E. and Parmentier, E. (2003), 'Influence of grain size evolution on convective instability', *Geochemistry, Geophysics, Geosystems* **4**(3).

Hansen, L. N., Kumamoto, K. M., Thom, C. A., Wallis, D., Durham, W. B., Goldsby, D. L., Breithaupt, T., Meyers, C. D. and Kohlstedt, D. L. (2019), 'Low-temperature plasticity in olivine: Grain size, strain hardening, and the strength of the lithosphere', *Journal of Geophysical Research: Solid Earth* **124**(6), 5427–5449.

Hansen, L. N., Wallis, D., Breithaupt, T., Thom, C. A. and Kempton, I. (2021), 'Dislocation creep of olivine: Backstress evolution controls transient creep at high temperatures', *Journal of Geophysical Research: Solid Earth* **126**(5), e2020JB021325.

Hansen, L., Zimmerman, M. and Kohlstedt, D. (2011), 'Grain boundary sliding in san carlos olivine: Flow law parameters and crystallographic-preferred orientation', *Journal of Geophysical Research: Solid Earth* **116**(B8).

Hansen, L., Zimmerman, M. and Kohlstedt, D. (2012), 'Laboratory measurements of the viscous anisotropy of olivine aggregates', *Nature* **492**(7429), 415–418.

Hart, E. (1957), 'On the role of dislocations in bulk diffusion', *Acta Metallurgica* **5**(10), 597.

Hillert, M. (1965), 'On the theory of normal and abnormal grain growth', *Acta metallurgica* **13**(3), 227–238.

Hirth, G. and Kohlstedt, D. (2003), 'Rheology of the upper mantle and the mantle wedge: A view from the experimentalists', *Geophysical Monograph-American Geophysical Union* **138**, 83–106.

Hirth, G. and Kohlstedt, D. (2015), 'The stress dependence of olivine creep rate: Implications for extrapolation of lab data and interpretation of recrystallized grain size', *Earth and Planetary Science Letters* **418**, 20–26.

Hirth, J. P. and Lothe, J. (1982), *Theory of dislocations*, 2nd ed edn, Wiley, New York ; Chichester.

Holtzman, B., Chrysochoos, A. and Daridon, L. (2018), 'A thermomechanical framework for analysis of microstructural evolution: Application to olivine rocks at high temperature', *Journal of Geophysical Research: Solid Earth* **123**(10), 8474–8507.

Hunderi, O. and Ryum, N. (1980), 'The kinetics of normal grain growth', *Journal of Materials Science* **15**(5), 1104–1108.

Jou, D., Casas-Vázquez, J. and Lebon, G. (1996), 'Extended irreversible thermodynamics', *Extended Irreversible Thermodynamics* pp. 41–74.

Jung, H. and Karato, S. (2001), 'Effects of water on dynamically recrystallized grain-size of olivine', *Journal of Structural Geology* **23**(9), 1337–1344.

Kamachali, R. D. and Steinbach, I. (2012), '3-d phase-field simulation of grain growth: Topological analysis versus mean-field approximations', *Acta Materialia* **60**(6-7), 2719–2728.

Karato, S. (1989), 'Grain growth kinetics in olivine aggregates', *Tectonophysics* **168**(4), 255–273.

Karato, S. (2008), 'Deformation of earth materials', *An Introduction to the Rheology of Solid Earth* **463**.

Karato, S. and Ogawa, M. (1982), 'High-pressure recovery of olivine: implications for creep mechanisms and creep activation volume', *Physics of the Earth and Planetary Interiors* **28**(2), 102–117.

Karato, S., Rubie, D. C. and Yan, H. (1993), 'Dislocation recovery in olivine under deep upper mantle conditions: Implications for creep and diffusion', *Journal of Geophysical Research: Solid Earth* **98**(B6), 9761–9768.

Karato, S. and Sato, H. (1982), 'Effect of oxygen partial pressure on the dislocation recovery in olivine: a new constraint on creep mechanisms', *Physics of the Earth and Planetary Interiors* **28**(4), 312–319.

Karato, S. and Toriumi, M. (1980), 'Experimental studies on the recovery process of deformed olivines and the mechanical state of the upper mantle—reply', *Tectonophysics* **65**(1-2), 186–192.

Karato, S., Toriumi, M. and Fujii, T. (1980), 'Dynamic recrystallization of olivine single crystals during high-temperature creep', *Geophysical Research Letters* **7**(9), 649–652.

Kazaryan, A., Wang, Y., Dregia, S. and Patton, B. (2002), 'Grain growth in anisotropic systems: comparison of effects of energy and mobility', *Acta Materialia* **50**(10), 2491–2502.

Keefner, J., Mackwell, S., Kohlstedt, D. and Heidelbach, F. (2011), 'Dependence of dislocation creep of dunite on oxygen fugacity: Implications for viscosity variations in earth's mantle', *Journal of Geophysical Research: Solid Earth* **116**(B5).

Kertsch, L. and Helm, D. (2016), 'Modelling grain growth in the framework of rational extended thermodynamics', *Modelling and Simulation in Materials Science and Engineering* **24**(4), 045001.

Kim, H.-K., Kim, S. G., Dong, W., Steinbach, I. and Lee, B.-J. (2014), 'Phase-field modeling for 3d grain growth based on a grain boundary energy database', *Modelling and Simulation in Materials Science and Engineering* **22**(3), 034004.

Kim, S. G. and Park, Y. B. (2008), 'Grain boundary segregation, solute drag and abnormal grain growth', *Acta Materialia* **56**(15), 3739–3753.

Kim, Y., Hwang, S., Kim, M., Kwun, S. and Chae, S. W. (2005), 'Three-dimensional Monte-Carlo simulation of grain growth using triangular lattice', *Materials Science and Engineering: A* **408**(1-2), 110–120.

Kocks, U. (1966), 'A statistical theory of flow stress and work-hardening', *Philosophical Magazine* **13**(123), 541–566.

Kocks, U. F. (1976), 'Laws for Work-Hardening and Low-Temperature Creep', *Journal of Engineering Materials and Technology* **98**(1), 76–85.

Kohlstedt, D. and Goetze, C. (1974), 'Low-stress high-temperature creep in olivine single crystals', *Journal of Geophysical Research* **79**(14), 2045–2051.

Kohlstedt, D., Goetze, C., Durham, W. and Vander Sande, J. (1976), 'New technique for decorating dislocations in olivine', *Science* **191**(4231), 1045–1046.

Kohlstedt, D., Nichols, H. and Hornack, P. (1980), 'The effect of pressure on the rate of dislocation recovery in olivine', *Journal of Geophysical Research: Solid Earth* **85**(B6), 3122–3130.

Kohlstedt, D. and Weathers, M. S. (1980), 'Deformation-induced microstructures, paleopiezometers, and differential stresses in deeply eroded fault zones', *Journal of Geophysical Research: Solid Earth* **85**(B11), 6269–6285.

Krausz, A. (1968), 'A rate theory of dislocation mobility', *Acta Metallurgica* **16**(7), 897–902.

Krill, C. and Chen, L.-Q. (2002), 'Computer simulation of 3-d grain growth using a phase-field model', *Acta materialia* **50**(12), 3059–3075.

Langdon, T. (1994), 'A unified approach to grain boundary sliding in creep and superplasticity', *Acta metallurgica et materialia* **42**(7), 2437–2443.

Lebon, G., Jou, D. and Casas-Vázquez, J. (2008), *Understanding non-equilibrium thermodynamics*, Vol. 295, Springer.

Lichtenberg, T., Keller, T., Katz, R. F., Golabek, G. J. and Gerya, T. V. (2019), 'Magma ascent in planetesimals: Control by grain size', *Earth and Planetary Science Letters* **507**, 154–165.

Liu, G., Yu, H. and Qin, X. (2002), 'Three-dimensional grain topology–size relationships in a real metallic polycrystal compared with theoretical models', *Materials Science and Engineering: A* **326**(2), 276–281.

MacPherson, R. D. and Srolovitz, D. J. (2007), 'The von neumann relation generalized to coarsening of three-dimensional microstructures', *Nature* **446**(7139), 1053–1055.

Marthinsen, K., Hunderi, O. and Ryum, N. (1996), 'The influence of spatial grain size correlation and topology on normal grain growth in two dimensions', *Acta materialia* **44**(4), 1681–1689.

Mascagni, M. and Srinivasan, A. (2000), 'Algorithm 806: SPRNG: A scalable library for pseudorandom number generation', *ACM Transactions on Mathematical Software (TOMS)* **26**(3), 436–461.

Mason, J. K., Lazar, E. A., MacPherson, R. D. and Srolovitz, D. J. (2015), 'Geometric and topological properties of the canonical grain-growth microstructure', *Physical Review E* **92**(6), 063308.

McKenzie, D. (1984), 'The generation and compaction of partially molten rock', *Journal of petrology* **25**(3), 713–765.

Mecking, H. and Kocks, U. (1981), 'Kinetics of flow and strain-hardening', *Acta Metallurgica* **29**(11), 1865–1875.

Messerschmidt, U. (2010), *Dislocation dynamics during plastic deformation*, Vol. 129, Springer Science & Business Media.

Minchew, B. M., Meyer, C. R., Robel, A. A., Gudmundsson, G. H. and Simons, M. (2018), 'Processes controlling the downstream evolution of ice rheology in glacier shear margins: case study on rutford ice stream, west antarctica', *Journal of Glaciology* **64**(246), 583–594.

Miyoshi, E., Takaki, T., Ohno, M., Shibuta, Y., Sakane, S., Shimokawabe, T. and Aoki, T. (2017), 'Ultra-large-scale phase-field simulation study of ideal grain growth', *NPJ Computational Materials* **3**(1), 1–6.

Müller, I. (1967), 'On the entropy inequality', *Archive for Rational Mechanics and Analysis* **26**(2), 118–141.

Mullins, W. (1998), 'Grain growth of uniform boundaries with scaling', *Acta materialia* **46**(17), 6219–6226.

Mullins, W. W. (1956), 'Two-dimensional motion of idealized grain boundaries', *Journal of Applied Physics* **27**(8), 900–904.

Mulyukova, E. and Bercovici, D. (2019*a*), 'The generation of plate tectonics from grains to global scales: A brief review', *Tectonics* **38**(12), 4058–4076.

Mulyukova, E. and Bercovici, D. (2019*b*), 'A theoretical model for the evolution of microstructure in lithospheric shear zones', *Geophysical Journal International* **216**(2), 803–819.

Nes, E. (1995), 'Recovery revisited', *Acta metallurgica et materialia* **43**(6), 2189–2207.

Nes, E. (1997), 'Modelling of work hardening and stress saturation in fcc metals', *Progress in materials science* **41**(3), 129–193.

Nes, E., Marthinsen, K. and Brechet, Y. (2002), 'On the mechanisms of dynamic recovery', *Scripta Materialia* **47**(9), 607–611.

Nes, E., Ryum, N. and Hunderi, O. (1985), 'On the zener drag', *Acta Metallurgica* **33**(1), 11–22.

Nimmo, F., Faul, U. and Garnero, E. (2012), 'Dissipation at tidal and seismic frequencies in a melt-free moon', *Journal of Geophysical Research: Planets* **117**(E9).

Nix, W., Gibeling, J. and Hughes, D. (1985), 'Time-dependent deformation of metals', *Metallurgical Transactions A* **16**(12), 2215–2226.

Ohuchi, T., Karato, S. and Fujino, K. (2011), 'Strength of single-crystal orthopyroxene under lithospheric conditions', *Contributions to Mineralogy and Petrology* **161**(6), 961–975.

Oikawa, H., Sugawara, K. and Karashima, S. (1978), 'Creep behavior of al-2.2 at% mg alloy at 573 k', *Transactions of the Japan Institute of Metals* **19**(11), 611–616.

Orowan, E. (1934), 'Zur kristallplastizität. I', *Zeitschrift für Physik* **89**(9-10), 605–613.

Pan, L., Powell, E. M., Latychev, K., Mitrovica, J. X., Creveling, J. R., Gomez, N., Hoggard, M. J. and Clark, P. U. (2021), 'Rapid postglacial rebound amplifies global sea level rise following west antarctic ice sheet collapse', *Science Advances* **7**(18), eabf7787.

Pande, C., Cooper, K. and McFadden, G. (2008), 'Grain size distribution in two dimensions in the long time limit', *Acta materialia* **56**(18), 5304–5311.

Pande, C. and Dantsker, E. (1990), 'On a stochastic theory of grain growth—II', *Acta Metallurgica et Materialia* **38**(6), 945–951.

Pande, C. and Dantsker, E. (1991), 'On a stochastic theory of grain growth—III', *Acta metallurgica et materialia* **39**(6), 1359–1365.

Pande, C. and McFadden, G. (2010), 'Self-similar grain size distribution in three dimensions: A stochastic treatment', *Acta Materialia* **58**(3), 1037–1044.

Pande, C. and Moser, A. (2020), 'Beyond modified mean field: a case for a stochastic grain growth model', *Philosophical Magazine* **100**(7), 837–856.

Pande, C. and Rajagopal, A. (2001), 'Uniqueness and self similarity of size distributions in grain growth and coarsening', *Acta materialia* **49**(10), 1805–1811.

Paterson, M. (1990), 'Rock deformation experimentation', *The brittle-ductile transition in rocks* **56**, 187–194.

Paterson, M. and Olgaard, D. (2000), 'Rock deformation tests to large shear strains in torsion', *Journal of structural Geology* **22**(9), 1341–1358.

Platt, J. and Behr, W. (2011), 'Grainsize evolution in ductile shear zones: Implications for strain localization and the strength of the lithosphere', *Journal of Structural Geology* **33**(4), 537–550.

Poirier, J.-P. (1985), *Creep of crystals: high-temperature deformation processes in metals, ceramics and minerals*, Cambridge University Press.

Pollitz, F. F., Bürgmann, R. and Banerjee, P. (2006), 'Post-seismic relaxation following the great 2004 sumatra-andaman earthquake on a compressible self-gravitating earth', *Geophysical Journal International* **167**(1), 397–420.

Raabe, D. (2014), 'Recovery and recrystallization: phenomena, physics, models, simulation', *Physical Metallurgy* pp. 2291–2397.

Ricoult, D. (1979), 'Experimental annealing of a natural dunite', *Bulletin de Minéralogie* **102**(2), 86–91.

Ricoult, D. and Gueguen (1980), 'Experimental studies on the recovery process of deformed olivines and the mechanical state of the upper mantle—discussion', *Tectonophysics* **65**(1-2), 181–186.

Rios, P. (1999), 'Comparison between a computer simulated and an analytical grain size distribution', *Scripta materialia* **40**(6), 665–668.

Rios, P. (2004), 'Irreversible thermodynamics, parabolic law and self-similar state in grain growth', *Acta materialia* **52**(1), 249–256.

Rios, P., Dalpian, T., Brandao, V., Castro, J. and Oliveira, A. (2006), 'Comparison of analytical grain size distributions with three-dimensional computer simulations and experimental data', *Scripta materialia* **54**(9), 1633–1637.

Rios, P. and Lücke, K. (2001), 'Comparison of statistical analytical theories of grain growth', *Scripta Materialia* **44**(10), 2471 – 2475.

Rios, P. R. and Glicksman, M. E. (2006*a*), 'Self-similar evolution of network structures', *Acta materialia* **54**(4), 1041–1051.

Rios, P. R. and Glicksman, M. E. (2006*b*), 'Topological theory of abnormal grain growth', *Acta materialia* **54**(19), 5313–5321.

Rios, P. and Zöllner, D. (2018), 'Critical assessment 30: Grain growth–unresolved issues', *Materials Science and Technology* **34**(6), 629–638.

Rowenhorst, D., Lewis, A. and Spanos, G. (2010), 'Three-dimensional analysis of grain topology and interface curvature in a β-titanium alloy', *Acta Materialia* **58**(16), 5511–5519.

Rozel, A., Ricard, Y. and Bercovici, D. (2011), 'A thermodynamically self-consistent damage equation for grain size evolution during dynamic recrystallization', *Geophysical Journal International* **184**(2), 719–728.

Rümpker, G. and Wolff, D. (1996), 'Viscoelastic relaxation of a burgers half-space: implications for the interpretation of the fennoscandian uplift', *Geophysical Journal International* **124**(2), 541–555.

Ryum, N. and Hunderi, O. (1989), 'On the analytic description of normal grain growth', *Acta Metallurgica* **37**(5), 1375–1379.

Sandström, R. and Hallgren, J. (2012), 'The role of creep in stress strain curves for copper', *Journal of nuclear materials* **422**(1-3), 51–57.

Schneider, S. (2008), Deformation of Olivine Single Crystals at Intermediate Temperatures: Application to Deformation of the Lithosphere, PhD thesis, University of Minnesota.

Skemer, P., Warren, J. M., Kelemen, P. B. and Hirth, G. (2010), 'Microstructural and rheological evolution of a mantle shear zone', *Journal of Petrology* **51**(1-2), 43–53.

Speciale, P., Behr, W., Hirth, G. and Tokle, L. (2020), 'Rates of olivine grain growth during dynamic recrystallization and postdeformation annealing', *Journal of Geophysical Research: Solid Earth* **125**(11), e2020JB020415.

Spigarelli, S. and Sandström, R. (2018), 'Basic creep modelling of aluminium', *Materials Science and Engineering: A* **711**, 343–349.

Spingarn, J., Barnett, D. and Nix, W. (1979), 'Theoretical descriptions of climb controlled steady state creep at high and intermediate temperatures', *Acta Metallurgica* **27**(9), 1549–1561.

Spingarn, J. and Nix, W. (1979), 'A model for creep based on the climb of dislocations at grain boundaries', *Acta Metallurgica* **27**(2), 171–177.

Srolovitz, D., Anderson, M. P., Sahni, P. S. and Grest, G. S. (1984), 'Computer simulation of grain growth—II. Grain size distribution, topology, and local dynamics', *Acta metallurgica* **32**(5), 793–802.

Streitenberger, P. (1998), 'Generalized Lifshitz-Slyozov theory of grain and particle coarsening for arbitrary cut-off parameter', *Scripta materialia* **39**(12), 1719–1724.

Streitenberger, P. and Zöllner, D. (2006), 'Effective growth law from three-dimensional grain growth simulations and new analytical grain size distribution', *Scripta materialia* **55**(5), 461–464.

Takeuchi, S. and Argon, A. (1976), 'Steady-state creep of single-phase crystalline matter at high temperature', *Journal of materials science* **11**(8), 1542–1566.

Taylor, G. I. (1934), 'The mechanism of plastic deformation of crystals. Part I.—Theoretical', *Proceedings of the Royal Society of London. Series A, Containing Papers of a Mathematical and Physical Character* **145**(855), 362–387.

Thomson, W. (1887), 'LXIII. On the division of space with minimum partitional area', *The London, Edinburgh, and Dublin Philosophical Magazine and Journal of Science* **24**(151), 503–514.

Toriumi, M. and Karato, S. (1978), 'Experimental studies on the recovery process of deformed olivines and the mechanical state of the upper mantle', *Tectonophysics* **49**(1-2), 79–95.

Turcotte, D. L. and Schubert, G. (2002), *Geodynamics*, Cambridge university press.

Turner, A. J., Katz, R. F. and Behn, M. D. (2015), 'Grain-size dynamics beneath mid-ocean ridges: Implications for permeability and melt extraction', *Geochemistry, Geophysics, Geosystems* **16**(3), 925–946.

Uhlenbeck, G. E. and Ornstein, L. S. (1930), 'On the theory of the brownian motion', *Physical review* **36**(5), 823.

Ullah, A., Khan, M., Weihua, X., Hussain, S., ur Rahman, M., Salamat, N., Haq, F. et al. (2017), 'Simulations of grain growth in realistic 3D polycrystalline microstructures and the MacPherson–Srolovitz equation', *Materials Research Express* **4**(6), 066502.

Ullah, A., Liu, G., Luan, J., Li, W., ur Rahman, M. and Ali, M. (2014), 'Three-dimensional visualization and quantitative characterization of grains in polycrystalline iron', *Materials Characterization* **91**, 65–75.

Von Neumann, J. (1952), 'Metal interfaces', *Ohio: American Society for Metals* p. 108.

Wakai, F., Enomoto, N. and Ogawa, H. (2000), 'Three-dimensional microstructural evolution in ideal grain growth—general statistics', *Acta Materialia* **48**(6), 1297–1311.

Wallis, D., Hansen, L. N., Kumamoto, K. M., Thom, C. A., Plümper, O., Ohl, M., Durham, W. B., Goldsby, D. L., Armstrong, D. E., Meyers, C. D. et al. (2020), 'Dislocation interactions during low-temperature plasticity of olivine and their impact on the evolution of lithospheric strength', *Earth and Planetary Science Letters* **543**, 116349.

Wallis, D., Hansen, L. N., Wilkinson, A. J. and Lebensohn, R. A. (2021), 'Dislocation interactions in olivine control postseismic creep of the upper mantle', *Nature Communications* **12**(1), 1–12.

Wang, L., Blaha, S., Pintér, Z., Farla, R., Kawazoe, T., Miyajima, N., Michibayashi, K. and Katsura, T. (2016), 'Temperature dependence of [100](010) and [001](010) dislocation mobility in natural olivine', *Earth and Planetary Science Letters* **441**, 81–90.

Wang, L. and Katsura, T. (preprint), 'Climb of jogs as a rate-limiting process of screw dislocations motion in olivine dislocation creep', *Earth and Space Science Open Archive* .
URL: *https://doi.org/10.1002/essoar.10501470.2*

Wang, M. C. and Uhlenbeck, G. E. (1945), 'On the theory of the brownian motion ii', *Reviews of modern physics* **17**(2-3), 323.

Warren, J. M. and Hirth, G. (2006), 'Grain size sensitive deformation mechanisms in naturally deformed peridotites', *Earth and Planetary Science Letters* **248**(1-2), 438–450.

Weiss, J. (2019), 'Ice: the paradigm of wild plasticity', *Philosophical Transactions of the Royal Society A* **377**(2146), 20180260.

Weiss, J., Rhouma, W. B., Richeton, T., Dechanel, S., Louchet, F. and Truskinovsky, L. (2015), 'From mild to wild fluctuations in crystal plasticity', *Physical review letters* **114**(10), 105504.

Weygand, D., Bréchet, Y., Lépinoux, J. and Gust, W. (1999), 'Three-dimensional grain growth: a vertex dynamics simulation', *Philosophical Magazine B* **79**(5), 703–716.

Whittaker, M., Harrison, W., Lancaster, R. and Williams, S. (2013), 'An analysis of modern creep lifing methodologies in the titanium alloy ti6-4', *Materials Science and Engineering: A* **577**, 114–119.

Wilshire, B. and Scharning, P. (2008), 'Prediction of long term creep data for forged 1cr–1mo–0· 25v steel', *Materials science and technology* **24**(1), 1–9.

Wu, X. and Krausz, A. (1994), 'A kinetics formulation for low-temperature plasticity', *Journal of materials engineering and performance* **3**(1), 169–177.

Yavari, P. and Langdon, T. G. (1982), 'An examination of the breakdown in creep by viscous glide in solid solution alloys at high stress levels', *Acta metallurgica* **30**(12), 2181–2196.

Zhang, C., Enomoto, M., Suzuki, A. and Ishimaru, T. (2004), 'Characterization of three-dimensional grain structure in polycrystalline iron by serial sectioning', *Metallurgical and Materials Transactions A* **35**(7), 1927–1933.

Zhang, J., Zhang, Y., Ludwig, W., Rowenhorst, D., Voorhees, P. W. and Poulsen, H. F. (2018), 'Three-dimensional grain growth in pure iron. Part I. Statistics on the grain level', *Acta Materialia* **156**, 76–85.

Zöllner, D. and Streitenberger, P. (2006), 'Three-dimensional normal grain growth: Monte Carlo Potts model simulation and analytical mean field theory', *Scripta materialia* **54**(9), 1697–1702.